Dissertation

submitted to the

Combined Faculty of Natural Sciences and Mathematics

of Heidelberg University, Germany

for the degree of

Doctor of Natural Sciences

Put forward by

Joseph Weygand

born in Abington, Pennsylvania, USA

Oral Examination: October 14th, 2020

Autocalibration Region Extending Through Time: A Novel GRAPPA Reconstruction Algorithm to Accelerate ^{1}H Magnetic Resonance Spectroscopic Imaging

Referees: Dr. Peter Bachert

Dr Joao Seco

Abstract

ARTT GRAPPA: A Novel GRAPPA Reconstruction Algorithm to Accelerate ^{1}H Magnetic Resonance Spectroscopic Imaging

Magnetic resonance spectroscopic imaging (MRSI) has the ability to noninvasively interrogate metabolism *in vivo*. However, excessively long scan times have thus far prevented its adoption into routine clinical practice. Generalized autocalibrating partially parallel acquisitions (GRAPPA) is a parallel imaging technique that allows one to reduce acquisition duration and use spatial sensitivity correlations to reconstruct the unsampled data points. The coil sensitivity weights are determined implicitly via a fully-sampled autocalibration region in k-space. In this dissertation, a novel GRAPPA-based algorithm is presented for the acceleration of ^{1}H MRSI. Autocalibration Region extending Through Time (ARTT) GRAPPA instead extracts the coil weights from a region in k-t space, allowing for undersampling along each spatial dimension. This technique, by exploiting spatial-spectral correlations present in MRSI data, allows for a more accurate determination of the coil weights and subsequent parallel imaging reconstruction. This improved reconstruction accuracy can then be traded for more aggressive undersampling and a further reduction of acquisition duration. It is shown that the ARTT GRAPPA technique allows for approximately two-fold more aggressive undersampling than the conventional technique while achieving the same reconstruction accuracy. This accelerated protocol is then applied to acquire high-resolution brain metabolite maps in less than twenty minutes in three healthy volunteers at $B_0 = 7$ T.

ARTT GRAPPA: Ein neuer GRAPPA Rekonstruktionsalgorithmus für beschleunigte ^{1}H Magnetresonanzspektroskopische Bildgebung

Die Magnetresonanzspektroskopische Bildgebung (MRSI) ermöglicht die nicht-invasive Untersuchung des Metabolismus *in vivo*. Übermäßig lange Scan-Zeiten haben jedoch bisher die Übernahme in die klinische Routine verhindert. Die verallgemeinerte autokalibrierende partiell parallele Datenaufnahme (GRAPPA) ist eine parallele Bildgebungstechnik, mit der die Aufnahmedauer verkürzt werden kann. Dabei wird eine Phased-Array-Spule genutzt um räumliche Sensitivitätskorrelationen zu extrahieren und nicht abgetastete Datenpunkte zu rekonstruieren. Die Spulensensitivitätsgewichtungen werden implizit über einen vollständig abgetasteten Autokalibrierungsbereich im k-Raum bestimmt. In dieser Dissertation wird ein neuartiger GRAPPA-basierter Algorithmus zur Beschleunigung von ^{1}H-MRSI implementiert. Durch die Erweiterung des GRAPPA-Autokalibrierungsbereichs auf die Zeit (ARTT), werden die Spulengewichtungen aus einem Bereich im k-t-Raum extrahiert, was eine Unterabtastung entlang jeder räumlichen Dimension ermöglicht. Durch Ausnutzung der in den MRSI-Daten vorhandenen räumlich-spektralen Korrelationen, ermöglicht diese Technik eine genauere Bestimmung der Spulengewichtungen und eine anschließende parallele Bildrekonstruktion. Diese verbesserte Rekonstruktionsgenauigkeit kann dann für eine stärkere Unterabtastung und eine weitere Verkürzung der Aufnahmedauer eingetauscht werden. Es wird gezeigt, dass die ARTT GRAPPA-Technik eine circa zweifach stärkere Unterabtastung als die herkömmliche Technik ermöglicht, während die gleiche Rekonstruktionsgenauigkeit erreicht wird. Dieses beschleunigte Protokoll wird dann angewendet, um hochauflösende Hirnmetabolitenkarten mit einer Auflösung von $3,75$ mm in Bildebene in weniger als zwanzig Minuten bei drei gesunden Probanden bei $B_0 = 7$ T aufzunehmen.

Contents

List of Abbreviations

ACS Autocalibration Signal

ARTT Autocalibration Region Extending Through Time

ADP Adenosine Diphosphate

ATP Adenosine Triphosphate

AUTO-SMASH Automatically Calibrated Simultaneous Acquisition of Spatial Harmonics

CAIPIRINHA Controlled Aliasing in Parallel Imaging Results in Higher Acceleration

CHESS Chemical Shift Selective

CNR Contrast-to-Noise Ratio

Cr Creatine

CRLB Cramér–Rao Lower Bound

CT Computed Tomography

DEFT Driven Equilibrium Fourier Transform

EPI Echo Planar Imaging

EPSI Echo Planar Spectroscopic Imaging

FASTMAP Fast Automatic Shimming Technique by Mapping Along Projections

FID Free Induction Decay

FLASH Fast Low-Angle Shot

FOV Field of View

FWHM Full Width at Half Maximum

GABA Gamma Aminobutyric Acid

Glx Glutamine + Glutamate

GPC Glycerophosphorylcholine

GRAPPA Generalized Autocalibrating Partial Parallel Acquisition

IR Inversion Recovery

LASER Localization by Adiabatic Selective Refocusing

MEGA Mescher-Garwood

MM Macromolecules

MOIST Multiply Optimized Insensitive Suppression Train

MR Magnetic Resonance

MRI Magnetic Resonance Imaging

MRSI Magnetic Resonance Spectroscopic Imaging

MSE Mean Squared Error

NAA N-Acetyl Aspartate

NAAG N-Acetylaspartylglutamate

NMR Nuclear Magnetic Resonance

OVS Outer Volume Suppression

PCr Phosphocreatine

PET Positron Emission Tomography

PSF Point Spread Function

PILS Parallel Imaging with Localized Sensitivities

ppm Parts Per Million

PRESS Point Resolved Spectroscopy

RF Radiofrequency

RMS Root Mean Squared

ROI Region of Interest

SAR Specific Absorption Rate

SENSE Sensitivity Encoding

SMASH Simultaneous Acquisition of Spatial Harmonics

SNR Signal-to-Noise Ratio

SPECIAL Spin-Echo Full-Intensity Acquired Localized

STEAM Stimulated Echo Acquisition Mode

SVD Singular Value Decomposition

SWAMP Suppression of Water with Adiabatic Modulated Pulses

tCho Total Choline

tCr Total Creatine

tNAA Total N-Acetyl Aspartate

TE Echo Time

TMS Tetramethylsilane

TSE Turbo Spin Echo

TR Repetition Time

UNFOLD Unaliasing by Fourier-Encoding the Overlaps Using the Temporal Dimension

VAPOR Variable Power Radiofrequency Pulses with Optimized Relaxation Delays

VD-AUTO-SMASH Variable Density Automatically Calibrated Simultaneous Acquisition of Spatial Harmonics

WASHCODE Low-Power Water Suppression by Hyperbolic Secant Pulses with Controlled Offsets and Delays

WATERGATE Water Suppression by Gradient Tailored Excitation

WEFT Water Eliminated Fourier Transform

WET Water Suppression Enhanced through T1 Effects

Chapter 1

Introduction

In 1900, Planck was studying the blackbody radiation emitted by a cavity [1]. Earlier classical analyses carried out by Rayleigh [2] and Jeans [3] exhibited a divergence from experimental observation. In particular, the Rayleigh-Jeans theory predicted that the energy density, defined as the energy contained in a unit volume of the cavity at a given temperature in a specified frequency interval, should tend towards infinity as frequency increases [4]. This calculation utilized the law of equipartition of energy [5] which is derived by integrating the Boltzmann distribution over all possible energies. Planck realized that if energy is instead treated as a discrete variable, then the integral would be replaced by a summation, and his calculated energy density would agree perfectly with experiment [6]. This so called quantum theory would go on to revolutionize physics over the next three decades, and numerous breakthroughs were to follow. In 1905, Einstein [7] proposed the existence of the photon as a quantum of energy to explain the observation of the photoelectric effect [8]. Further evidence for the quantum nature of light was provided by Compton [9] when he described the scattering of a photon by a charged particle. In 1923, de Broglie [10] asserted that particles alternatively possess wave-like properties. Pauli [11] put forth the exclusion principle and Heisenberg [12] articulated the uncertainty principle in 1925 and 1927, respectively. In 1926, Schrödinger [13] developed wave mechanics which caused the world's leading physicists to meet in Brussels the following year to formulate this nascent quantum theory.

At the same time that quantum mechanics was being developed, physicists were also attempting to construct a model that describes the structure of the atom. In 1904, seven years after his discovery of the electron [14], Thomson [15] proposed his so called plum pudding atomic model in which the negatively charged electrons were distributed throughout a sea of homogenous positive charge. This plum pudding model was displaced in 1911, when Rutherford [16] postulated the existence of the atomic nucleus after Geiger and Marsden [17] observed large deflections of α particles when passing through a gold foil. Rutherford's atomic model contained a dense, localized core of positive charge surrounded by orbiting electrons. However, this model was not in agreement with physical observation since an electron orbiting a nucleus would continuously release electromagnetic radiation causing it to lose energy, spiral inward, and, ultimately, collapse in a timescale on the order of picoseconds. To ensure atomic stability, two years later Bohr [18] proposed that electrons are permitted to revolve around the atomic nucleus only in stationary orbits at discrete distances from that nucleus. The major implication of this proposal was that the angular momentum of the revolving electron was quantized

[19]. Sommerfeld [20] expanded on these ideas by further quantizing the shapes and orientations of the allowed electron orbits.

In 1922, Stern and Gerlach [21] devised an experiment that would test the veracity of the Bohr-Sommerfeld model and sent a beam of silver atoms through a nonuniform magnetic field while observing the deflection of each atom as it struck a metallic plate. They found that the deflected atoms split into two discrete groupings which implied the existence of spin angular momentum. Dirac [22] later demonstrated theoretically that spin was a natural consequence of the union of quantum mechanics with special relativity.

The phenomenon of nuclear magnetic resonance (NMR) was first discovered in 1938 by Rabi [23] of Columbia University. Rabi exhibited that the nuclei in a beam of lithium chloride molecules could be induced to flip the orientation of their spins via the application of an oscillating magnetic field in the radiofrequency (RF) regime. Rabi received the 1944 Nobel Prize in physics for this discovery of NMR. Immediately after the war independent teams led by Purcell [24] and Bloch [25] first demonstrated NMR in solid state with experimental setups using paraffin and water, respectively. Purcell and Bloch shared the 1952 Nobel Prize in physics for this work. In 1950, Hahn [26] developed the concept of a spin echo. In 1964, Ernst and Anderson [27] revolutionized the magnetic resonance (MR) field when they developed Fourier transformation NMR spectroscopy. They simultaneously excited all resonances by applying a series of short intense RF pulses and collected time-domain data which was subsequently analyzed using a computer. These early spectroscopic experiments ultimately allowed scientists to interrogate the structure, interaction dynamics, and chemical environment of molecules and belatedly earned Ernst the Nobel Prize in chemistry in 1991.

NMR was first applied to interrogate biological systems in 1955 by Odeblad and Lindström [28]. Their experiments demonstrated that different types of tissues exhibit different relaxation times, a finding that would ultimately be exploited as contrast in producing anatomical images. Further biological studies were to follow [29]. In 1967, Lignon [30] measured the relaxation of water in the arm of a human, and in 1968, Jackson and Langham [31] were the first to perform NMR on an entire living organism. In 1971, Damadian [32] became the first to apply NMR towards diagnostic oncology and showed that malignant tissue exhibits different relaxation times than normal tissue. Although there were grave errors in his experimental setup and the conclusions he ultimately drew [33], Damadian's intense advertisement of NMR's utility in biomedical applications attracted a great amount of publicity and ultimately propelled the NMR field forward.

The major step towards the development of magnetic resonance imaging (MRI) was taken in 1973 by Lauterbur [34] when he introduced the concept of spatial encoding using gradient magnetic fields. By spatially perturbing the strength of the magnetic field, he was able to discern the location at which an NMR signal originates by observing the modulated field's influence on a spin's precessional frequency. Lauterbur's initial developments performed the image reconstruction via a back projection [35], but Ernst and his colleagues incorporated their previous aforementioned work in Fourier transformation

NMR spectroscopy into the MRI reconstruction process and established the Fourier-based reconstruction technique that is used today. Lauterbur initially called this process zeugmatography [36], but it eventually came to be referred to as the more familiar MRI. Lauterbur's contribution to the MRI field did not end with his initial developments, as he and his colleagues went on to pioneer various subfields of MRI such as radiofrequency coil design [37], X-nuclei imaging [38], cardiac imaging [39], magnetization transfer [40], and the use of contrast agents [41]. This work earned Lauterbur one-half of the 2003 Nobel Prize in physiology or medicine. This prize was shared with Mansfield who was the first to acquire an *in vivo* MR image [42] and developed the concept of echo planar imaging [43]. It should be duly noted that at roughly the same time that MRI was being developed, the other vastly influential biomedical imaging modality, computed tomography (CT), was invented by Hounsfield [44] and collaborators.

Magnetic resonance has found applications in a wide variety of biomedical research. One such application is oncology. In addition to producing anatomical images of tumors, the functional aspects of MR can allow one to probe the complex biochemical processes that occur in malignant tissue such as metabolism. Cancerous cells exhibit severely dysregulated metabolic activity. In particular, they typically catabolize glucose via the energy-inefficient pathway of aerobic glycolysis [45], while normal differentiated cells under the same aerobic conditions will metabolize their energy via oxidative phosphorylation in the mitochondria, an observation first made by Warburg [46]. The concentrations of numerous important metabolites are altered in malignant tissue [47], so observing these metabolic changes could be useful in diagnostic oncology. In addition, metabolism is downstream from genetic modifications, so observing tumor metabolism may provide insights into tumor progression or alternatively allow for an earlier prediction of a tumor's response to a given therapy. When an oncologist prescribes a cancer patient with a particular drug, it is not known whether the patient will respond to that drug or not until after the treatment regimen has run its course; therefore, it is important to identify biomarkers which may predict a drug's efficacy at an earlier timepoint in the treatment process so that the course of treatment can be appropriately modified if needed. The various forms of altered metabolic expression serve as potential oncologic biomarkers [48], so a method that interrogates tumor metabolism in a localized and noninvasive manner that can be applied serially is highly desirable.

Magnetic resonance spectroscopic imaging (MRSI) could potentially satisfy this clinical need. MRSI allows for the determination of the relative concentrations of numerous metabolites in a spatially localized fashion and leads to the production of metabolic images. Spectroscopic imaging can be applied serially since magnetic resonance does not utilize ionizing radiation. Although MRSI has been around for decades its adoption into routine clinical practice has been hampered by a number of technical challenges, the most damaging of which is the excessively long scan time required for an examination [49]. This is due to the fact that MRSI requires the acquisition of an extra data dimension, the temporal dimension, in addition to each of the spatial dimensions. Thus, the application of conventional spectroscopic imaging techniques often demands scan times on the order of one hour for spatial resolutions on the order of 5 mm. The maximum achievable spatial resolution is further restricted by the sensitivity of MRSI, which scales with size of the voxels. Although proton spectroscopic imaging is significantly more sensitive than MRSI using more exotic nuclei, this still presents a fundamental

limit on how large of an imaging matrix size can be achieved, especially when interrogating lower concentration metabolites. Sensitivity can be increased by acquiring multiple averages, but this necessarily increases the acquisition time. Thus, there exists a complex interplay between sensitivity and acquisition duration that need be considered when designing an accelerated, high-resolution MRSI experiment.

Recent advances, however, have demonstrated the feasibility of acquiring MRSI datasets and producing two-dimensional metabolite maps of a number of key neurometabolites in a clinically acceptable amount of time [50]. The reduction of acquisition time was accomplished via parallel imaging which decreases the time needed for acquisition by utilizing information regarding the spatial distribution and sensitivities of the individual receiver coil elements in a phased array [51]. In particular, parallel imaging allows one to reduce the total number of required phase encoding steps, and then uses the spatial-sensitivity profile of the phased array to reconstruct the missing data. Other techniques such as echo planar spectroscopic imaging, spiral-based trajectories, and compressed sensing also allow for the acceleration of acquisition duration, and each has found its use in a variety of applications. The only necessity of parallel imaging is that it requires the use of a phased array which are becoming ever more ubiquitous in clinical practice. The reconstruction robustness and general applicability of parallel imaging make it an attractive option, and, therefore, parallel imaging is the strategy which is employed in this work.

Two main flavors of parallel imaging exist: k-space-based reconstructions and image space-based reconstructions. The k-space-based techniques, the most common of which is generalized autocalibrating partial parallel acquisition (GRAPPA), calculate the coil weights in an implicit fashion via the complete acquisition of a central autocalibration region [52], and this procedure requires the full acquisition of one of the spatial dimensions. Therefore, undersampling is only possible along $N-1$ of the dimensions where $N = 2$ or 3 is the number of spatial dimensions acquired. In MRSI a fully-sampled time dimension is directly acquired and can be used in the calculation of the coil weights instead of using one of the spatial directions. Significant spatial-spectral correlations exist in MRSI data, but the incorporation of the spectral component into an MRSI parallel imaging algorithm is often neglected. However, it is possible to exploit these spatial-spectral correlations by using an autocalibration region in k-t space. In this work, a novel time domain-based GRAPPA technique, autocalibration region extending through time (ARTT), is presented and subsequently applied to accelerate the acquisition of spectroscopic imaging data.

Chapter 2

Fundamentals of Nuclear Magnetic Resonance

2.1 Nuclear Spin and the Zeeman Effect

The nucleus of a hydrogen atom consists of a single proton. The proton is a fermion and, therefore, has a spin of one-half. Spin is an intrinsic form of angular momentum and behaves analogously to the quantum mechanical formulation of orbital angular momentum. The spin angular momentum operators along each of the three coordinate axes do not commute with each other and, instead, obey the following relation [53]:

$$[\hat{I}_i, \hat{I}_j] = i\hbar\epsilon_{ijk}\hat{I}_k \tag{2.1}$$

However, one can define the total squared spin angular momentum operator as

$$\hat{I}^2 = \hat{I}_x^2 + \hat{I}_y^2 + \hat{I}_z^2 \tag{2.2}$$

which does commute with the individual component spin angular momentum operators [54]:

$$[\hat{I}^2, \hat{I}_k] = 0 \tag{2.3}$$

for $k \in \{x, y, z\}$. The following eigenvalue equations for the spin operators appearing in Equation 2.3 determine the physical observables of the system:

$$\hat{I}^2|I, m\rangle = \hbar^2 I(I+1)|I, m\rangle \tag{2.4}$$

$$\hat{I}_z|I, m\rangle = \hbar m|I, m\rangle \tag{2.5}$$

A nuclear spin constitutes a magnetic dipole moment given by:

$$\hat{\vec{\mu}} = \gamma\hat{\vec{I}} \tag{2.6}$$

Here, the constant of proportionality γ is the so-called gyromagnetic ratio which is specific to the nucleus in question. For example, the proton [55] possesses a gyromagnetic ratio of

$$\gamma(^1H) = 2.675 \times 10^8 \frac{rad}{Ts} \tag{2.7}$$

Often in the literature, the gyromagnetic ratio of the proton is given in its reduced form as $\frac{\gamma}{2\pi}(^1H) = 42.58 \frac{MHz}{T}$, but the gyromagnetic ratio given by Equation 2.7 is used exclusively in the rest of this work.

If a constant external magnetic field of magnitude B_0 is applied along the z axis, the interaction of the magnetic dipole moment of a nucleus with this external field can be described by the Hamiltonian operator [56]:

$$\hat{H}_z = -\hat{\vec{\mu}} \cdot \vec{B} = -\gamma \hat{\vec{I}} \cdot B_0 \hat{z} \tag{2.8}$$

If this Hamiltonian is inserted into the time-independent Schrödinger equation

$$\hat{H}_z |I, m\rangle = E_m |I, m\rangle \tag{2.9}$$

then it is observed that the Hamiltonian shares the same eigenstates as the spin angular momentum operator along the z axis and obtains the following set of allowed eigenenergies:

$$E_m = -\gamma \hbar m B_0 \tag{2.10}$$

Thus, in the presence of an external magnetic field, a spectral line will split into $2S+1$ discrete energy levels. The separation between each allowed energy level is given by:

$$\Delta E = \gamma \hbar B_0 \tag{2.11}$$

This observation was first made by Zeeman [57] in 1896 and is analogous to Stark's [58] observation that spectral lines split in the presence of an external electric field.

In NMR, transitions between these allowed energy levels are induced by the presence of an oscillating magnetic field, and the energy of the system is altered via the absorption or emission of a photon. When a collection of spins is placed in an external magnetic field, their net magnetic dipole moment vector will precess around the field direction with frequency

$$\omega_0 = \gamma B_0 \tag{2.12}$$

Equation 2.12 is known as the Larmor equation and was articulated prior to the development of quantum mechanics [59].

2.2 Macroscopic Magnetization

Consider a canonical macroscopic ensemble [60] of N nuclei with spin $S = \frac{1}{2}$ in thermal equilibrium with a heat bath at a fixed temperature T. There are $2S + 1 = 2$ possible energy levels, E_+ and E_-, and the probability P that the system is in either state is given by.

$$P_\pm = \frac{1}{Z} e^{-E_\pm / kT} \tag{2.13}$$

Here, Z is the partition function and takes the form

$$Z = e^{-E_+/kT} + e^{-E_-/kT} \tag{2.14}$$

in this two-state system. To calculate the net magnetic moment of the macroscopic ensemble, one must sum over the N individual magnetic moments. Assume that there is a static magnetic field of magnitude B_0 pointing along the z axis. The component of the net magnetic moment in the transverse plane vanishes, and the net magnetic moment vector points along z [61]. The expectation value of an individual magnetic moment is given by:

$$\langle \hat{\mu}_z \rangle = \gamma \langle I_z \rangle = \frac{\gamma\hbar}{2}(P_{\frac{1}{2}} - P_{-\frac{1}{2}}) \tag{2.15}$$

where

$$\frac{N_+ - N_-}{N} = P_{\frac{1}{2}} - P_{-\frac{1}{2}} \tag{2.16}$$

When the degree of polarization is modest, which is the case at the low magnetic field strengths used in clinical magnetic resonance studies, the thermal energies are far greater than the energies associated with spin orientation. In this case, a first-order Taylor expansion can be applied to the exponential term appearing Equation 2.13, and plugging this result into Equation 2.15 and Equation 2.16 yields:

$$\langle \hat{\mu}_z \rangle = \frac{\gamma^2\hbar^2 B_0}{4kT} \tag{2.17}$$

Thus, the macroscopic magnetization in a volume V is

$$M_0 = \sum_{i=1}^{N} \frac{\langle \hat{\mu}_z \rangle}{V} = \frac{N\gamma^2\hbar^2 B_0}{4kTV} \tag{2.18}$$

Note that in Equation 2.18, the magnetization is directly proportional the magnetic field strength but indirectly proportional to the temperature of the system. This observation is a statement of Curie's law [62], named after Pierre Curie.

2.3 Nuclear Magnetic Resonance

The fundamental equation of motion that describes the torque on a magnetic moment in the presence of a magnetic field [63] is

$$\frac{d\vec{\mu}}{dt} = \gamma\vec{\mu} \times \vec{B} \tag{2.19}$$

Taking the derivative with respect to time of both sides of Equation 2.18 and inserting Equation 2.19 yields:

$$\frac{d\vec{M}}{dt} = \vec{M} \times \gamma\vec{B} \tag{2.20}$$

First consider the situation in which the ensemble of spins is only subjected to a static B_0 field pointing in the z direction. In that case, both the magnetization and the magnetic field appearing on the right-hand side of Equation 2.20 point along the z direction. Since the vector product of two parallel vectors vanishes, Equation 2.20 implies that the magnetization is constant in time. Now consider the situation where an RF field that oscillates in the transverse plane at frequency ω_1 is

introduced:

$$\vec{B}_1 = B_1 \cos(\omega_1 t)\hat{x} + B_1 \sin(\omega_1 t)\hat{y} \tag{2.21}$$

At this point, it is customary to transform into a frame of reference known as the rotating reference frame:

$$\begin{pmatrix} x' \\ y' \\ z' \end{pmatrix} = \begin{pmatrix} \cos(\omega_1 t) & 0 & 0 \\ 0 & sin(\omega_1 t) & 0 \\ 0 & 0 & 1 \end{pmatrix} \begin{pmatrix} x \\ y \\ z \end{pmatrix} \tag{2.22}$$

In this frame, Equation 2.20 becomes

$$\frac{d\vec{M}'}{dt} = \vec{M}' \times \gamma \vec{B}_{eff} \tag{2.23}$$

where the effective magnetic field is defined as

$$\vec{B}_{eff} = B_1 \hat{x}' + (B_0 - \frac{\omega_1}{\gamma})\hat{z}' \tag{2.24}$$

The components of Equation 2.23 about each of the three principle axes are known as the Bloch equations [64]. The effective magnetic field is the field that appears in Equation 2.19 when μ is transformed into the rotating reference frame. As can be seen in Equation 2.24, as a result of being in this rotating reference frame, the system experiences a fictitious magnetic field along the z direction opposing the static magnetic field. When the resonance condition is achieved, $\omega_{RF} = \omega_1$, this fictitious field exactly cancels the static field and the z component of Equation 2.24 vanishes. The effective magnetic field then points in the x' direction which induces precession in the y-z plane. Thus, the application of an RF pulse on resonance allows for the flipping of the magnetization vector into the transverse plane. The angle by which the magnetization is rotated away from the z axis, the so-called flip angle α [65], by a constant RF pulse B_1 of duration τ is given by the following equation:

$$\alpha = \omega_1 \tau = \gamma B_1 \tau \tag{2.25}$$

2.4 Relaxation

2.4.1 Spin-Lattice Relaxation

In an *in vivo* NMR experiment, the spins being interrogated do not exist in isolation; instead these spins are inside atoms which compose molecules which, in turn, compose biological systems. These molecules are undergoing constant vigorous motion, so-called molecular tumbling [66]. The magnetic field that a given spin sees is the superposition of the static field with a microscopic field due to the chemical environment in which the spin exists. This microscopic field is constantly changing in both magnitude and direction due to the rapid motion of the molecules. These microscopic fields modulate the precessional motion of a given magnetic moment so that after a long time the magnetic moment of each spin wanders between different precessional cones, until the entire range of possible orientations is sampled. This wandering motion is anisotropic, as it is marginally more favorable for a spin to assume an orientation with a low magnetic field energy; that is, the wandering motion is biased towards orientations in which the magnetic moment is parallel to the field [67].

This biased wandering of spin polarization along the direction of the external field is the basis of spin-lattice relaxation. When a 90° RF pulse is initially applied, the magnetization is flipped entirely into the transverse plane so that the longitudinal magnetization is zero. However, due to spin-lattice relaxation, the longitudinal magnetization slowly starts to recover. The rate of recovery is determined by the spin-relaxation time constant T_1, which is specific for a given material or tissue-type. This T_1 relaxation mechanism can be modeled as an exponential recovery. For example, following a 90° pulse the recovery of the longitudinal magnetization is given by [68]:

$$M_z(t) = M_0(1 - e^{-\frac{t}{T_1}}) \tag{2.26}$$

2.4.2 Spin-Spin Relaxation

The other relaxation mechanism that is important in NMR is spin-spin relaxation. When the magnetization is flipped into the transverse plane, it continues to precess around the longitudinal axis at the Larmor frequency. Again, these individual precessing spins will experience a slightly different magnetic field due to differing chemical environments which modifies a given spin's Larmor frequency. Because the spins are precessing at slightly different frequencies, they eventually dephase, leading to the exponential decay of the transverse magnetization. This decay is categorized by the spin-spin relaxation time constant T_2 which, like T_1, is tissue-dependent. This T_2 relaxation mechanism can be modeled as an exponential decay [68]:

$$M_{xy}(t) = M_0 e^{-\frac{t}{T_2}} \tag{2.27}$$

In actuality, the dephasing of the transverse magnetization occurs much more rapidly than what would be expected with a time constant of T_2 due to inhomogeneities in the magnetic field. This more rapid relaxation process is categorized by the time constant T_2^* which is less than T_2 [69]. In particular, if ΔB characterizes the inhomogeneity of the field across a volume element, T_2^* and T_2 are related via the following equation:

$$\frac{1}{T_2^*} = \frac{1}{T_2} + \gamma \Delta B \tag{2.28}$$

The Bloch equations, given by each component of Equation 2.23, can be extended to include T_1 and T_2 relaxation processes:

$$\frac{dM_x}{dt} = \gamma(\vec{M} \times \vec{B})_x - \frac{M_x}{T_2} \tag{2.29}$$

$$\frac{dM_y}{dt} = \gamma(\vec{M} \times \vec{B})_y - \frac{M_y}{T_2} \tag{2.30}$$

$$\frac{dM_z}{dt} = \gamma(\vec{M} \times \vec{B})_z - \frac{M_0 - M_z}{T_1} \tag{2.31}$$

Further modifications to the Bloch equations have been made by Torrey [70] and McConnell [71] by incorporating diffusion and chemical exchange, respectively.

2.5 Principles of Signal Detection

In order to be detected, the magnetization must be rotated into the transverse plane. After the application of a 90° RF pulse, the magnetization starts to precess in the transverse plane. As the magnetization precesses, the magnetic flux ϕ [72] rotates as well. Because of this changing magnetic flux, an electromotive force will be induced [73] through which the flux sweeps. This observation was first articulated independently by Faraday [74] and Henry [75], and Faraday's law of induction went on to be one of the four fundamental equations in Maxwell's classical formulation of electrodynamics [76]. The electromotive force induced by a changing magnetic flux is given by:

$$emf = -\frac{d\Phi}{dt} \tag{2.32}$$

The Lorentzian principle of reciprocity [77] states that an electromotive force induced in a given circuit X will give rise to the same current in another circuit Y as would be induced in X if the electromotive force operated in Y [78]. Using this principle, Faraday's law can be expressed in an NMR setting as:

$$emf = -\frac{d}{dt}\iiint\limits_{sample} d^3r\vec{M}(\vec{r},t)\cdot\vec{\mathcal{B}}^{receive}(\vec{r}) \tag{2.33}$$

Here, $\vec{\mathcal{B}}^{receive}$ is the field that is produced by the receiver coil at all points with nonvanishing magnetization. Thus, the precessing magnetization induces a current in this coil which constitutes the NMR signal.

2.6 Chemical Shift

In the Larmor equation given by Equation 2.12, the frequency about which a spin precesses is determined by the gyromagnetic ratio and the external magnetic field. The magnetic field a given spin experiences also depends on the chemical environment in which the spin exists [79], a phenomenon known as chemical shift. It is caused by the fact that spins in different chemical environments will experience different magnetic fields due to the shielding of the static field by the electrons surrounding a given spin [80]. In particular, the electrons precess around the static field in the opposite direction as the precessing nuclei. This establishes a microscopic magnetic field that opposes the static field, and this diamagnetic shielding acts to decrease the magnetic field experienced by the nucleus. If σ is a dimensionless shielding constant characterizing a spin's chemical environment, then the field experienced by that spin is given by [81]:

$$\vec{B} = (1-\sigma)\vec{B}_0 \tag{2.34}$$

Thus, the actual resonant frequency is determined by plugging Equation 2.34 into Equation 2.12:

$$\omega = \gamma B = (1-\sigma)\gamma B_0 \tag{2.35}$$

The chemical shift δ is typically defined as [61]:

$$\delta[ppm] = \frac{\omega - \omega_{ref}}{\omega_{ref}}\cdot 10^6 \tag{2.36}$$

where the multiplicative factor of 10^6 ensures that δ is given in units of parts per million (ppm). Here,

ω_{ref} is the Larmor frequency of a reference compound. While the choice of this reference is completely arbitrary, it is conventionally taken to be tetramethylsilane (TMS) [82] in proton spectroscopic studies. While the phenomenon of chemical shift is a nuisance in MRI, as it can cause artifacts in MR images [83], it is the principle that makes spectroscopy possible.

2.7 Spectroscopy

Magnetic resonance spectroscopy (MRS) is a safe, noninvasive technique by which one can probe the biochemical makeup of *in vivo* tissue or an *ex vivo* compound. Spectroscopic studies targeting the proton (^{1}H) [84, 85, 86, 87, 88, 90], carbon-13 (^{13}C) [91, 92, 93, 94, 95, 96, 97], phosphorus-31 (^{31}P) [98, 99, 100, 101], fluorine-19 (^{19}F) [102, 103], sodium-23 (^{23}Na) [104], potassium-39 (^{39}K) [105], and chlorine-35 (^{35}Cl) [106] have been applied to a wide variety of biochemical applications in the literature. Henceforth in this work, unless otherwise specified, it will be assumed that the nucleus being interrogated is ^{1}H.

When the magnetization is flipped into the transverse plane it starts to precess about the longitudinal axis. Simultaneously, this transverse magnetization undergoes T_2^* decay, as discussed in Section 2.4.2. Thus, the magnetization along one of the transverse axes as a function of time undergoes damped oscillations: the product of a purely sinusoidal function with a decaying exponential function characterized by time constant T_2^*. This observable signal is known as a free induction decay (FID) [107]. In general, if the sample being measured contains numerous protons oscillating with different chemical shifts, this NMR signal is a superposition of signals oscillating at different frequencies. Fourier analysis [108] allows one to parse out the individual contributions from each frequency component. This is performed by taking the Fourier transformation of the FID to yield an NMR spectrum. This concept is illustrated in Figure 2.1 which was modified from a figure taken from Zaiss [109]. In Figure 2.1.A, an FID that oscillates at a single frequency is shown decaying in time. Figure 2.1.B depicts the Fourier transformation of this monofrequency FID as a spectrum with a single peak. The number of frequency components contributing to a given FID will correspond to the number of peaks present in its resultant spectrum. As can be seen in the figure, the line width of the peak, quantified by its full width at half maximum (FWHM) is inversely proportional to T_2^*; thus, a more homogeneous magnetic field will produce spectra with sharper resonances.

An exemplary *in vivo* ^{1}H NMR spectrum is displayed in Figure 2.2, an illustration taken from De Graaf [61]. This spectrum was acquired at $B_0 = 11.75$ T in the brain of a living rat. Many commonly observed metabolites are labeled. The horizontal axis is chemical shift, as was discussed in Section 2.6, and the intensity of the peaks corresponds to the relative concentration of that metabolite in the region of interest [110]. The location of a resonance on the chemical shift axis allows one to identify to which metabolite a signal corresponds, although overlapping peaks do occur and render metabolite quantification difficult. In this figure the chemical shift range was censored between four and five ppm in order to omit the unsuppressed water peak occurring at approximately 4.7 ppm [111].

A given metabolite containing M nonequivalent proton groups will show up as M different resonances occurring at unique chemical shifts in a ^{1}H NMR spectrum. Scalar coupling, which is the indirect coupling of two spins via the chemical bonds connecting these spins, causes a given resonance line to

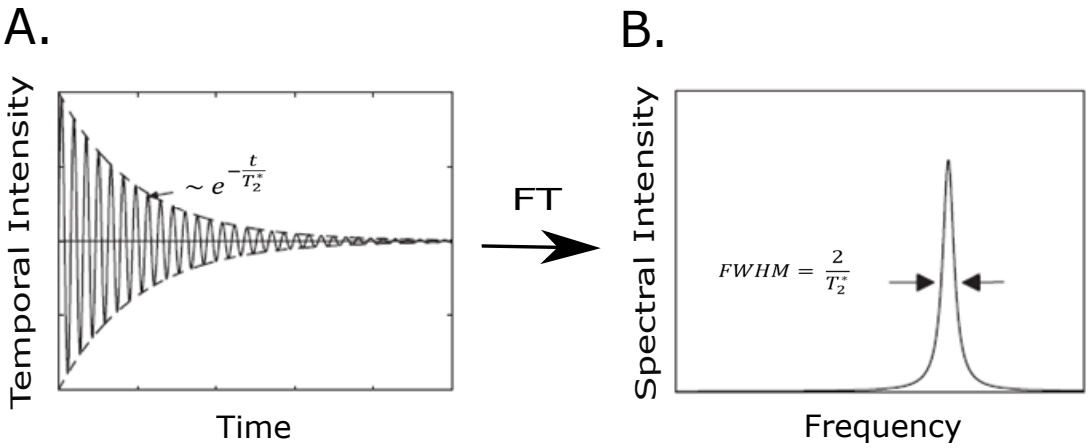

Figure 2.1: A monofrequency free induction decay (FID) with its typical damped sinusoidal form (2.1A) and its Fourier transformation which is a spectrum (2.1B) - Since the FID contains a single oscillatory frequency, a single peak is present in the spectrum. This figure was modified from reference [109].

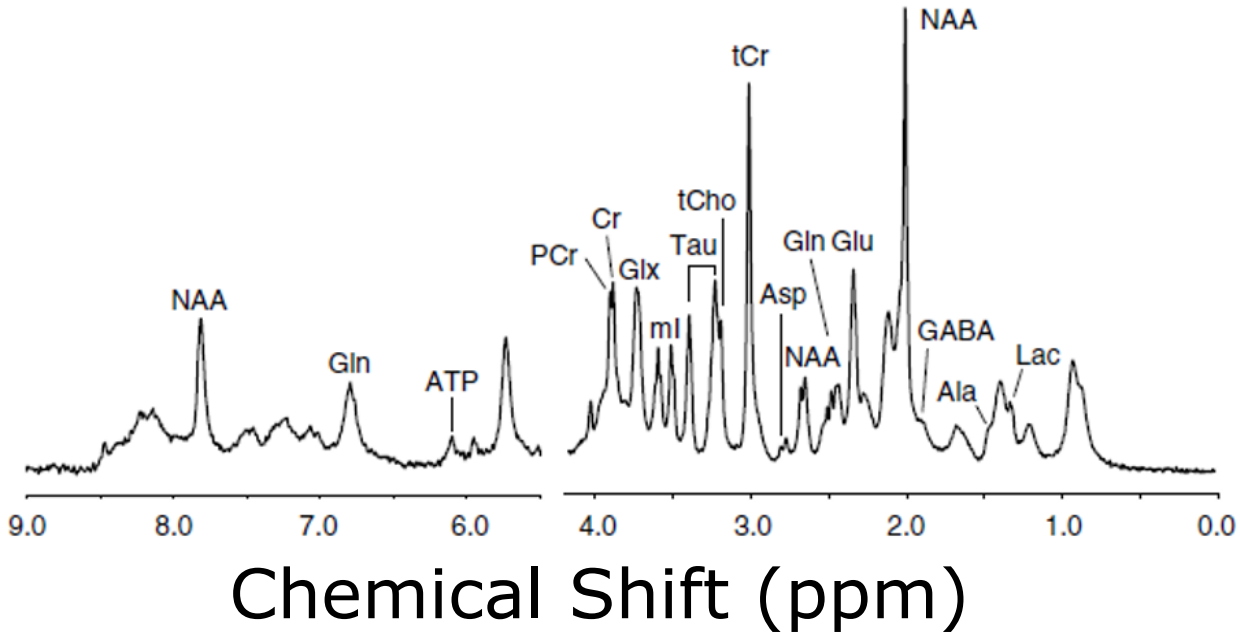

Figure 2.2: An exemplary *in vivo* ^{1}H spectrum of rat brain acquired at 11.75 T with the resonances of various metabolites labeled - This figure was modified from reference [61].

split into a multiplet [112]. The number of peaks into which a given resonance splits is determined by the number of equivalent protons attached to adjacent carbon atoms, which is a statement of the $N + 1$ rule [113].

Chapter 3

Biomedical Considerations

3.1 Cancer Metabolism

Metabolism is the collection of all chemical and physical processes that occur within an organism and result in the biochemical processing of energy and materials [114]. Metabolism can be divided into two main categories: anabolism and catabolism. Anabolism necessarily requires the input of energy and is the construction of larger, more complex molecules starting with simpler ones. In contrast, catabolism results in the release of energy and is the breakdown of more complex molecules into simpler ones [115]. Enzymes catalyze most metabolic reactions, so the modulation of the activities of these enzymes crucially regulate metabolic activity [116].

Cancerous cells exhibit severely dysregulated metabolic properties [117], and this metabolic dysregulation is commonly considered one of the hallmarks of cancer [118]. Healthy differentiated cells usually catabolize energy through oxidative phosphorylation under normal conditions but then switch to anaerobic glycolysis in hypoxic environments [119]. On the other hand, tumor cells preferentially catabolize energy through glycolysis even in the presence of an abundant supply of oxygen. This aerobic glycolysis is very energy inefficient relative to oxidative phosphorylation [120]. In particular, four moles of adenosine triphosphate (ATP), the energy currency of living cells, are produced for each mole of glucose in aerobic glycolysis, as compared to thirty-six moles of ATP produced per mole of glucose in oxidative phosphorylation [121]. The upregulation of glycolysis in malignant cells leads to an increase in the production of lactic acid [122], a biological process which is the subject of intense investigation using 13C MRS with hyperpolarized pyruvate [123]. The observation that cancer cells preferentially undergo glycolysis is known as the Warburg effect since it was first described in 1925 by Warburg [46, 124] who went on to receive the Nobel prize in physiology or medicine for this work in 1931. In general, metabolism is downstream from genomics, transcriptomics, and proteomics [125], so observing tumor metabolism provides crucial insight into the biological processes underlying tumor progression. Moreover, studying tumor metabolism allows for both the diagnosis of cancer and the assessment of a tumor's therapeutic response.

3.2 The Neurochemical Profile

N-acetyl aspartate (NAA) is one of the most commonly observed metabolites in ^{1}H MRS. Despite a plethora of research investigating its possible role in neurometabolism [126, 127], its precise function is still not well understood [128]. It is mainly observed as a singlet at 2.01 ppm originating from its methyl group, but smaller resonances appear at 2.49 ppm, 2.67 ppm, 4.38 ppm, and 7.82 ppm, respectively [61]. Its concentration varies spatially throughout the brain [129]. In MRS it is used to detect neuronal loss since NAA concentration decreases in pathologies where neuronal density decreases such as stroke [130] and multiple sclerosis [131]. This is particularly true in an oncological setting, as NAA concentrations are known to decrease in gliomas [132]. NAA is a precursor to N- acetylaspartylglutamate (NAAG) which is a neurotransmitter [133]. The primary resonance of NAAG is a singlet located at 2.04 ppm arising from the protons in its acetyl group. Because of its proximity to the NAA resonance, it is difficult to resolve NAA and NAAG, although not impossible [134]. The concentrations of NAAG across the brain also vary significantly but are usually within 0.6 mM to 3.0 mM [61].

Creatine (Cr) and phosphocreatine (PCr) are neurometabolites that are involved in energy metabolism [135]. In particular, PCr acts as an energy buffer [136] in maintaining adenosine triphosphate (ATP) levels by regenerating ATP from adenosine diphosphate (ADP). It also acts as an energy shuttle between the mitochondria, where the ATP is produced [137], and the site of energetic utilization in the cytoplasm. Being very similar in chemical structure, the resonances of Cr and PCr are located very close to each other on a proton spectrum; thus, they are difficult to resolve and often quantified together as total creatine (tCr). The prominent resonance of total creatine is a singlet at 3.03 ppm originating from the sole methyl group, but there is also a singlet at 3.92 ppm originating from the methylene group. The *in vivo* concentrations in the human brain of Cr and PCr are 4.5 mM to 6.0 mM and 4.0 mM to 5.5 mM, respectively, with slightly higher concentrations found in gray matter as compared to white matter [61]. Total creatine concentrations are relatively stable in the presence of most pathologies [138], so it is often used as a relative concentration reference, but this usage remains controversial [139]. Total creatine concentrations are observed to decrease in brain tumors [140].

One of the most prominent resonances in proton spectroscopy is that of total choline (tCho) which is comprised of contributions from free choline, phosphorylcholine, and glycerophosphorylcholine (GPC) [141]. There is a conglomeration of peaks arising from tCho located at approximately 3.2 ppm, although each compound possesses a number of smaller resonances to the left of the dominant peak. Concentrations of tCho are heterogeneous across the human brain but typically in the range of 1 mM to 2 mM [142]. Compounds containing choline aid in the synthesis and degradation of phospholipids and are thus involved in membrane turnover [143]. Choline concentrations have been observed to increase in a number of pathologies such as multiple sclerosis [144], Alzheimer's disease [145], and cancer [146].

Lactate, as discussed in Section 3.1, is the end product of glycolysis. Since glycolysis is strongly upregulated in tumorous tissue, its concentration increases in tumors [147]. Increases in lactate concentration are also observed during an ischemic stroke [148], functional activation [149], hyperventilation [150], and under hypoxic conditions [151]. Lactate's primary resonance, arising due to the protons in its methyl group, is a doublet located at 1.31 ppm, but there also exists a quartet located at 4.10 ppm arising due to the single proton in the methine group. Detection of lactate in proton spectroscopy is

nontrivial since the methyl peak overlaps with a large lipid signal and was not accomplished in this work. The normal *in vivo* concentration of lactate is approximately 0.5 mM [61].

Glutamate is the most abundant excitatory neurotransmitter in the human brain [152] and is the precursor to gamma aminobutyric acid (GABA) [153], which is important in reducing neuronal excitability in the human nervous system [154]. Glutamate is also vital in the synthesis of some smaller metabolites along with larger peptides and proteins [155]. Closely related to glutamate is glutamine. Neurons release glutamate or GABA which is then subsequently taken up by astrocytes [156]. The astrocytes then release glutamine which is taken up by the neurons [157]. This metabolic pathway is known as the glutamate-glutamine cycle [158]. Glutamate and glutamine have a similar chemical structure with both molecules possessing two methylene groups and a methine group. Therefore, the proton spectrum of the two molecules are quite similar, so the combination of glutamine and glutamate is typically quantified and referred to as Glx. The methine proton resonates as a doublet of doublets at 3.75 ppm and a triplet at 3.76 ppm for glutamate and glutamine, respectively. The methylene protons form multiplets located between 2.04 ppm and 2.35 ppm for glutamate and between 2.12 ppm and 2.46 ppm for glutamine. GABA has three methylene groups which produce triplets at 2.28 ppm and 3.01 ppm and a quintet at 1.89 ppm [61]. *In vivo* glutamate concentrations vary between 6 mM and 12.5 mM with significant differences observed between white and gray matter [159]. Glutamine concentrations are a bit lower, typically between 2 mM and 4 mM [160]. Glutamate is believed to be a tumor growth factor [161], and glutamate concentration has been observed to increase in the peripheral region of glioblastoma tumors [162]. Glutamine is known to be rapidly consumed by cancer cells [163], a process that is dependent on numerous factors such as the tumor microenvironment, tissue type, or underlying genetic factors [164]. Glutamine metabolism in cancer has been interrogated via ^{13}C hyperpolarized MRS [165], and glutamine can alternatively be used as a metabolic imaging agent via positron emission tomography (PET) [166].

Three additional signals are present in proton spectroscopic studies that complicate the metabolite quantification process. The first of these is water which shows up as a large resonance at 4.7 ppm. Water suppression is discussed in Section 6.2. The next bothersome signal is the lipid resonance at approximately 1.5 ppm. While it is true that dysregulated lipid metabolism may serve as a biomarker for cancer [167], the lipid signal observed in ^{1}H MRS brain studies originates in the thin layer of pericranial lipids surrounding the skull and, therefore, should be suppressed. The removal of pericranial lipids is discussed further in Section 6.6. The final signal that must be considered is that of the macromolecules (MM) in the tissue, arising from proteins and membrane structures [1495-1496]. No less than ten MM resonances appear in the human brain [168], but it is not possible to assign the specific proteins from which the signals originate.

Chapter 4

Magnetic Resonance Imaging

4.1 Spatial Encoding and Slice Selection

MRI is made possible through the application of gradient magnetic fields. These gradient fields introduce small perturbations to the value of the magnetic field linearly along a given direction. Three separate gradient fields are applied, one along each of the three spatial dimensions. By appropriately combining these three gradients, a gradient field can be applied in any desired direction, endowing MRI with the ability to image in arbitrary planes [169]. The guiding principle of MRI is that by spatially perturbing the value of the magnetic field, one spatially perturbs the precessional frequency of the nucleus. Since they then oscillate at different resonant frequencies, it is possible to discriminate from where a given component of the NMR signal originates, a process known as spatial encoding. Therefore, when gradient fields are introduced, the Larmor frequency becomes spatially dependent, and Equation 2.12 is modified as follows:

$$\omega(\vec{r}) = \gamma(B_0 + \vec{G} \cdot \vec{r}) \tag{4.1}$$

Here, $\vec{r}$ is the spatial position, and $\vec{G}$ is the gradient field.

In conventional two-dimensional imaging, a slice of spins must first be excited. This is typically accomplished by applying an RF excitation pulse with a finite bandwidth. Since frequency scales linearly with position due to the application of the gradient field, the finite bandwidth corresponds to a finite slice along the direction of the gradient.

4.2 k-Space

MRI data is acquired in a spatial frequency domain called k-space. It is easily accessed since spatial frequency is proportional to gradient strength. In particular, if G_i is the gradient along the i^{th} dimension for $i \in \{x, y, z\}$, then one can calculate k_i as [62]:

$$k_i(t) = \gamma \int_0^T G_i(t)dt \tag{4.2}$$

Here, the gradient is taken to have been turned on from 0 to T.

Following slice selection, data are acquired by applying gradients in the orthogonal directions to traverse k-space. The gradient in one in-plane dimension is referred to as the frequency encoding gradient or the readout gradient, while the gradient in the other in-plane direction is typically called the phase encoding direction. Trajectories through k-space can be Cartesian [170], spiral [171], radial [172], or follow a zig-zag pattern [173]. Once k-space is populated, an anatomical image of the spin density can be produced by taking a multidimensional discrete inverse Fourier transformation. More precisely, in the case of three-dimensional imaging, one can find the desired spin density ρ from the measured k-space data s via the following relation [63]:

$$\rho(\vec{r}) = \iiint_{k-space} s(\vec{k}) e^{2\pi i \vec{k}\cdot\vec{r}} d^3k \tag{4.3}$$

4.3 Signal-To-Noise

MRI is considered a low-sensitivity imaging modality [174]. In particular, at conventional clinical field strengths, only a handful more spins out of a million will populate the lower energy state relative to the higher energy state and ultimately contribute to the measured signal [986]. This sensitivity issue is circumnavigated by the fact that most clinical applications target hydrogen atoms in water molecules due to the relatively high natural abundance of such hydrogen atoms in the human body. However, this advantage is neutralized when it is desired to interrogate hydrogen atoms not in water molecules or nonhydrogeneous nuclei.

The MRI signal is proportional to the spin density [175] in the region of interest and the third power of the nucleus' gyromagnetic ratio [176]. The signal is inversely proportional to the temperature of the system [177] and is approximately proportional to the square of the magnetic field strength, although this dependence subquadratic as B_0 increases [178]. The spin density is a fundamental property of the tissue being examined and cannot be altered. The gyromagnetic ratio is dependent on the nucleus being probed and is largest for hydrogen. The temperature cannot be adjusted either since MRI need be performed at physiological temperature. The only adjustable parameter that increases the MRI signal is the external field strength, which explains the trend in recent years to push to higher field strengths [179]. The use of phased array coils also increases SNR since each individual element only detects signals from local regions and, thus, ignores the noise arising in further regions. In addition, surface coils have a high coupling to tissue.

Noise is ever present in any MR experiment, originating mainly from random thermal fluctuations in the electronics of the receiver coil and the sample [180]. These fluctuations are characterized by a Rician distribution which is the probability distribution of the amplitude of a bivariate circular normal random variable with a mean that does not necessarily vanish [181]. If A is the noise-free pixel intensity, M is the measured pixel intensity and σ^2 is the variance of the signal, then the probability distribution ρ for the intensity M is given by [182]:

$$p_M(M) = \frac{M}{\sigma^2} e^{\frac{-(M^2+A^2)}{2\sigma^2}} I_0\left(\frac{AM}{\sigma^2}\right) \tag{4.4}$$

Here, I_0 is the modified zeroth order Bessel function of the first kind. By inspecting Equation 4.3, it is seen that for small $\frac{A}{\sigma}$ (high noise), the probability distribution is given by a Rayleigh distribution [183], but for $\frac{A}{\sigma} > 3$ (decreasing noise), it starts to approach a Gaussian distribution [184].

The deleterious effects of noise in MRI, as in numerous other fields of signal processing, can be quantified via the signal-to-noise ratio (SNR). If S is the mean signal intensity, then the SNR is defined as:

$$\text{SNR} = \frac{S}{\sigma} \tag{4.5}$$

There exists a complex interrelationship between SNR, spatial resolution, and image acquisition duration, as one parameter is typically improved at the expense of the others [185]. For example, acquiring N datasets and averaging them will increase the SNR by $\sqrt{N}$ but will double the acquisition duration.

4.4 Contrast

In order to generate contrast in MRI one must exploit a difference in some MR-observable parameter. Some common examples include proton density, tissue relaxation properties, diffusion, perfusion, chemical exchange, and magnetic susceptibility. The two most commonly employed contrast mechanisms in clinical MRI are T_1 and T_2. The mechanism behind these tissue relaxation properties was discussed in detail in Section 2.4, and the basis for T_1 and T_2 contrast are discussed below for the illustrative example of a spin echo sequence.

In a spin echo experiment [26], one of the most utilized MRI pulse sequences, a 90° pulse initially rotates the magnetization into the transverse plane. The spins are then allowed to dephase but after some time, $\frac{TE}{2}$, a 180° pulse is applied and the spins rephase and form an echo at the echo time (TE). This procedure is then serially repeated after each repetition time (TR). The signal S of a spin echo experiment is proportional to the following quantity:

$$S \propto (1 - e^{-\frac{TR}{T_1}})e^{-\frac{TE}{T_2^*}} \tag{4.6}$$

When TR is long

$$\text{Long } TR \Rightarrow e^{-\frac{TR}{T_1}} \rightarrow 0 \tag{4.7}$$

and the contrast's dependence on T_1 is reduced. Similarly, when TE is short

$$\text{Short } TE \Rightarrow e^{-\frac{TE}{T_2^*}} \rightarrow 1 \tag{4.8}$$

and the contrast's dependence on T_2 is reduced. Thus, to produce a T_1-weighted image, both TE and TR should be short, while to produce a T_2-weighted image, both TE and TR should be long. To produce a proton-density image, the effect of both T_1 and T_2 relaxation need be reduced, so TR should be long and TE should be short.

Roughly 50% of all MRI examinations worldwide are contrast-enhanced [186], most of which are gadolinium based [187]. Gadolinium is paramagnetic and, thus, becomes magnetized in the presence of a magnetic field. The gadolinium accumulates in tissue, shortens its T_1, and consequentially renders it bright in a T_1-weighted image [188]. Gadolinium also shortens T_2 [189], but this effect is less pronounced since T_1 is typically much longer than T_2 *in vivo*.

The contrast-to-noise ratio (CNR) is defined as the difference in mean signal intensities between a tissue S_t of interest and a reference tissue S_{ref} relative to the noise σ [190]:

$$CNR = \frac{|\bar{S}_t - \bar{S}_{ref}|}{\sigma} \tag{4.9}$$

4.5 Magnetic Resonance Spectroscopic Imaging

Magnetic resonance spectroscopic imaging (MRSI) combines the features of unlocalized NMR spectroscopy discussed Section 2.7 and the localization techniques employed by MRI discussed in Section 4.1. It was developed in the early 1980's, and the initial *in vitro* [191, 192] and *in vivo* [193, 194] applications were soon to follow.

MRSI is analogous to MRI except that at each point in k-space, an FID is acquired rather than a single complex datapoint. Thus, an FID is read out at each point as a series of phase encoding steps are iterated through each spatial direction. Each phase encoding step has a temporal duration of TR. The readout of the FID captures the spectroscopic information, while the sequence of phase encoding gradients performs spatial encoding. Consider an MRSI experiment in three spatial dimensions. For the sake of simplicity, assume that the sampling rate is infinite so that the signal can be described as a continuous function. Also assume that the region of interest is the entirety of space, and the measurement duration is throughout all of time. A time-dependent signal $S(t)$ is acquired from the coil and is the sum of each signal arising in volume elements $s(x, y, z, t)dxdydz$ from each spatial location (x, y, z) in the region of interest:

$$S(t) = \int_{-\infty}^{\infty}\int_{-\infty}^{\infty}\int_{-\infty}^{\infty} s(x, y, z, t)dxdydz \tag{4.10}$$

When gradients are applied, a set of FIDs in k-space can be acquired and subsequently transformed into a set of spectra in k-space F:

$$F(k_x, k_y, k_z, \omega) = \int_{-\infty}^{\infty} S(k_x, k_y, k_z, t)e^{-i\omega t}dt \tag{4.11}$$

The set of spectra in image space f can then be found from F by taking the three-dimensional Fourier transformation from k-space into image space.

$$f(x, y, z, \omega) = \int_{-\infty}^{\infty}\int_{-\infty}^{\infty}\int_{-\infty}^{\infty} F(k_x, k_y, k_z, \omega)e^{-i(k_x x + k_y y + k_z z)}dk_x dk_y dk_z \tag{4.12}$$

The physical case proceeds analogously except that boundary conditions are placed on the temporal and spatial dimensions and the sampling is discrete in both time and space so that discrete Fourier transformations are applied rather than their continuous versions [61].

4.6 MRSI at Higher Fields

Most clinical scanners operate at magnetic field strengths of either 1.5 T or 3 T. In recent years, there has been a push to higher field strengths for a variety of MR-based applications and MRSI is no exception [195, 196, 197]. At higher field strength, SNR is increased, spectral dispersion is increased, and the effects of scalar coupling are reduced because of the regime change from a strongly coupled system to a weakly coupled system [198]. However, these benefits come with a number of challenges. For example, as one moves from 3 T to 7 T, B_0 inhomogeneities become more problematic since static field perturbations arising from magnetic susceptibility differences increase proportionally to B_0 [199]. B_1 inhomogeneities also become more problematic due to the fact that the wavelength of an RF pulse required to excite a spin at 7 T is shorter than the dimensions of the human skull [200]. A further challenge is the shorter T_2 relaxation which must be compensated by using very short echo times [201].

Despite the many challenges it is still advantageous to perform MRSI at higher field strength, so the entirety of this work is performed at 7 T. With the aforementioned improvement in spectral resolution at higher fields, relative, single-voxel *in vivo* concentrations of approximately twenty [198] neurometabolites can be assessed, although these are not all detected in this work. Some of the more important of these were discussed above in Section 3.2. The benefits and disadvantages of MRSI at higher field strength are also discussed in Section 8.1.1.

Chapter 5

Parallel Imaging

5.1 Acceleration of MRSI

As discussed in Section 4.5, MRSI has the ability to produce high-resolution metabolite maps in a non-invasive manner. This is extremely useful in an oncological setting due to the dysregulated metabolic phenotype expressed by malignant cells. Metabolic images can aid in tumor diagnosis. Also, since MR does not employ ionizing radiation, metabolic images can be acquired serially and thus be used to monitor a tumor's therapeutic response.

Despite this tremendous potential, MRSI has not been fully adopted into routine clinical practice [202]. Although there are numerous challenges associated with MRSI, the major limitation of its clinical implementation is the excessively long scan times required for data acquisition [203], as MRSI examinations with a modest imaging matrix of 64×64 can often take upwards of one hour. This is because MRSI requires the acquisition of an extra dimension of data, the temporal dimension, as compared to MRI. In addition, a long TR is typically used in MRSI in order to achieve sufficient spectral resolution. The combination of the long TR and the full phase-encoding requirements impose extremely long acquisition durations. Therefore, the main objective of this project was to reduce the required acquisition duration for an MRSI examination and thus increase the feasibility of MRSI's routine clinical adoption.

The acceleration of image acquisition can be accomplished via parallel imaging which decreases the time needed for acquisition by utilizing information regarding the spatial distribution and sensitivities of the individual receiver coil elements in a phased array. Image reconstruction is thereby converted from a direct Fourier transformation to the solution of an ill-conditioned inverse problem [204]. As discussed in great detail in the following section, parallel imaging can be superficially subdivided into two main categories: those that are performed in k-space and those that are performed in image space. The parallel imaging techniques that are performed in k-space conventionally require the full acquisition of one of the spatial dimensions to calculate the coil weighting factors, but since MRSI additionally acquires a fully-sampled temporal dimension, this requirement may no longer be necessary. In this work, a novel technique to perform k-space-based parallel imaging using only the time domain data to calculate the coil weighting factors is presented. This ARTT GRAPPA parallel imaging technique allows for greater flexibility in potential sampling patterns, exploits spatial-spectral correlations in the data, and, ultimately, allows for more aggressive undersampling schemes.

5.2 General Principles of Parallel Imaging

The major limitation preventing the widespread adoption of ^{1}H MRSI into clinical practice is the extremely long time required to acquire MRSI data, as high-resolution MRSI examinations can often take upwards of one hour. The reduction of acquisition time has long been a focus in MRI research [205]. Numerous fast MRI techniques have been developed and applied ubiquitously in the literature in a variety of applications. These include echo planar imaging (EPI) [43], fast low-angle shot (FLASH) [206], and turbo spin echo (TSE) [207]. These fast image acquisition techniques have revolutionized the magnetic resonance field and have been applied to accelerate MRSI. In particular, echo planar spectroscopic imaging (EPSI) has been utilized in proton MRSI [208, 209, 210], phosphorus MRSI [211], and hyperpolarized carbon MRSI [212]. Due to the nature of how spatial encoding is accomplished in these fast MRI techniques, rapidly switching gradients are required to achieve further acceleration. Although gradient performance has improved markedly in recent decades, these fast MRI techniques still exhibit methodological and hardware limitations [213].

Parallel imaging allows for image acquisition acceleration without the reliance on increased gradient performance. By contrast, parallel imaging decreases the time needed for acquisition by utilizing information regarding the spatial distribution and sensitivities of the individual receiver coil elements in a phased array. A phased array is an array of individual coil elements which are fed into separate receiver chains and spatially distributed around the anatomy of interest [214]. Surface coils, which are small coils placed directly on the surface of the patient as close as possible to the anatomy of interest, typically have a high SNR but limited anatomical coverage [215]. By combining many small surface coils together and arranging them around the anatomy of interest in a phased array, one achieves both a high SNR and a large field coverage [216]. The only disadvantage of using a phased array compared to a single channel coil is that the final images acquired from a phased array exhibit an inhomogeneous SNR distribution [214].

These individual surface coils in the array have both different sensitivities and different spatial positions, and this spatial sensitivity information can allow for the reduction in MRI acquisition duration [217]. Normally in MRI, when phase encoding lines are skipped during the filling of k-space, acquisition duration is reduced but marked aliasing or wrap-around artifacts [218] are introduced. Aliasing artifacts are errant features in an MR image that appear when the FOV is smaller than the object being imaged. It reflects the fact that the spacing between adjacently acquired k-space lines is too small to properly resolve frequencies from different locations within an object [219]. Normally, in order to avoid aliasing effects, the Nyquist criterion must be satisfied, mandating that the sampling rate must be greater than or equal to twice the highest frequency contained in the signal [220]. In MRI the Nyquist criterion restricts the maximum allowable spacing between successive k-space phase encoding lines [221] which, for a given spatial resolution, fixes the number of required phase encoding lines. Thus, since image acquisition duration is proportional to the number of phase encoding lines acquired, the Nyquist criterion fixes the image acquisition time for a given TR. Parallel imaging allows one to accelerate image acquisition duration past the minimum time imposed by the Nyquist limit and largely minimizes these aliasing effects by using the spatial sensitivity profile of the phased array to reconstruct the missing data.

The coil sensitivity of a single channel is a function of three-dimensional position. At a given point

in space, it describes how sensitive that coil is at that position. These sensitivities, which depend on the coil loading [222], the interaction of the patient with the RF coil, may vary from patient to patient. Thus, one cannot simply determine the sensitivity profile once and blindly apply it for each measurement; it must be determined on an individual basis. Moreover, since parallel imaging makes use of differences in coil sensitivities, one can only accelerate along dimensions for which there are sufficient coil sensitivity variations. For example, if an array were geometrically constructed so that it consisted of n coils arranged in a line along the y direction, then acceleration would only be possible along the y direction, not the x or z directions. Therefore, the geometry of the array, by dictating the coil sensitivity profile, determines the acceleration that can be achieved in the implementation of parallel imaging.

5.3 SENSE

There are two main flavors of parallel imaging reconstructions: image space-based reconstructions and k-space-based reconstructions. The main image space-based reconstruction technique is sensitivity encoding (SENSE) [223], which has been applied ubiquitously in the literature for a variety of applications [224, 225, 226], including MRSI [227, 228, 229, 230, 231]. Other image space-based reconstructions such as parallel imaging with localized sensitivities (PILS) [232] have been developed but have not been significantly applied in the literature. In image space-based techniques, the coil sensitivity maps must be known *a priori*, which is typically accomplished via a prescan prior to the MRI examination.

The SENSE reconstruction algorithm works as follows. Assume that the phased array has M coils and that there are $N = XY$ pixels in a two-dimensional image, where X and Y are the number of pixels in both of the principal directions. Let the coil sensitivity profile form an M by N matrix S such that the ijth element S_{ij} indicates the sensitivity of the jth coil in the ith pixel. Furthermore, let F be an M-dimensional vector of complex-valued measured aliased signal intensities in each coil, and let Ψ be an M by M matrix that characterizes the noise in the acquisition channels. Thus, if the desired separated pixel values form an N-dimensional vector p, signal separation is performed via the following matrix equation:

$$\vec{p} = (S^{\dagger}\Psi^{-1}S)^{-1}S^{\dagger}\Psi^{-1}\vec{F} \tag{5.1}$$

Here, the superscript dagger denotes the Hermitian conjugate, and the superscript -1 denotes the matrix inverse. This procedure is then repeated for each pixel in the reduced FOV in order to reconstruct a non-aliased full-FOV image [223].

5.4 GRAPPA

The major k-space-based parallel imaging reconstruction technique is generalized autocalibrating partial parallel acquisition (GRAPPA) [233]. GRAPPA, like SENSE, has been applied ubiquitously in the literature for a variety of applications [234, 235, 236, 237], including MRSI [238, 239, 240, 241, 242, 243]. GRAPPA is the fourth generation of k-space-based parallel imaging reconstruction techniques and is the most generalized version of its predecessors: simultaneous acquisition of spatial harmonics (SMASH) [244], automatically calibrated simultaneous acquisition of spatial harmonics (AUTO-

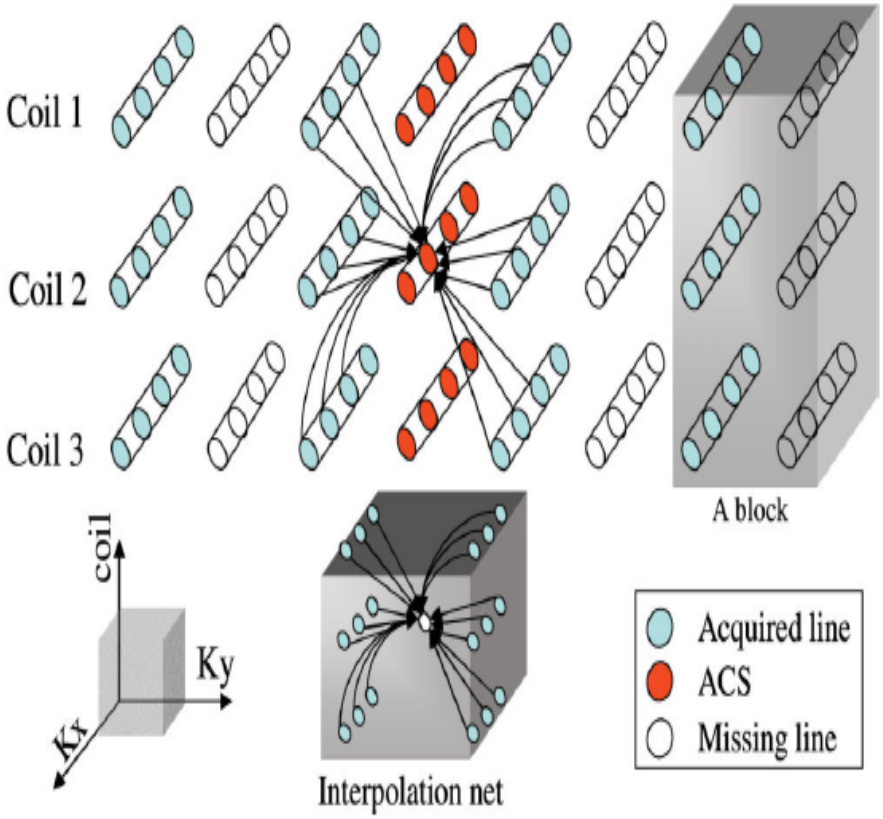

Figure 5.1: The interpolation net utilized in GRAPPA - A single ACS point is linked to each of its neighboring points throughout each coil. This interpolation net is then used to reconstruct the unsampled points in k-space. This figure was modified from reference [247].

SMASH) [245], and variable density automatically calibrated simultaneous acquisition of spatial harmonics (VD-AUTO-SMASH) [246].

Unlike SENSE, which requires an explicit determination of the coil sensitivity profile, GRAPPA is a data-driven approach which determines the coil sensitivity profile in an implicit fashion through the full acquisition of a central autocalibration region. GRAPPA is essentially a sophisticated interpolation technique that uses correlations between neighboring points in k-space and the calculated coil sensitivity profile to estimate the complex value of an unsampled k-space point had it been sampled. This procedure is repeated for each unsampled k-space point in each coil until a fully-reconstructed k-space exists for each channel in the array. After an appropriate coil combination algorithm and a multidimensional discrete Fourier transform, the reconstructed image is recovered.

The idea behind this procedure is illustrated in Figure 5.1, which was modified from a figure taken from Wang et al [247]. The red circles embedded inside white cylinders represent autocalibration signal (ACS) points, which are the fully-sampled points at the center of k-space and are used in the determination of the GRAPPA weights. The blue and white circles embedded inside white cylinders represent points belonging to fully-acquired k-space lines and unsampled k-space lines, respectively. In GRAPPA, an interpolation net is formed linking a single ACS point to its neighboring points

throughout each coil. This interpolation net extracts correlations in the composite spatial frequency-coil domain and is then used to reconstruct each unsampled point. Let R be the acceleration factor, which is defined as the integer spacing between successively acquired k-space lines in the undersampled peripheral region. Then a block, which is shown shaded in gray in the figure, is defined as a single acquired k-space line for each coil followed by $R-1$ unsampled k-space lines for each coil. Using this formalism, the GRAPPA algorithm can be expressed succinctly as follows [233]:

$$S_j(k_y - r\Delta k_y) = \sum_{l=1}^{N_c} \sum_{b=0}^{N_b-1} W(j,b,l,r) S_l(k_y - bR\Delta k_y) \tag{5.2}$$

Here, S_j is the signal to be obtained in line $k_y - r\Delta k_y$ for the jth coil, Δk_y is the sampling interval along the k_y direction, r is the ordinal line number of the missing data point in a block [247], S_l is the known signal in the lth coil, N_c is the number of coils, b is the block index, N_b is the number of blocks, and W contains GRAPPA weights. The indices j, b, l, and r run from 1 to N_c, N_b, N_c, and R, respectively.

5.5 The Implementation of GRAPPA

Because a thorough understanding of GRAPPA is essential for much of what is to follow, a more detailed description of the GRAPPA algorithm is presented here using conventional two-dimensional imaging as an illustrative example. The basic two-dimensional GRAPPA sampling scheme is shown in Figure 5.2, which was modified from a figure taken from Breuer et al [248]. The k_x dimension runs from left to right, and the k_y dimension runs from bottom to top. Here, the k_y dimension is the direction that is undersampled, and the k_x dimension is fully-sampled. Note that one dimension is always required to be fully-sampled in order to determine the GRAPPA weights. Therefore, the implementation of GRAPPA into N-dimensional imaging allows for undersampling along $N-1$ dimensions. In Figure 5.2, there are seven ACS lines, the acceleration factor is three, and the number of blocks is four. In this example, the product of R and N_b divided by the number of ACS lines (N_{ACS}) is less than two for illustrative purposes, but it is important to note that this value is typically larger, e.g., 2 to 5, allowing for greater overall acceleration.

The first step in a GRAPPA reconstruction is to fill so-called source and target matrices. A kernel is placed at the top left of the central autocalibration region, as shown in Figure 5.2. In this example, the kernel dimensions are $X_k = 3$ and $Y_k = 2$. The horizontal kernel dimension need be an odd number less than or equal to the number of points in the k_x direction. The vertical kernel dimension can be any number less than or equal to $N_{ACS} - 2$, but the reconstruction technique is easiest to understand when this dimension equals $R-1$, as in the example. At this kernel position, the six source points, or more generally the $2X_k$ source points, shown as small shaded circles inside larger circles, are extracted and placed into a source vector. Analogously, the two target points, or more generally the Y_k target points, shown as circles with a bold border, are extracted and placed into a target vector. The kernel is then translated horizontally to the right by some horizontal step size ΔS_x, and new source and target vectors are extracted. This procedure is repeated until the kernel cannot travel any further in the horizontal direction, at which point it is translated vertically downward by some vertical step size ΔS_y and then proceeds to travel back to the left. Thus, the kernel traverses the entire autocalibration region in the manner just described, extracting source vectors and target vectors at each of the N_k

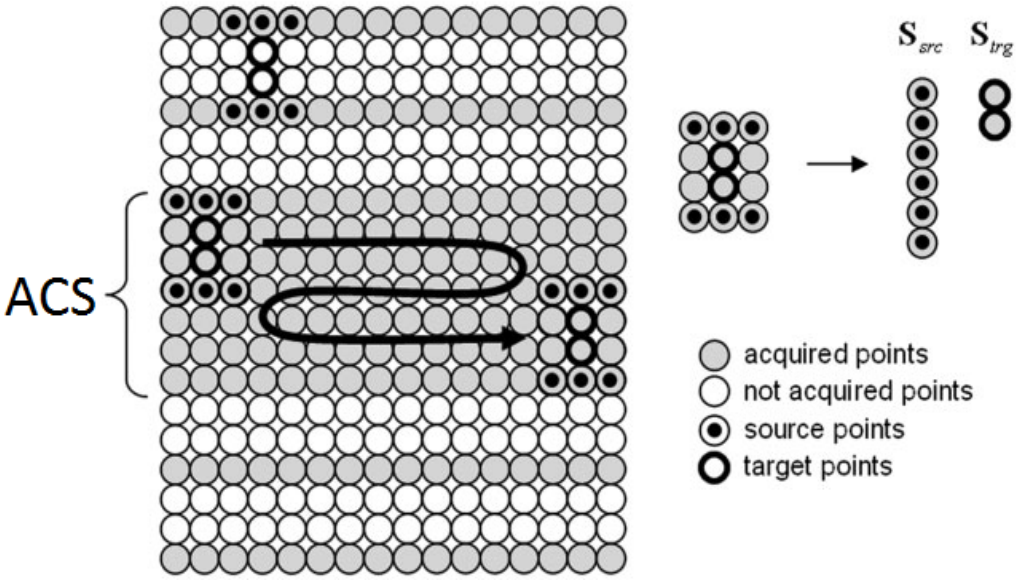

Figure 5.2: The basic GRAPPA reconstruction technique - The GRAPPA weights are determined by allowing a kernel to traverse the central autocalibration region. Once the GRAPPA weights are determined the unsampled k-space points can then be estimated. This figure was modified from reference [248].

kernel positions. Each source vector and each target vector are then appended horizontally to form a single-coil source matrix and a single-coil target matrix, respectively. The single-coil source matrix has dimensions $2X_k$ by N_k, and the single-coil target matrix has dimensions Y_k by N_k. Finally, this procedure is then repeated for each channel in the phased array, and each single-coil source matrix and each single-coil target matrix are appended vertically to form the source matrix S_{src} and the target matrix S_{trg}, respectively. Here, S_{src} has dimensions $2X_kN_c$ by N_k, and S_{trg} has dimensions Y_kN_c by N_k.

The next step in a GRAPPA reconstruction is the determination of the GRAPPA weights which implicitly hold the information regarding the coil sensitivity profile. The GRAPPA weights W are then found via the following equation:

$$\mathbf{W} = \mathbf{S}_{trg}\text{pinv}(\mathbf{S}_{src}) \tag{5.3}$$

Here, pinv is the Moore-Penrose pseudoinverse, which is a generalized version of matrix inversion [249]. The dimensions of W are Y_kN_c by X_kN_c, as it maps a given source point in channel i to a given target point in channel j for all pairs of channels i and j in the array. This can be more easily visualized in Figure 5.3. In this representation, W is a matrix of dimensions N_c by N_c where each element of W is itself a matrix of dimensions Y_k by X_k. Because the GRAPPA weights are calculated from a low-resolution dataset with sufficiently high SNR and a large number of kernel positions within the ACS, the use of the Moore-Penrose pseudoinverse results in GRAPPA weights that can be considered noise free [248].

Once the GRAPPA weights are determined, one can then estimate the missing points in the peripheral undersampled region of k-space. One first places the kernel in the undersampled region, as shown at

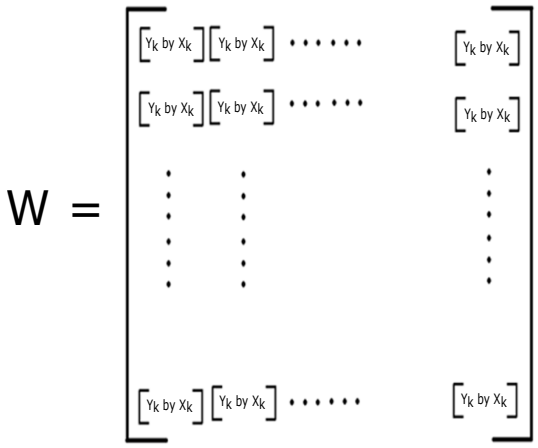

Figure 5.3: A schematic of the GRAPPA weights - The GRAPPA weights can be interpreted as an array of dimensions the number of coils by the number of coils with elements that are themselves arrays of dimensions the number of target points by the number of source points.

the top of Figure 5.2. In this figure, the target vector in the fourth column of the first block in the ith channel is being reconstructed. One first extracts the source vector S_j at the specified kernel position for each channel in the array using the same procedure as described above. Then the desired target vector T_i is reconstructed via the following equation:

$$T_i = \sum_j w_{ij} S_j \tag{5.4}$$

Here, the sum is taken over all channels, and w_{ij} is the ijth, Y_k by X_k submatrix of W. This procedure is then iterated for each target vector in each block in each channel until the entirety of k-space has been reconstructed.

5.6 SNR in Parallel Imaging

One drawback of parallel imaging is that it necessarily reduces the SNR. This is due to the fact that a parallel imaging-based examination acquires less data than a corresponding examination that does not use parallel imaging. In particular, the reduction of the SNR is described by

$$\mathrm{SNR}_{\mathrm{pi}} = \frac{\mathrm{SNR}_{\mathrm{normal}}}{g\sqrt{R}} \tag{5.5}$$

Here, $\mathrm{SNR}_{\mathrm{normal}}$ is the SNR of a normal, corresponding, non-parallel imaging study, and $\mathrm{SNR}_{\mathrm{pi}}$ is the SNR of the parallel imaging study. In addition, R is the acceleration factor, and g is the geometry factor which depends on the number and spatial distribution of the individual receiver coil elements, the loading of the coil, and the orientation of the imaging plane. In addition, this geometry factor varies throughout the image but typically is between 1 and 2 [248].

The influence of Equation 5.5 can be seen in Figure 5.4 where the $\frac{\mathrm{SNR}_{\mathrm{normal}}}{\mathrm{SNR}_{\mathrm{pi}}}$ is plotted against $\sqrt{R}$. These data were acquired in the retrospectively undersampled *in vivo* analysis described below in Section 6.8.3. The average SNR of each spectrum throughout the brain of a healthy volunteer was

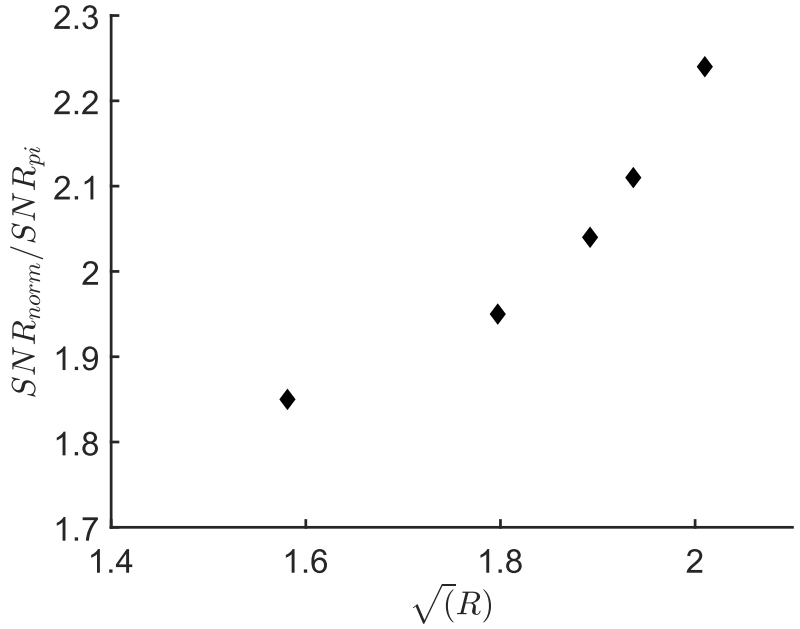

Figure 5.4: The degredation of SNR in parallel imaging with increasing acceleration factor.

measured for both the fully-sampled dataset and a series of retrospectively undersampled reconstructed datasets. Here, it can be seen that $\frac{\mathrm{SNR}_{\mathrm{normal}}}{\mathrm{SNR}_{\mathrm{pi}}}$ varies approximately linearly with $\sqrt{R}$ and that g is slightly greater than unity.

Chapter 6

Materials & Methods

6.1 Scanner and Coils

All measurements were performed at the German Cancer Research Center on a 7 Tesla whole-body MAGNETOM MRI scanner (Siemens Healthineers, Erlangen, Germany). The scanner used in this work is displayed in Figure 6.1A, which was modified from a figure taken from Windschuh [250]. The static magnetic field is $B_0 = 6.98$ T which corresponds to a proton resonance frequency of 297.15 MHz. The system is equipped with a set of three mutually perpendicular gradients each with a maximum strength of 28 mT/m and a slew rate of 170 mT/m/s [251]. A twenty-four channel receive head coil coupled with a birdcage coil for transmission [252], shown in Figure 6.1B, was used for all measurements.

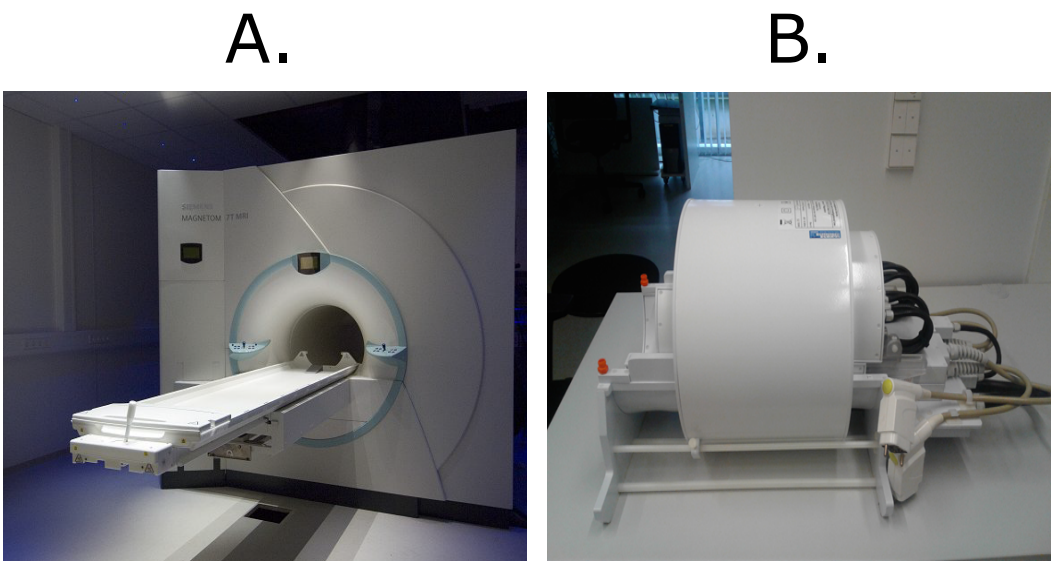

Figure 6.1: The 7 Tesla whole-body MAGNETOM MRI scanner (6.1A) and the 24-channel receive head coil (6.1B) used in this work - Figure 6.1 A was modified from reference [250].

6.2 Water Suppression

6.2.1 Water Suppression Introduction

Water, consisting of two hydrogen atoms, appears in a proton spectrum as a peak located at approximately 4.7 ppm. It can be three to four orders of magnitude larger than the peaks arising from the metabolites of interest. Although modern analog-to-digital converters can adequately discriminate these low metabolite signals, the presence of the large water peak can lead to distortions of the spectral baseline and errant signals arising from vibration-induced signal modulation [61]. These distortions render the metabolite detection process unreliable [253]. Therefore, most proton spectroscopic applications implement some type of water suppression technique.

6.2.2 Chemical Shift Selective Pulses

Frequency selective RF pulses are the most commonly applied means of suppressing water. Here, a spectrally selective RF pulse excites all spins within the specified frequency band which are then subsequently dephased using a spoiler gradient. These chemical shift selective (CHESS) pulses [254] are able to precede any arbitrary pulse sequence and do not modulate the metabolite peaks outside of the designated frequency band. A single CHESS pulse would adequately suppress water in the presence of homogeneous B_0 and B_1 fields. In practice, however, both B_0 [255, 256] and B_1 [257] are inhomogeneous, so the CHESS pulse is repeated multiple times. This will broaden and flatten the frequency range centered about the water frequency, reducing the technique's sensitivity to B_0 inhomogeneities. In addition, B_1 insensitivity is achieved since the residual longitudinal magnetization following n CHESS pulses is given by the relation [61]:

$$M_z(\alpha) = M_{z,0}(\cos\alpha)^n \tag{6.1}$$

Here, $M_{z,0}$ is the initial longitudinal magnetization at the start of the CHESS sequence, and α is the achieved flip angle. Because of the exponential dependence on the number of CHESS pulses, flip angles differing from $\frac{\pi}{2}$ will have less of an effect on the water suppression scheme.

Numerous CHESS-based techniques have been applied in the literature, including water suppression enhanced through T_1 effects (WET) [258], multiply optimized insensitive suppression train (MOIST) [259], suppression of water with adiabatic modulated pulses (SWAMP) [260], and low-power water suppression by hyperbolic secant pulses with controlled offsets and delays (WASHCODE) [261]. These approaches differ in the number of CHESS pulses applied, the amplitude and shape of the CHESS pulses, and the delay times separating each pulse. In addition, three techniques have been applied in the literature where water suppression is applied after excitation, during a following spin echo period. These include water suppression by gradient tailored excitation (WATERGATE) [262], excitation sculpting [263], and Mescher-Garwood (MEGA) [264]. However, these frequency selective refocusing approaches were not used here because they necessarily increase the required echo time, and a short echo time approach is desirable since it avoids the degradation of spectral information due to T_2 relaxation and J-coupling effects. Thus, it was decided to employ a CHESS-based technique prior to excitation.

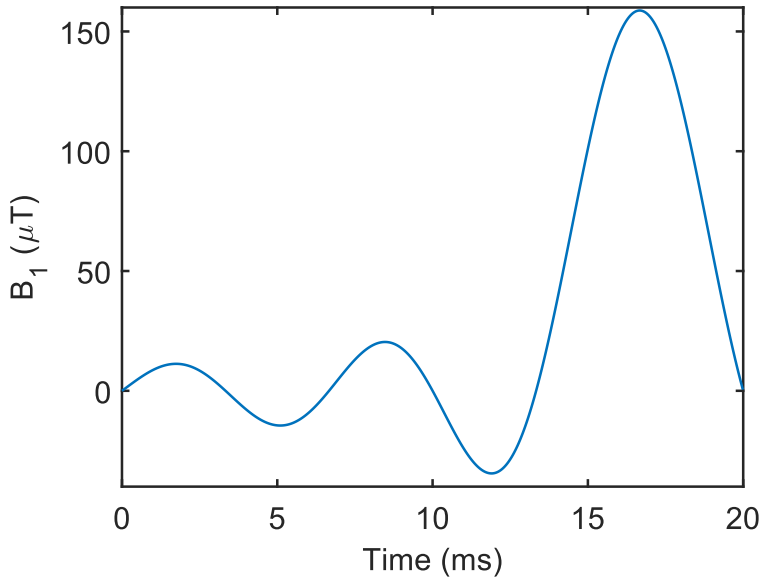

Figure 6.2: The asymmetric sinc shape of a single VAPOR pulse - The strength of the B_1 field is expressed in μT, and the pulse length is 20 ms.

6.2.3 VAPOR

Variable power radiofrequency pulses with optimized relaxation delays (VAPOR) is a CHESS-based water suppression technique that has been optimized for insensitivity in the presence of B_1 inhomogeneities [265]. Its application is ubiquitous in the literature.

VAPOR consists of seven CHESS pulses each with the shape of an asymmetric *sinc* function. In the implementation here, the temporal extent of the pulse could be adjusted by the user within the range of 5 ms to 30 ms. The *sinc* pulse had five lobes in total; 4.5 lobes were to the left of the maximum point, while one half of a lobe was to the right of the maximum point. In Figure 6.2, a single VAPOR pulse is shown, illustrating its asymmetric *sinc* shape. In this figure, the pulse length is 20 ms, and the prescribed RF power profile is given in units of μT. In the VAPOR scheme, the seven interpulse delay times were 150 ms, 80 ms, 160 ms, 80 ms, 100 ms, 30 ms, and 26 ms, respectively. The flip angle α of a single pulse of length T_p was calculated via the following relation:

$$\alpha = \gamma \int_0^{T_p} B_1(t)dt \tag{6.2}$$

Here, γ is the gyromagnetic ratio of the proton given in Equation 2.7. Equation 6.2 is the generalization of Equation 2.25 for an arbitrarily shaped pulse. The prescribed RF power of the first, second, fourth, and sixth pulse was chosen so that the flip angle was $\frac{\pi}{2}$. The prescribed RF power of the third, fifth, and seventh pulses were a factor of 1.78 larger than that of the previously described group. The entire VAPOR pulse train is displayed in Figure 6.3, where the amplitude A shown in the figure is that which will ensure a $\frac{\pi}{2}$ flip angle, as calculated via Equation 6.2. As in Figure 6.2, the pulse length was chosen to be 20 ms, and the prescribed RF power profile is given in units of μT.

Following each VAPOR pulse, a spoiler gradient was applied to null the transverse magnetization.

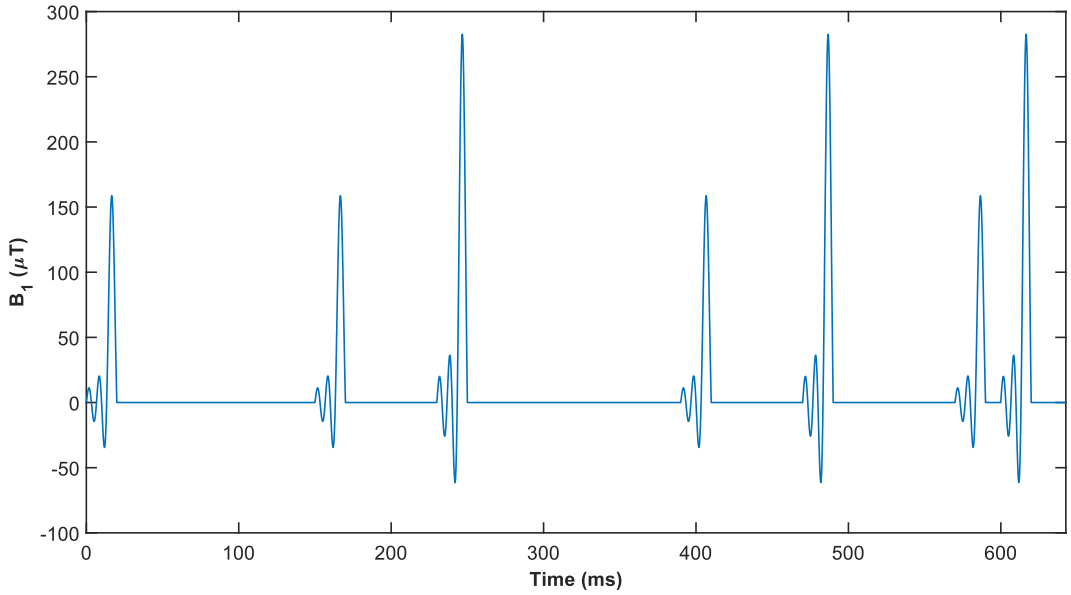

Figure 6.3: The VAPOR pulse train - VAPOR consists of seven asymmetric *sinc*-shaped CHESS pulses with optimized amplitudes and interpulse delay times.

When designing the spoiler gradient pulses, care needed to be taken in order to avoid unwanted echoes that can form and distort the peak amplitudes and lineshapes in a spectrum [266]. In order to think about this problem, it can be helpful to introduce the concept of coherence first formulated by Bodenhausen et al [267]. Coherence is a generalization of the concept of transverse magnetization. In particular, it can describe an arbitrary transition between any pair of eigenstates, r and s, in a system. Transverse magnetization corresponds to the specific subset of coherence for which the order of coherence equals positive or negative unity. Here, the order of coherence [268] is defined as the difference in magnetic quantum numbers between the two states: M_r–M_s.

A gradient pulse G_ζ applied in the direction ζ for a time duration δ induces an acquired phase ϕ across a voxel of

$$\phi = p\gamma G_\zeta \delta \Delta r_\zeta \tag{6.3}$$

Here, p is the order of coherence, γ is the gyromagnetic ratio of the proton, and Δr_ζ is the voxel dimension in the ζ direction, where ζ can be either of the three spatial dimensions. Analogously, when the sequence of a VAPOR pulse and subsequent gradient spoiling is repeated n times, the phase gained during the entire sequence is

$$\Phi_\zeta = \sum_n \phi_n = \gamma \Delta r_\zeta \sum_n p_n G_{\zeta,n} \delta_n \tag{6.4}$$

If $\phi_{\zeta,min}$ describes the minimum accumulated phase required for sufficient dephasing in a single pulse experiment, then echoes are sufficiently dispersed if

$$\Phi_\zeta \geq \phi_{\zeta,min} \tag{6.5}$$

Since the magnitude of each component of the order of coherence vector appearing in Equation 6.4 must be less than or equal to unity, it can be seen that the requirement of Equation 6.5 can be satisfied by doubling the magnitude of each subsequent gradient moment along a given direction [269]. Since there are seven VAPOR pulses, adequate spoiling can be accomplished with the following set of gradient amplitudes:

$$G \in \{\mu G_{x,min}, 2\mu G_{x,min}, \mu G_{y,min}, 2\mu G_{y,min}, \mu G_{z,min}, 2\mu G_{z,min}, 4\mu G_{z,min}\} \tag{6.6}$$

Here, μ is some arbitrary constant greater than or equal to unity in place to ensure that the employed gradient amplitudes are at least the minimum required gradient amplitude to achieve sufficient dephasing in a single pulse experiment. In addition, for simplicity, it was assumed that the gradient duration δ is the same for each spoiler gradient. The slice direction was chosen as the dimension with three spoiler gradients since spoiling is optimal along the largest voxel dimension.
To find the minimum required gradient amplitude, Equation 6.3 can be modified to give

$$|\Delta\phi_{min}| = \gamma G_{\zeta,min}\delta\Delta r_\zeta \tag{6.7}$$

which can be rearranged to yield

$$G_{\zeta,min} = \frac{|\Delta\phi_{min}|}{\gamma\delta\Delta r_\zeta} \tag{6.8}$$

Here, the minimum phase dispersion $|\Delta\phi_{min}|$ can be taken to be 4π [270]. Using a voxel dimension of 5 mm and a gradient duration of 20 ms, one finds a minimum required gradient amplitude of 1.9 mTm^{-1}. Since this amplitude is substantially less than the technical limits imposed by modern gradient performance, a relatively large μ of 2.6 was chosen so that the three employed gradient amplitudes were 5, 10, and 20 mTm^{-1}. In addition, since MR gradients are slew rate limited, a ramp time of 300 μs was used. This ramp time corresponds to a slew rate of 67 $\mathrm{Tm}^{-1}\mathrm{s}^{-1}$, well within the slew rate performance capabilities of modern MR systems. An example of the various radiofrequency pulse and gradient parameters employed for each of the seven pulses is summarized in Table 6.1 and Table 6.2, respectively.

Pulse Number	Desired Pulse Amplitude (μT)	Pulse Length (ms)	Delay Time (ms)
1	1.59	20	150
2	1.59	20	80
3	2.83	20	160
4	1.59	20	80
5	2.83	20	100
6	1.59	20	30
7	2.83	20	26

Table 6.1: Shown are the various VAPOR pulse parameters employed in this work.

6.2.4 Water Suppression Simulations

Prior to implementation, simulations were performed to track the evolution of the magnetization throughout the VAPOR scheme. Here, the Bloch equations of Equation 2.29 through 2.31 were solved numerically using a MATLAB toolbox available online [271]. In Figure 6.4, the excitation profile is shown. Namely, the longitudinal magnetization at the end of the VAPOR sequence normalized by

Pulse Number	Gradient Amplitude (mTm^{-1})	Gradient Direction	Gradient Length (ms)
1	5	z	20
2	5	y	20
3	5	x	20
4	10	z	20
5	10	y	20
6	10	x	20
7	20	z	20

Table 6.2: Shown are the various VAPOR gradient parameters employed in this work.

the initial longitudinal magnetization is plotted against the frequency in Hz. In Figure 6.4A, the excitation profile is shown for a variety of flip angles: 75°, 90°, 105°, and 120°. Here, one can see the B_1 insensitivity of the VAPOR technique since the excitation profile does not drastically change as the flip angle is varied. In Figure 6.4B, the excitation profile is shown for a variety of pulse lengths: 10 ms, 20, ms, and 30 ms. As one would expect, increasing the length of each VAPOR pulse decreases the saturation bandwidth.

The B_1 insensitivity of the VAPOR technique is most effectively demonstrated by Figure 6.5, where the normalized longitudinal magnetization at the center frequency is tracked as a function of time throughout the VAPOR scheme. As can be seen in the figure, regardless of the prescribed flip angle, the longitudinal magnetization is nulled at the end of the VAPOR scheme. Further simulations were performed in order to characterize the dependence of VAPOR's performance on certain sequence parameters, namely pulse length and final delay time, t_7. Figure 6.6 plots normalized residual longitudinal magnetization at the center frequency as a function of flip angle while both pulse length and t_7 are varied. In Figure 6.6A, it is seen that the pulse length has little effect on the resultant magnetization profile and that adequate saturation is achieved over a wide range of prescribed flip angles. In Figure 6.6B, it is seen that modifying t_7, which alters the overall time that the system is subjected to T_1 relaxation, results roughly in a vertical translation of the magnetization profile. The optimal final delay time was found to be 26 ms, as was used in the original VAPOR manuscript [265].

6.2.5 Water Suppression Realization

A VAPOR water suppression scheme, as described in Section 6.2.3, was implemented first into a single voxel spectroscopic sequence and eventually into the localized spectroscopic sequence, described below in Section 6.3. Figure 6.7 illustrates the effect that the VAPOR pulse train has on a representative resultant spectrum. In Figure 6.7A, no water suppression has been applied, and the metabolites of interest are not visible. In Figure 6.7B, VAPOR has been applied, and the water has been suppressed down to the order of magnitude of the metabolites of interest.

The dependence of the VAPOR scheme's efficacy on two of the suppression pulse parameters was investigated and is shown in Figure 6.8. Here, if $a = 4.5$ ppm and $b = 5.0$ ppm the efficacy of the VAPOR scheme was quantified using the suppression factor which is defined here as:

$$H = \frac{\int_a^b S_{\text{No VAPOR}}(\delta)d\delta}{\int_a^b S_{\text{VAPOR}}(\delta)d\delta} \tag{6.9}$$

That is, an integral was performed over a chemical shift range containing the water peak for spectra

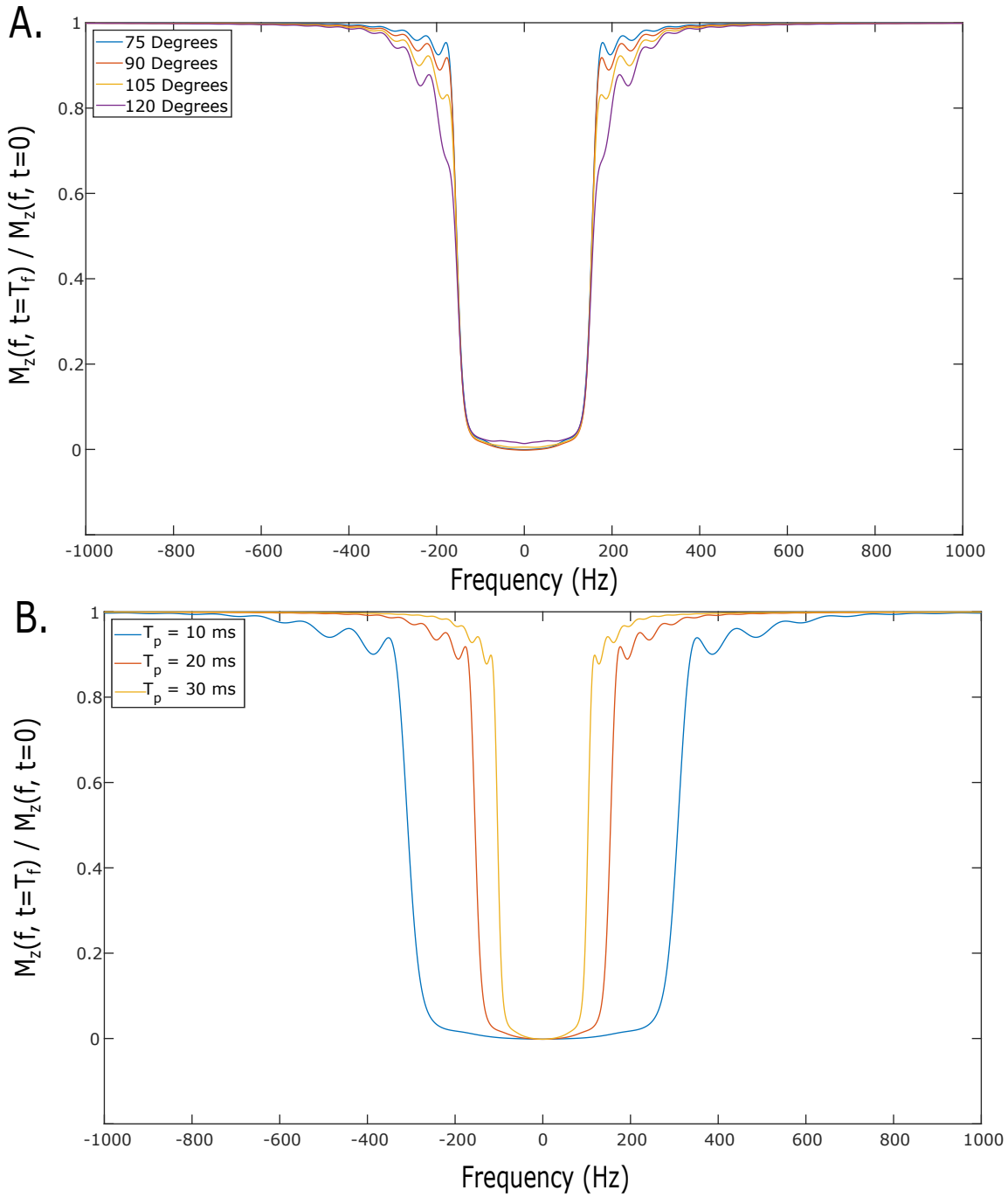

Figure 6.4: Bloch simulated excitation profiles showing the longitudinal magnetization as a function of offset frequency from the water peak - In Figure 6.4A, the relative insensitivity to B_1 inhomogeneities can be seen, as Bloch simulated excitation profiles are shown for a variety of flip angles. In Figure 6.4B, the Bloch simulated excitation profiles are seen to become narrower as the pulse length is increased.

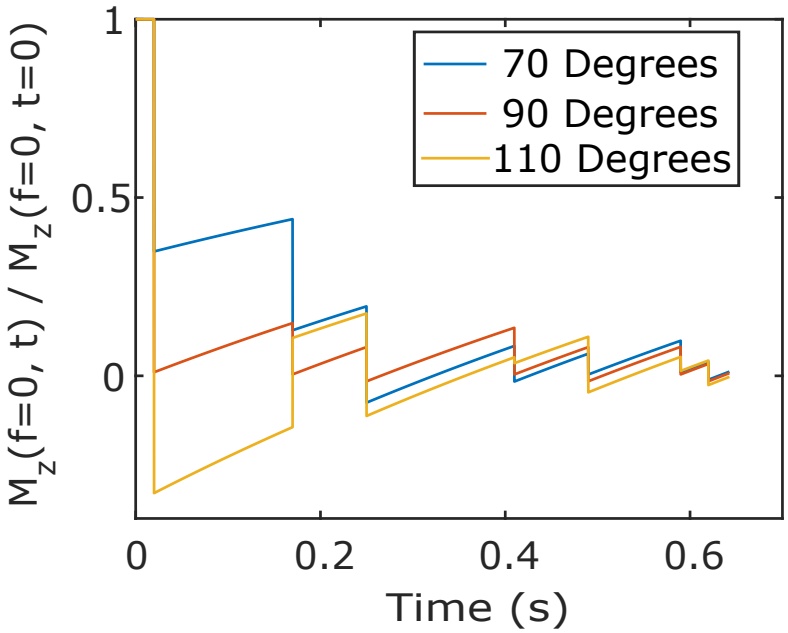

Figure 6.5: The insensitivity of VAPOR to B_1 inhomogeneities as seen by simulating the evolution of the longitudinal magnetization at the water frequency throughout the VAPOR pulse sequence - For each simulated flip angle, the longitudinal magnetization at the water frequency nearly vanishes at the end of the VAPOR pulse sequence.

without and with water suppression, and the ratio was then taken. In Figure 6.8A, the suppression factor is plotted against the pulse length of the VAPOR pulses. It is seen that varying the pulse length has little effect on the overall suppression achieved. In Figure 6.8B, the suppression factor is plotted against the prescribed flip angle. It is seen that adequate suppression was achieved over a prescribed flip angle range from 60° to 140°. Thus, the water suppression scheme is robust in the presence of realistic B_1 inhomogeneities.

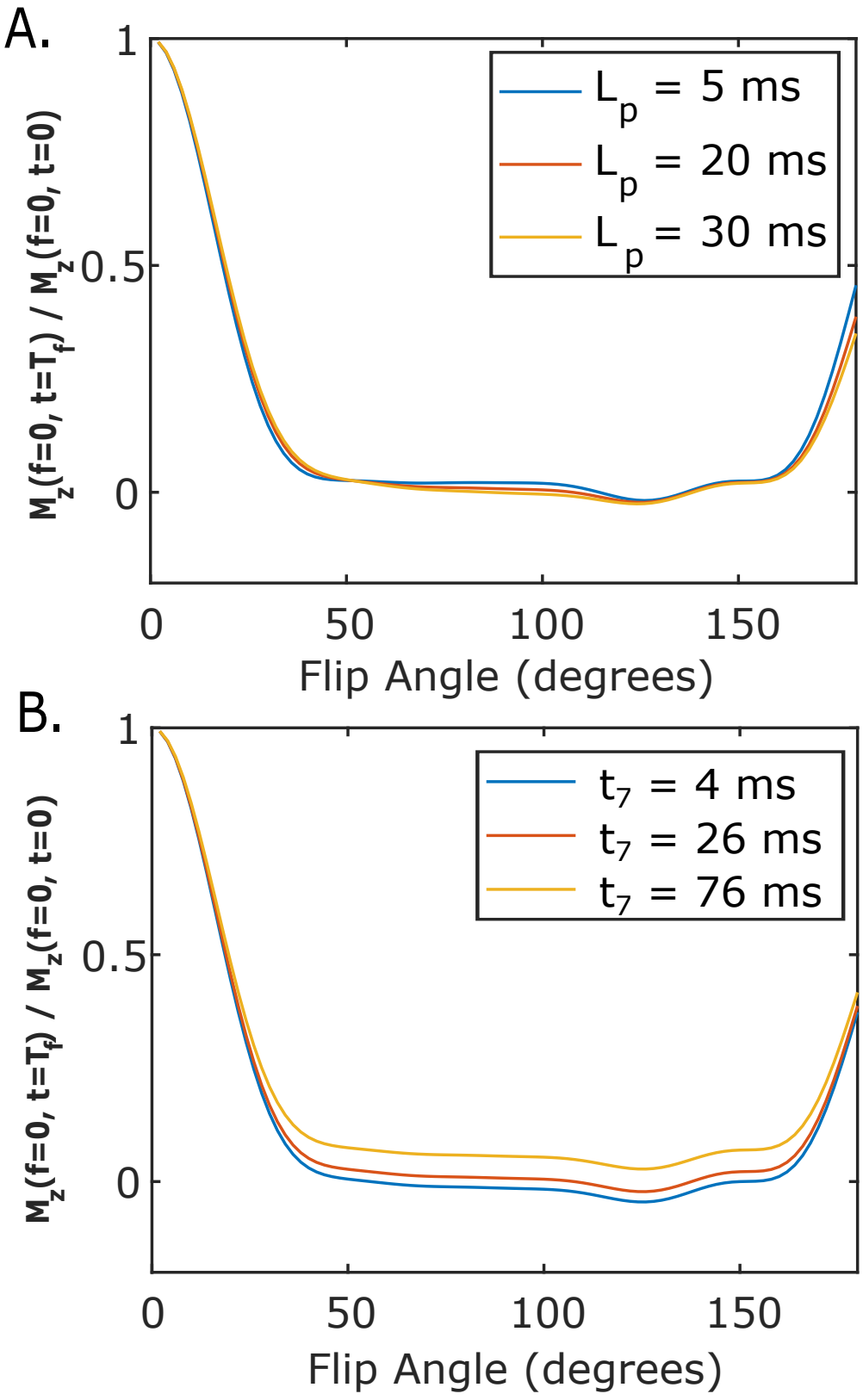

Figure 6.6: The simulated normalized residual longitudinal magnetization at the water frequency plotted as a function of flip angle while both pulse length (6.6A) and final delay time t_7 (6.6B) are varied.

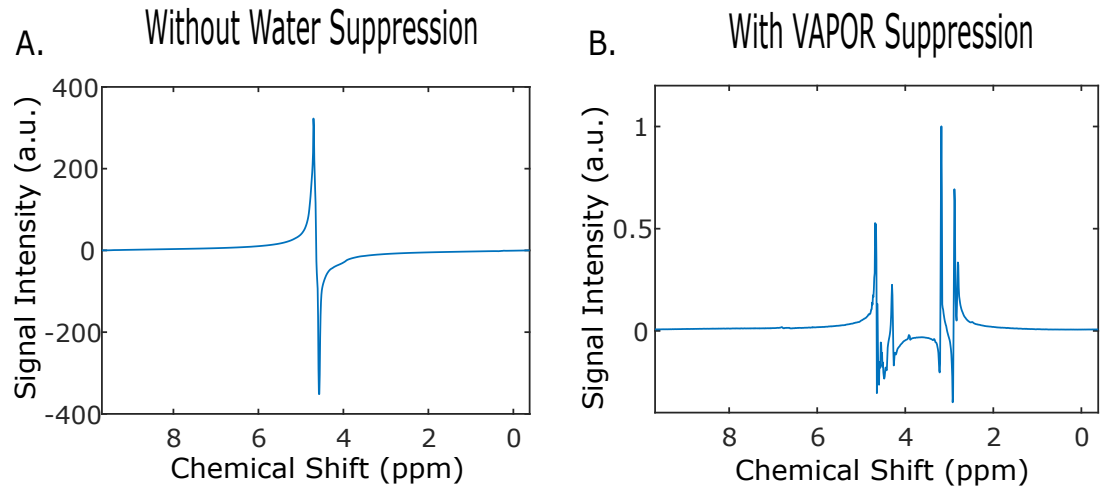

Figure 6.7: A representative spectrum without (6.7A) and with (6.7B) VAPOR water suppression - After water suppression, the intensity of the water peak is on the same order of magnitude as the metabolites of interest.

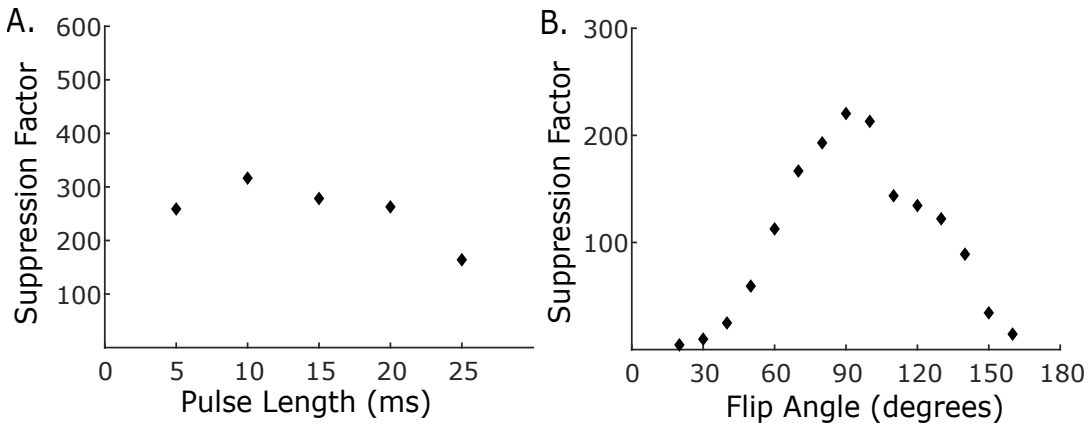

Figure 6.8: The efficacy of water suppression as pulse length (6.8A) and flip angle (6.8B) are varied - In Figure 6.8A, one sees that suppression is rather insensitive to changes in pulse length. In Figure 6.8B, one sees that suppression falls off only when the prescribed flip angle deviates too far from 90°. Adequate suppression was achieved over a prescribed flip angle range from 60° to 140°.

6.3 FID MRSI Pulse Sequence

The pulse sequence applied in this work is the direct acquisition of an FID following excitation [272]. This FID MRSI technique, by construction, utilizes ultrashort echo times. The benefit of using these ultrashort TE sequences at higher field strengths is twofold. Firstly, at higher B_0, T_2 relaxation times decrease. This is due to the fact that microscopic susceptibility differences scale with field strength and are, therefore, more prominent at higher fields. This more rapid transverse relaxation offsets the SNR benefit obtained from transitioning to higher field strength, but an ultrashort TE value minimizes the amount of time that the magnetization has to relax and, thus, maximizes SNR. Secondly, scalar coupling evolution induces signal dephasing which further reduces SNR and increases the overlap of spectral resonances [272]. An ultrashort TE also reduces this scalar coupling evolution effect.

One repetition of the pulse sequence is illustrated in Figure 6.9 which was modified from a figure taken from Korzowski [251]. First the seven-pulse water suppression scheme is applied. Next, an excitation pulse is applied which flips the magnetization into the transverse plane, and the FID is then directly acquired. The application of the gradients was such that data were acquired in a GRAPPA CAIPIRINHA-like pattern, which is discussed in more detail in the following section.

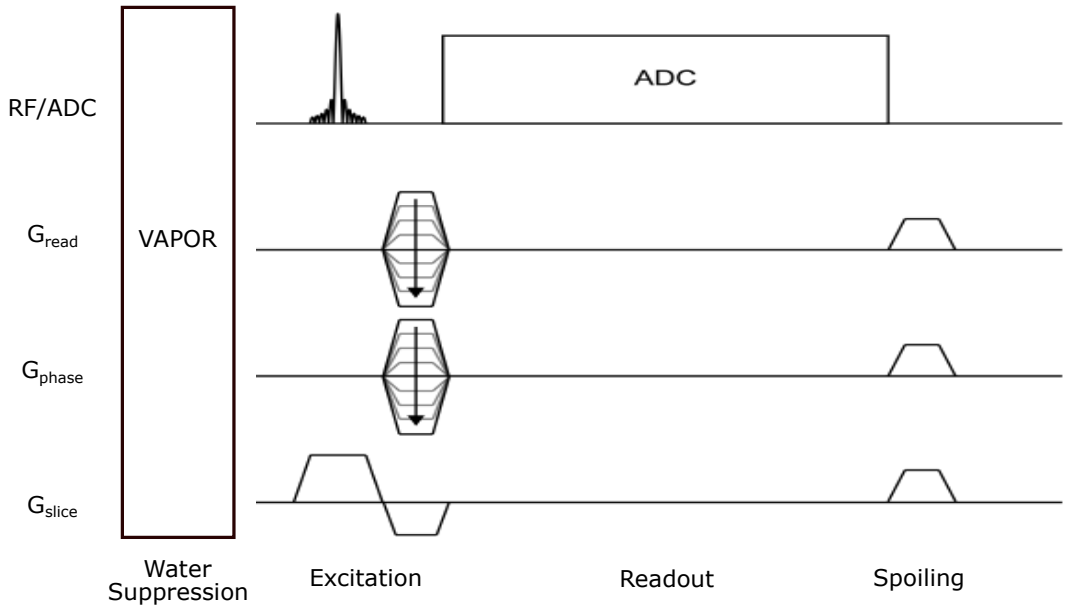

Figure 6.9: The FID MRSI pulse sequence used throughout this work - This figure was modified from reference [251].

6.4 A Novel Temporal Domain GRAPPA Algorithm

The conventional GRAPPA algorithm was described in detail in Sections 5.4 and 5.5. Recall that in this algorithm the GRAPPA weights are determined by having a kernel traverse the ACS region. This ACS region is depicted in Figure 6.10A. The ACS region contains the central rows in the vertical k_y direction but is sampled fully in the horizontal k_x direction. Thus, conventional GRAPPA requires one

of the k-space directions to be fully-sampled which places restrictions on the possible sampling schemes that can be implemented. In MRSI, an FID is acquired at each position in k-space, so there exists a fully-sampled temporal dimension in MRSI data that is not present in MRI data. Several dynamic MRI studies [273, 274, 275, 276, 277, 278, 279, 280, 281, 282, 283, 284, 285, 286, 287, 288, 289] have incorporated temporal domain data in combination with k-space data to determine the coil weights, but no studies exist where the GRAPPA weights are determined exclusively using the time domain data as the fully-sampled ACS dimension.

In the first two decades of the twentieth century, Einstein developed his special [290] and general [291] theories of relativity. The development of relativity revolutionized theoretical physics and led to a number of previously counterintuitive physical implications such as length contraction, time dilation, the constancy of the speed of light, the equivalence of mass and energy, the gravitational redshift, and the gravitational deflection of light. Whereas prior to Einstein's work it was thought that time and space were separate entities that are independent of each other, it is now understood that they are fundamentally intertwined and influence each other as described by the Lorentz transformation [292, 293, 294]. It was this understanding of the fundamental equivalence of time and space that motivated the main hypothesis of this dissertation: that GRAPPA can be applied to accelerate MRSI using only the time domain data to calculate the coil weights.

To understand the concept of ARTT GRAPPA, consider Figure 6.10. Figure 6.10A depicts a conventional GRAPPA sampling pattern. Here, the coil weights are calculated by having the kernel traverse an ACS region that extends fully in the k_x direction. For a given unsampled k_y, each k_x point in that row is reconstructed. Figure 6.10B illustrates the ARTT GRAPPA concept, where the k_x direction has been replaced by the temporal dimension. Thus, the kernel traverses an ACS region which is some number of vertically stacked FIDs, and the coil weights are calculated using an ACS region in k-t-space. For a given unsampled k_y, an entire FID is reconstructed. To additionally reconstruct along the k_x direction, a higher dimensional GRAPPA implementation is needed. This can be accomplished either by manually augmenting the dimensionality of the GRAPPA reconstruction algorithm by brute force or by the GRAPPA operator approach [295], but the literature indicates that the GRAPPA operator approach is the more accurate technique [296]. Here, GRAPPA is extended into the third dimension by repeatedly applying a series of 2D GRAPPA reconstructions for each k-t slice along one undersampled k-space dimension then applying another series of 2D GRAPPA reconstructions for each k-t slice along the other undersampled k-space dimension.

By calculating the GRAPPA weights using only time domain data one can now simultaneously undersample along multiple dimensions in k-space which greatly increases the number of possible sampling patterns. To visualize the possible sampling schemes in a multidimensional setting consider a simple experiment with two phase encoding directions. This is illustrated in Figure 6.11 which is an amalgamation of numerous figures taken from Breuer et al [297]. In particular, Figure 6.11A depicts the case when k-space is fully-sampled. If one wants to achieve an effective acceleration factor of two, then there are three possible ways it can be achieved. One can apply two-fold acceleration along the vertical k-space direction while keeping the spacing in the horizontal k-space direction fixed, as shown in Figure 6.11B. Alternatively, one can apply two-fold acceleration along the horizontal k-space direction while keeping the spacing in the vertical k-space direction fixed, as shown in Figure 6.11C. The third possible sampling pattern is a checkerboard-like pattern that combines the first two methods, as

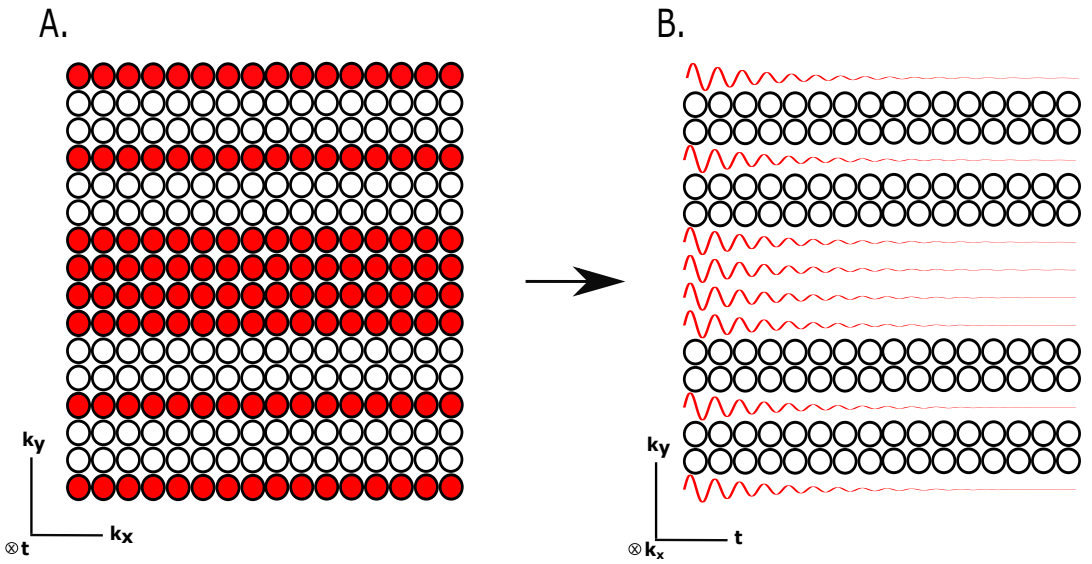

Figure 6.10: The difference between conventional MRSI GRAPPA (6.10A) and ARTT GRAPPA (6.10B) - In the conventional approach the reconstruction is performed in k-space and iteratively repeated for each timepoint in the FID. In the approach applied in this work, the reconstruction is instead performed in k-t-space, and the GRAPPA operator method is used to reconstruct along the additional k-space dimension.

shown in Figure 6.11D. Aliasing necessarily results from undersampling and occurs in the undersampled direction. Thus, the resulting image obtained from reconstructing the data shown in Figure 6.11B and 6.11C will result in aliasing along the vertical and horizontal image dimensions, respectively. By dividing the undersampling along both eligible k-space dimensions, the resulting image obtained from reconstructing the data shown in Figure 6.11D will exhibit an altered aliasing signature relative to 6.11B and 6.11C.

This is the underlying logic behind the controlled aliasing in parallel imaging results in higher acceleration (CAIPIRINHA) [298] concept which aims to modify the appearance of aliasing effects in order to reduce the dependence of the parallel imaging implementation on the geometry of the phased array. CAIPIRINHA has been applied to minimize aliasing artifacts in a variety of applications [299, 300, 301]. As the effective acceleration increases the number of possible sampling patterns increases factorially leading to high levels of flexibility when choosing potential sampling schemes. This is illustrated in Figure 6.12 which was taken from Breuer et al [297]. Here, one considers all four by four subsets of k-space which achieve an effective acceleration factor of four. Conventional sampling patterns utilizing acceleration schemes of one by four, two by two, and four by one are shown, respectively, in the left part of this figure. Additionally, four CAIPIRINHA-like patterns are constructed by systematically circularly shifting subsequent rows of data rightward by some integral distance Δ, as illustrated in the right part of the figure. By sampling data in these CAIPIRINHA-like patterns, one is able to more readily control aliasing artifacts and minimize the effect that aliasing has on the resultant image.

The workflow for the ARTT GRAPPA reconstruction algorithm is illustrated in Figure 6.13 for the

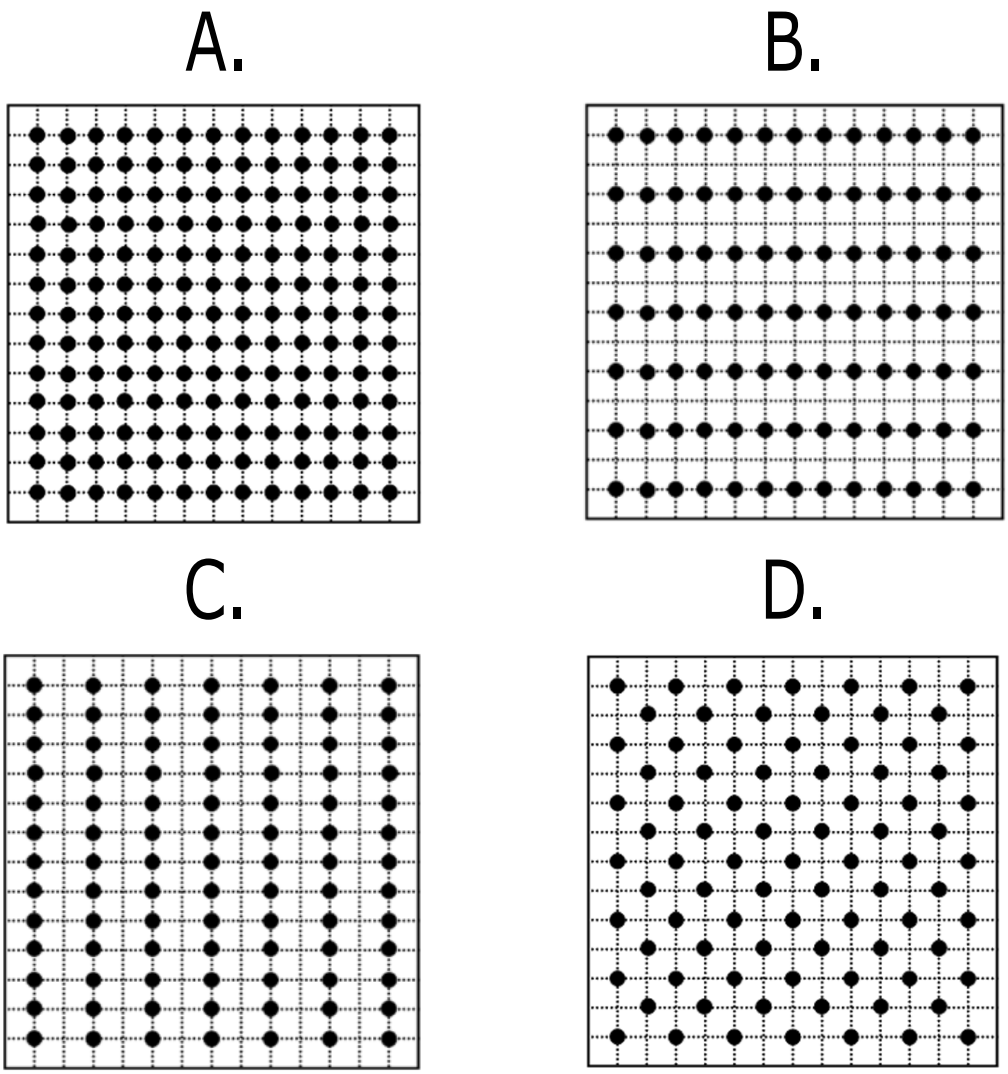

Figure 6.11: Various two-fold undersampled k-space sampling schemes - In Figure 6.11A, k-space is fully-sampled. In Figure 6.11B and 6.11C, two-fold undersampling is applied along vertical and horizontal dimensions, respectively. Figure 6.11D shows the third possibility, a checkerboard-like pattern that combines both vertical and horizontal and undersampling. This figure was modified from reference [297].

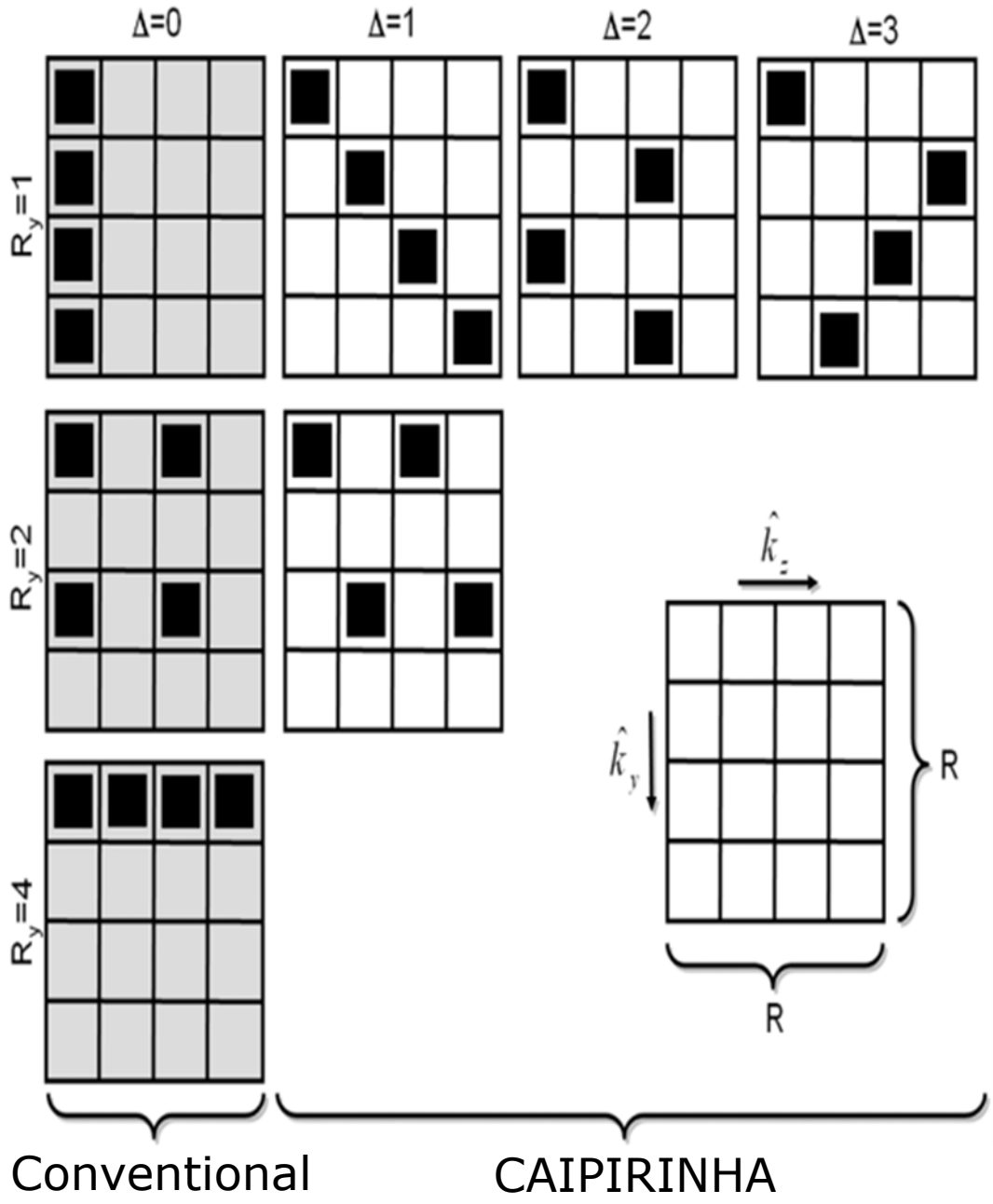

Figure 6.12: The difference between conventional undersampling schemes and CAIPIRINHA-like schemes - This figure was modified from reference [297].

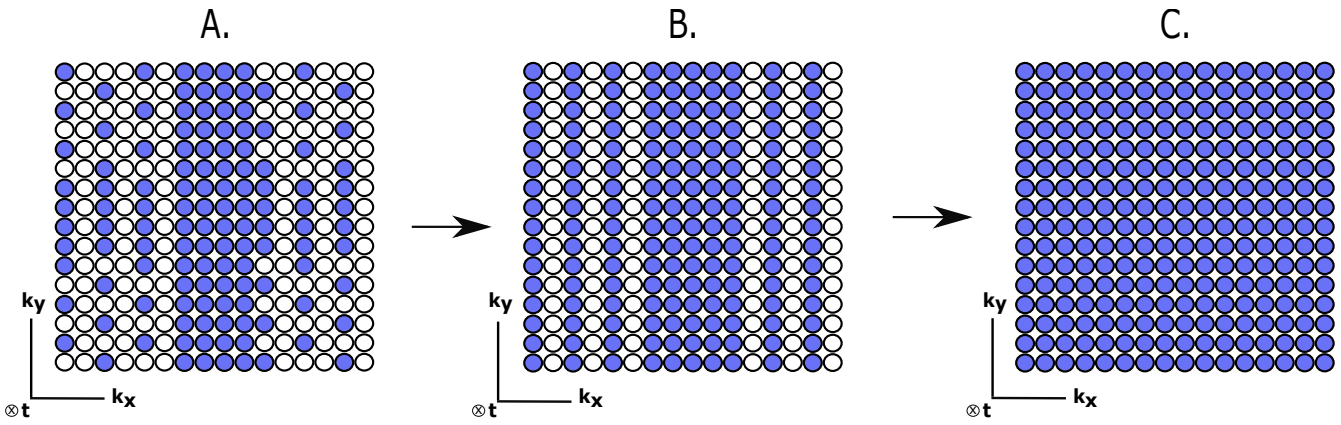

Figure 6.13: The workflow of the GRAPPA Operator approach - Each partially sampled column in the undersampled dataset (6.13A) is reconstructed. Then each underampled row from the intermediate dataset (6.13B) is reconstructed until the fully-reconstructed dataset (6.13C) is recovered.

case of a two dimensional MRSI experiment. First, the data are sparsely sampled in a CAIPIRINHA-like GRAPPA sampling scheme, as shown in Figure 6.13A. Here, the figure depicts k-space, but since it is an MRSI experiment, each blue circle represents a complete FID going into the plane of the paper, as indicated by the axes in the figure. In this example, the undersampled regions utilize two by two acceleration with a four by four ACS region, and there is a $\Delta = 1$ CAIPIRINHA shift in the vertical direction. The first step in the algorithm is to reconstruct the left column. Observing that the k_y-t plane in Figure 6.13A resembles the k_y-t plane in Figure 6.10B, one can apply the ARTT GRAPPA method described above to reconstruct this column. This procedure is then repeated until each undersampled column has been reconstructed, as shown in Figure 6.13B. Next the rows are reconstructed by applying the ARTT GRAPPA method to each k_x-t plane and iterating over each k_y position until the entirety of k-space has been reconstructed, as shown in Figure 6.13C. Alternatively, when the CAIPIRINHA shift is in the horizontal direction, one first reconstructs the rows and then reconstructs the columns. In a three dimensional MRSI experiment, this procedure is then iterated for each partition encoding k-space slice until the entire dataset has been reconstructed.

The effective acceleration factor R_{eff} is the parameter of importance, as it represents the factor by which the image acquisition would be accelerated. It is defined as

$$R_{\text{eff}} = \frac{N_k}{N_x N_y} \tag{6.10}$$

where $N_x = N_y = 64$ specifies the matrix size in each direction, and N_k is the total number of FID's acquired or, in the case of artificial undersampling, retained.

6.5 Coil Combination Algorithm

After the missing data points have been reconstructed, the FIDs from each individual coil element need be combined to obtain a resultant FID in a given voxel. At this point the data array is five-dimensional: three spatial dimensions, a temporal dimension, and a coil dimension. The coil dimension must be

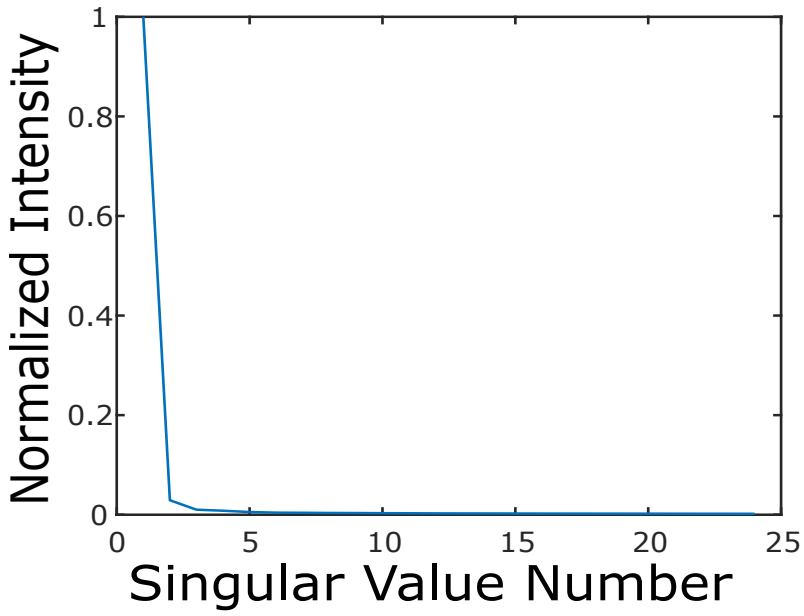

Figure 6.14: Normalized intensity plotted against singular value - The intensity falls off rapidly as the singular value number increases.

collapsed so that the conventional four-dimensional MRSI data format can be recovered. Coil combination is often accomplished using a sum-of-squares based approach [302], but this reduces the SNR of the combined FID and, hence, its corresponding spectrum. Singular value decomposition (SVD) is a mathematical technique that can be thought of as a generalized version of eigenvalue decomposition in the case of non-square matrices. The singular values can be divided into those originating from signal and those arising from noise [303], and the SNR can be increased by discarding the contributions from singular vectors corresponding to the singular values arising from noise. This is illustrated in Figure 6.14 where normalized signal intensity is plotted against singular value in a representative single-voxel spectroscopy experiment. In this figure, there are twenty-four singular values since the data were acquired using a twenty-four channel head coil. One can see a large intensity for the first singular value which corresponds to authentic signal in the data. After that first value, the intensity of the subsequent singular values falls off rapidly, indicating that they increasingly arise from noise in the data. Thus, this method allows one to find the optimal rank-1 solution for the N individual signals.

In order to illustrate how this approach works, consider first a single-voxel spectroscopy experiment for simplicity. Here, FIDs consisting of N time points have been acquired by each of the m individual receiver coils in the phased array. The m individual FIDs, $\{y_i(t)\}$, need be combined into a resultant signal of interest, $\phi(t)$. This situation can be modeled mathematically via the following relation:

$$y_i(t) = \beta_i \phi(t) + \lambda_i(t) \tag{6.11}$$

for $t = 1, \ldots, N$ and $i = 1, \ldots, m$. Here, $\{y_i(t)\}$ are the observed signals from the m coil elements, β_i are the unknown sensitivities of the m coil elements, $\{\lambda_i(t)\}$ are the noise profiles from each of the m coil elements, and $\phi(t)$ is the signal of interest [304].

There are numerous techniques with which to find $\phi(t)$. Initially, a parametric approach was implemented in which the signal, $\phi(t)$, was modeled as a sum of exponentially damped sinusoids [305]. The data were then arranged as a Hankel matrix, which is a square matrix whose skew diagonal entries are constant. The complex amplitudes, damping coefficients, and frequencies of each mode were then determined via SVD and subsequently finding the eigenvalues of the solution to a least squares regression problem. This parametric approach had two main drawbacks. The first drawback was that it was too computationally intensive, typically taking on the order of tens of seconds to compute. In a single voxel setting, this would be acceptable, but such a computational burden is not optimal in a multi-voxel setting where the coil combination algorithm need be applied thousands of times, once for each voxel in the image. The second drawback is that one must know a priori the number of modes with which to model the signal. The number of modes should equal the number of resonances in a given spectrum. However, this value is not generally known prior to the experiment nor is it generally fixed from voxel to voxel in an MRSI experiment. Thus, it was determined to instead use a simpler, non-parametric approach that is more robust in settings where the number of metabolites in a given voxel is variable.

In order to determine $\phi(t)$, one first recasts Equation 6.11 into a matrix equation as shown:

$$\mathbf{Y} = \beta\phi^* + \mathbf{\Lambda} \tag{6.12}$$

Here, $\mathbf{Y}$ is an m by N matrix with the component Y_{ij} specifying the observed signal detected by the ith coil at the jth time point. Analogously, $\mathbf{\Lambda}$ is an m by N matrix with the component Λ_{ij} specifying the noise profile of the ith coil at the jth time point. β is a column vector of length m specifying the sensitivity of each coil element, and ϕ^* is a row vector of length N that is the conjugate transpose of the signal of interest. In spectra with a sufficiently high SNR, $\mathbf{\Lambda}$ can be neglected, and Y can be approximated by the rank-one matrix $\beta\phi^*$ [304]. One can decompose Y using SVD:

$$\mathbf{Y} = \mathbf{U}\mathbf{\Sigma}\mathbf{V}^* \tag{6.13}$$

Here, $\mathbf{U}$ and $\mathbf{V}$ are unitary matrices of dimensions m and N, respectively, $\mathbf{\Sigma}$ is a diagonal matrix of dimension m by N, and $\mathbf{V}^*$ denotes the conjugate transpose of the matrix $\mathbf{V}$. A schematic illustrating the dimensionality of the SVD is shown in Figure 6.15. The diagonal entries of $\mathbf{\Sigma}$ are termed the singular values, which are listed in descending order. These singular values are analogous to the eigenvalues determined in eigenvalue decomposition.

Letting σ_1 denote the maximum singular value and letting u and v be the left and right singular vectors, respectively, one can estimate the coil sensitivities β_i and the desired signal $\phi(t)$ as follows [304]:

$$\beta_i = u_i \tag{6.14}$$

$$\phi(t) = \sigma_1 v(t) \tag{6.15}$$

The described algorithm applies to single-voxel, multi-channel datasets. This technique can then be extended to multi-voxel, multi-channel datasets via the successive application of the algorithm in each voxel in the image. Figure 6.16 illustrates a non-water suppressed image of a healthy volunteer's brain

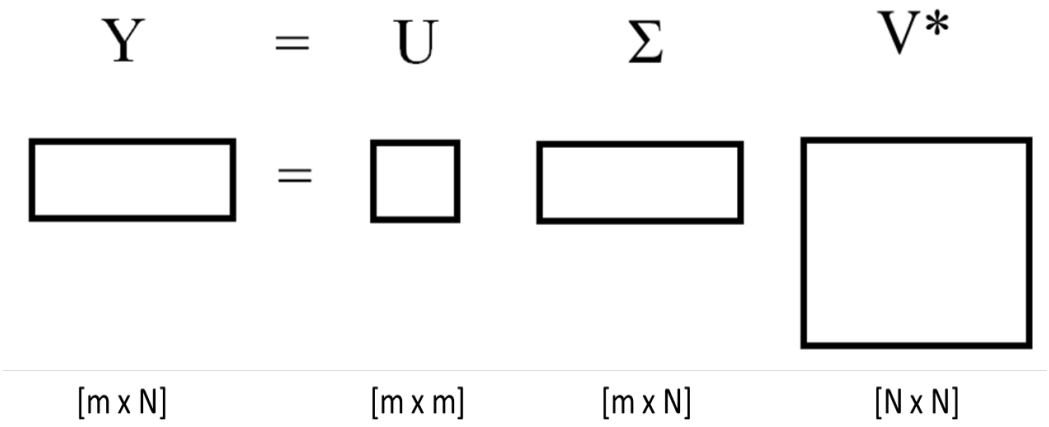

Figure 6.15: A schematic illustrating the relevant dimensions of the singular value decomposition performed in the coil combination algorithm.

for which the multi-voxel version of this algorithm has been applied.

It should be noted that the order in which one performs this coil combination and the 3D Fourier transformation is important. The model described in Equations 6.11 and 6.12 operates in the spatial domain. If both the Fourier transformation and the SVD were linear functions, then it would not matter in which domain the algorithm was performed, but either function being nonlinear would necessitate that the algorithm be performed in image space. The Fourier transformation is a linear function, but the SVD is not. If one defines the function

$$\mathcal{F} : \mathbb{C}^{m \times N} \mapsto \mathbb{C}^{N} \tag{6.16}$$

such that $\mathcal{F}$ maps a matrix Y to a signal $\phi(t)$ using the method described above, it can be seen that the linearity requirement

$$\mathcal{F}(\alpha Y_1 + \beta Y_2) = \alpha \mathcal{F}(Y_1) + \beta \mathcal{F}(Y_2) \tag{6.17}$$

does not hold $\forall\ \alpha, \beta \in \mathbb{C}$ and $\forall\ Y_1, Y_2 \in \mathbb{C}^{m \times N}$. In particular, the 3D Fourier transformation must first be applied followed by the SVD. Thus, the coil combination need be performed in image space. Figure 6.17 illustrates in non-water suppressed phantom images artifacts that will arise if the coil combination is mistakenly applied in k-space. In particular, the same dataset has been combined in both k-space (6.17A) and image space (6.17B).

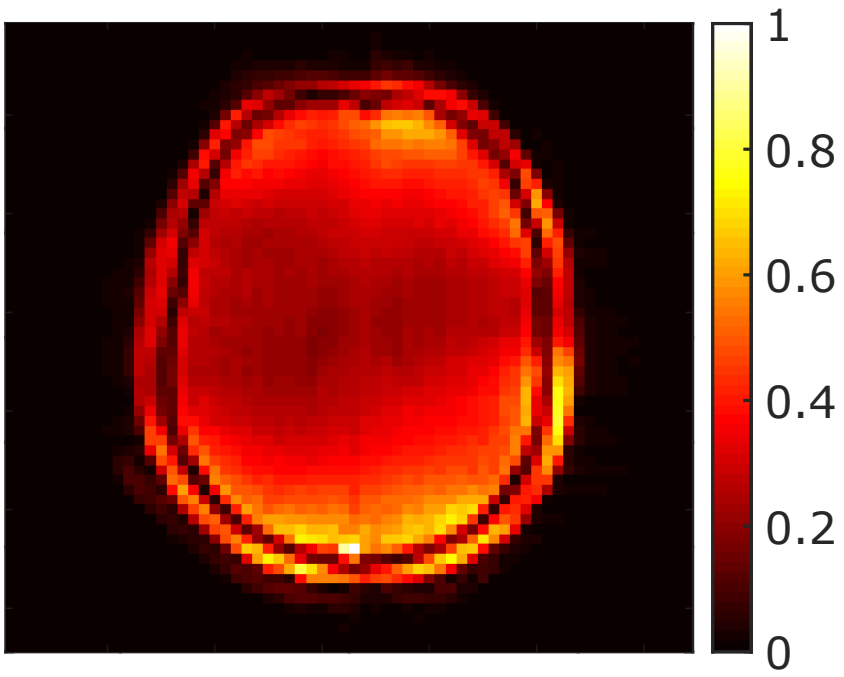

Figure 6.16: A non-water suppressed image of a healthy volunteer's brain for which the multi-voxel version of this algorithm has been applied.

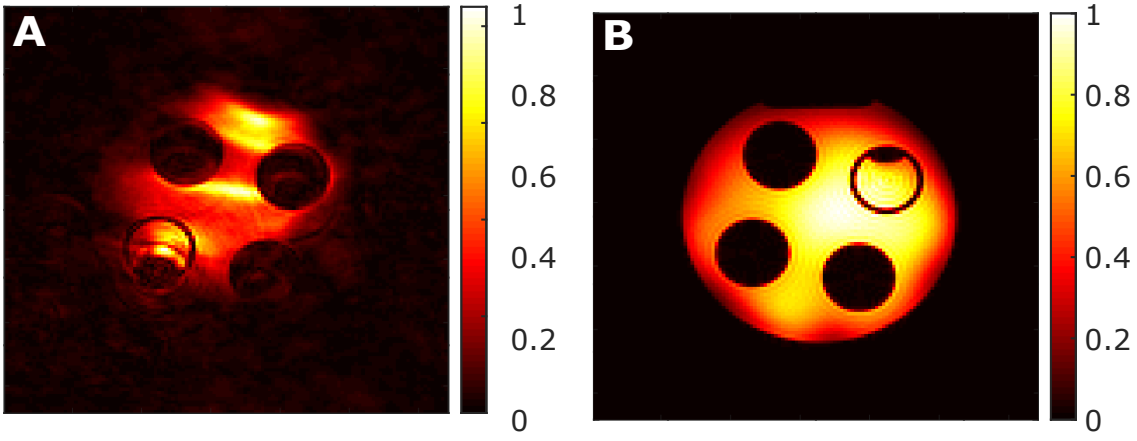

Figure 6.17: A non-water suppressed phantom image for which the coil combination was performed in k-space (6.17A) and image space (6.1B). One sees that the coil combination need be applied in image space.

6.6 Lipid Suppression

A further challenge in proton spectroscopy is the subcutaneous layer of fat surrounding the skull. These pericranial lipids produce a number of strong resonances, the most prominent of which occurs around 1.5 ppm, which tend to be quite broad. The point spread function (PSF), which describes the response of an imaging system to a point source or point object, is nonideal in MRSI due to the limited number of acquired phase encoding increments [61]. Because the lipid resonance is so large, the side lobes of the PSF cause the lipid signal originating outside of the skull to bleed into nearby voxels [306] which contaminates spectra otherwise containing only brain tissue. The extent of this problem is illustrated in Figure 6.18. In particular, Figure 6.18A shows an *in vivo* brain tissue spectrum with characteristic lipid contamination. A very large lipid resonance is found extending approximately between 1 and 2 ppm. In Figure 6.18B, an NAA metabolite map of a non-lipid suppressed dataset is shown. Despite NAA appearing at 2.01 ppm, on the border of this lipid contaminated spectral region, only voxels in the peripheral ring of the skull appear with appreciable relative NAA concentrations. The concentrations depicted in Figure 6.18B are displayed in arbitrary units, as this figure aims to give only a qualitative description of the problem. Lipid suppression is usually accomplished prior to or during data acquisition using relaxation-based methods [307] or outer volume suppression [308]. However, in order to avoid both unnecessarily increasing the specific absorption rate (SAR) and extending the minimum achievable TR by suppressing the lipid signal during image acquisition, an algorithm that suppresses the lipid signal after data acquisition was highly desirable.

This work utilized a lipid suppression algorithm based off L_2 regularization [309]. Regularization is the act of incorporating prior knowledge to solve ill-posed problems, and L_2 refers to the fact that a quadratic loss function is used [310]. This process is alternatively commonly referred to as Tikhonov regularization [311] or ridge regression [312] in the literature. The benefits of L_2 regularization is that the regularization process admits a closed-form solution that can be easily computed.

The first step of the algorithm utilizes dual density reconstruction which uses two datasets with different resolutions [313]. The high resolution dataset allows for the generation of a lipid image, and the low resolution dataset has a sufficiently high SNR for metabolite signal quantification [309]. First a dual density k-space dataset is obtained via the following relation:

$$\mathbf{dual} = \mathcal{F}^{-1}(\mathcal{F}(\mathbf{lipid}) + \mathcal{F}(\mathbf{csi}_{low})) \tag{6.18}$$

Here, $\mathcal{F}$ and $\mathcal{F}^{-1}$ represent the Fourier transformation and its inverse, respectively, $\mathbf{csi}_{low}$ is the low resolution dataset, and

$$\mathbf{lipid} = \mathbf{M}_{lipid}\mathbf{csi}_{high} \tag{6.19}$$

where $\mathbf{csi}_{high}$ is the high resolution dataset and $\mathbf{M}_{lipid}$ is a binary mask that selects only the ring surrounding the skull [309]. Lipid-basis penalty solves an optimization problem forcing the lipid and metabolite spectra to be mutually orthogonal [314]. Where the lipid-basis penalty method considers the sum of the absolute value of the inner products between the lipid and metabolite spectra, this L_2 regularization instead performs the summation in quadrature as follows:

$$\min ||\mathbf{x} - \mathbf{dual}||_2^2 + \beta \sum_{i \in \mathbf{M}_{brain}} ||\mathbf{L}^* \mathbf{x}_i||_2^2 \tag{6.20}$$

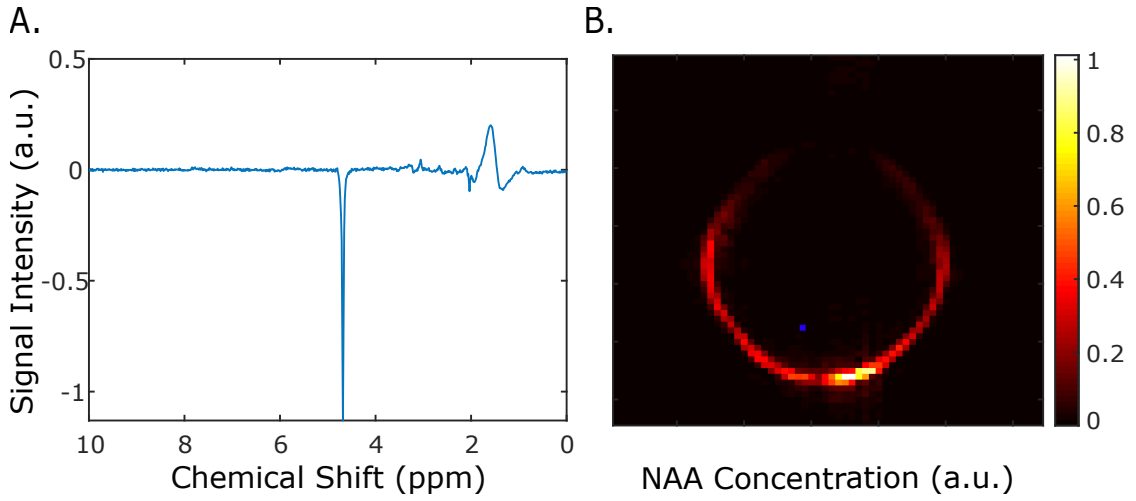

Figure 6.18: An illustration of the need for lipid suppression - Figure 6.18A shows an *in vivo* brain tissue spectrum with representative lipid contamination. A very large lipid resonance is found approximately between 1 and 2 ppm. In Figure 6.18B, an NAA metabolite map of a non-lipid suppressed dataset is shown. Only voxels in the peripheral ring of the skull appreciably appear in the metabolite map. The blue pixel seen in Figure 6.18B specifies the position of the spectrum shown in Figure 6.18A.

Here $\mathbf{M}_{brain}$ is a binary mask that selects only brain tissue, $\mathbf{x}_i$ is the desired spectrum in the ith voxel, $\beta = 0.65$ is a regularization parameter, $\mathbf{L}$ is the lipid-basis matrix, and * denotes the conjugate transpose. $\mathbf{L}$ is generated by taking the spectra from the dual-density image inside the lipid mask [309]. The solution can then be computed in closed-form. Namely, if i is an element of $\mathbf{M}_{brain}$, then

$$\mathbf{x}_i = (\mathbf{I} + \beta \mathbf{L}\mathbf{L}^*)^{-1}\mathbf{dual}_i \tag{6.21}$$

Otherwise,

$$\mathbf{x}_i = \mathbf{dual}_i \tag{6.22}$$

In this work, the lipid and brain masks are determined in a semi-automated fashion, and this L_2 regularization algorithm is applied to the dataset following both GRAPPA reconstruction and coil combination. The effect of this algorithm is shown in Figure 6.19 which shows the same spectrum, both before and after lipid suppression. In Figure 6.19A, a large lipid signal is observed extending approximately between 1 and 2 ppm. In Figure 6.19B, the large signal is completely removed, although other features of the spectrum remain unchanged.

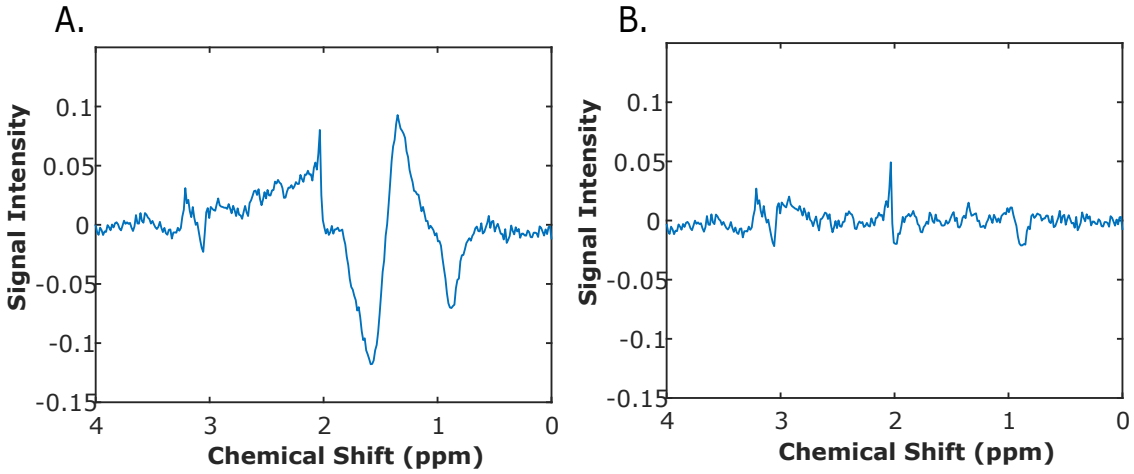

Figure 6.19: A non-lipid supressed spectrum (6.19A) and the same spectrum following lipid suppression via L_2 regularization (6.20B).

6.7 Metabolite Quantification

LCModel (LCModel Inc., Oakville, Canada) [315] is the most commonly employed algorithm to quantify proton spectra. It models a spectrum as a linear combination of a number of basis spectra, where each basis element is an *in vitro* spectrum acquired in a region containing only a single metabolite using the same pulse sequence, the same echo time and on a scanner of the same field strength. The basis set should include all metabolites, lipid resonances, and macromolecular peaks that may appear in the *in vivo* dataset that is to be quantified. These basis spectra can either be directly acquired or simulated [316]. In this work, simulated basis spectra provided by LCModel were used. LCModel is fully automated and can be used to quantify multi-voxel datasets [317].

After the basis sets are determined, either via simulation or direct measurement, the first step in the LCModel algorithm is to zero fill both the *in vivo* dataset and the *in vitro* basis sets in order to double the spectral resolution. Next, the modeled spectrum $Y(\nu_k)$ is calculated using the following equation:

$$Y(\nu_k) = e^{-i(\phi_0+\nu_k\phi_1)}\left[\sum_{j=1}^{N_B}\beta_j B_j(\nu_k) + \sum_{l=1}^{N_m} C_l \sum_{n=-N_s}^{N_s} S_n M_l(\nu_{k-n}, \gamma_l, \epsilon_l)\right] \tag{6.23}$$

where

$$M_l(\nu, \gamma_l, \epsilon_l) = \mathcal{F}\{m_l(t)e^{-(\gamma_l+i\epsilon_l)t}\} \tag{6.24}$$

Here, ν_k is the set of all spectral points. The zeroth-phase correction is given by ϕ_0 and is needed due to the gross misadjustment of the phase of the detector. The first order phase correction is given by ϕ_1 and is needed due to the time delay between excitation and detection, flip angle variations across the spectrum, and phase shifts induced by the filter that is applied to reduce noise outside the spectral bandwidth. $\sum \beta_j B_j$ is a frequency domain baseline correction where the baseline is modeled as N_B cubic B-splines. The concentrations of interest of the N_m metabolites in the spectrum are given by C_l. S_n are the line shape coefficients, and $\sum S_n M_l$ is a finite discrete convolution from $-N_s$ to N_s to account for static field inhomogenieties, eddy currents, and other distortions. Moreover, γ_l modifies

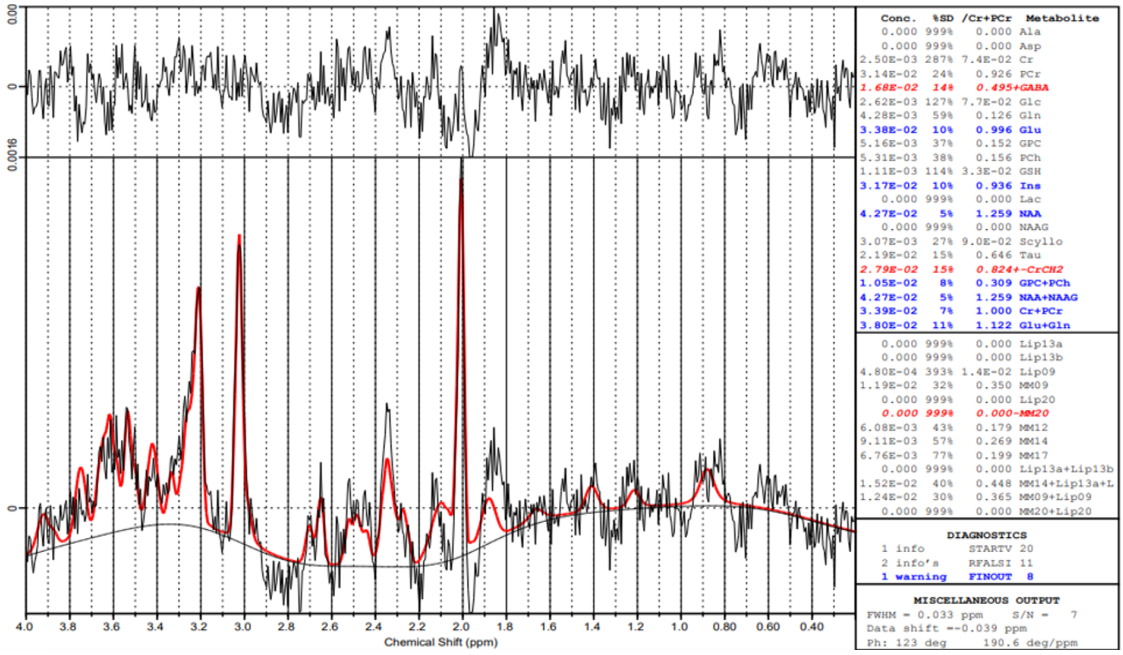

Figure 6.20: A typical LCModel output file.

the basis spectra to account for the shortening of T_2 *in vivo* [318], and ϵ_l modifies the basis spectra to account for referencing errors. Lastly, $m_l(t)$ is inverse fast Fourier transformation of the model spectrum, and $\mathcal{F}$ is the corresponding fast Fourier transformation into the spectral domain [315]. The algorithm then applies a constrained, Marquardt-modified Gauss Newton least-squares analysis [319] to solve for the $3N_m+2N_s+N_B+3$ unknowns: the concentrations, T_2 shortening terms, and referencing terms of N_m metabolites in the spectrum, the N_B baseline coefficients, the $2N_s+1$ line shape terms, and the two phase correction parameters. It should be noted that the number of metabolites N_m is specified by the user in the input of the basis set, while N_B and N_s are calculated by the algorithm by the linewidth of the spectrum. LCModel is then applied iteratively to quantify multi-voxel datasets.

Figure 6.20 illustrates the typical output of LCModel. On the left of the figure, the actual spectrum is shown in black, while the fit is shown in red. For each resonance in the basis set the concentration and relative concentration normalized by the total creatine amplitude is provided. As a measure of the variance the Cramér–Rao lower bound (CRLB) [320, 321] is also provided for each resonance in the basis.

6.8 Experimental Techniques

6.8.1 Simulation Experimental Setup

A digital phantom was constructed for initial simulation studies. The digital phantom contained four circular test tubes arranged in a square-like pattern. Each test tube possessed a different simulated spectral signature: creatine, creatine and choline, creatine and NAA, and creatine and lactate. The simulated coil sensitivity profile varied circularly in the in-plane direction and parabolically along the longitudinal axis. With the exception of the acceleration factor, none of the other parameters should

exhibit a dependence on the orientation of the reconstruction, so these initial simulations utilized a conventional MRSI GRAPPA implementation. Each parameter was successively varied in order to characterize the reconstruction accuracy's dependence on that parameter. Reconstruction accuracy was quantified by taking the mean squared error (MSE) of the entire dataset. In particular, if X_i are the observed values, $\hat{X}_i$ are the predicted values, and N is the number of data points in both datasets, then the MSE can be computed via the following equation:

$$MSE = \frac{1}{N}\sum_{i=1}^{N}(\hat{X}_i - X_i)^2 \tag{6.25}$$

Here, $i \in \{1, 2, ..., N\}$ is the index which, in this case, runs over both spatial dimensions, the temporal dimension, and the coil dimension. While varying a given parameter, the largest MSE was assigned a value of unity and all other MSE values were normalized by that value. The varied parameters were the acceleration factor R, the number of acquired autocalibration lines N_{ACS}, the kernel dimension in the fully-sampled direction K_x, and the distance S between consecutive kernel positions as it traverses the autocalibration region.

6.8.2 Retrospectively Undersampled Phantom Experimental Setup

Next phantom studies were performed using an in-house built phantom which was a cooler filled with water. Inside the cooler, four 60-mL test tubes were inserted and fixed in place. The test tubes contained a combination of choline, creatine, NAA, and lactate, the concentrations of which are summarized in Table 6.3. A photograph of the phantom showing the layout of the test tubes prior to being filled with water is shown in Figure 6.21A. A schematic depicting the contents of the four test tubes in the phantom is shown in Figure 6.21B.

Tube Number	Creatine (mM)	Choline (mM)	NAA (mM)	Lactate (mM)
1	50	0	0	0
2	50	100	0	0
3	0	0	100	0
4	50	0	0	100

Table 6.3: The molar concentrations of the four metabolites in each test tube of the phantom.

A fully-sampled, two-dimensional dataset was acquired. The matrix size was 64×64, and the slice thickness was 15 mm. The FOV was 240×240 mm^2, yielding an in-plane resolution of 3.75 mm. A TR of 920 ms was used so that the entire fully-sampled measurement took 62 minutes. The fully-sampled data was then retrospectively undersampled using seven ARTT GRAPPA sampling patterns varying from an effective acceleration of 2.50 to 4.71. The specifics of each undersampling pattern are illustrated in Table 6.4. In this table, the number of ACS lines (N_{ACS}) in both x and y, the acceleration factor (R) in both x and y, and the effective acceleration factor are listed.

Each of the seven retrospectively undersampled datasets was reconstructed using the ARTT GRAPPA approach described in Section 6.4. The fully-sampled dataset and each reconstructed dataset were quantified using LCModel to produce metabolite maps of the four metabolites in the phantom.

The error of the GRAPPA reconstruction was then measured as a function of effective acceleration

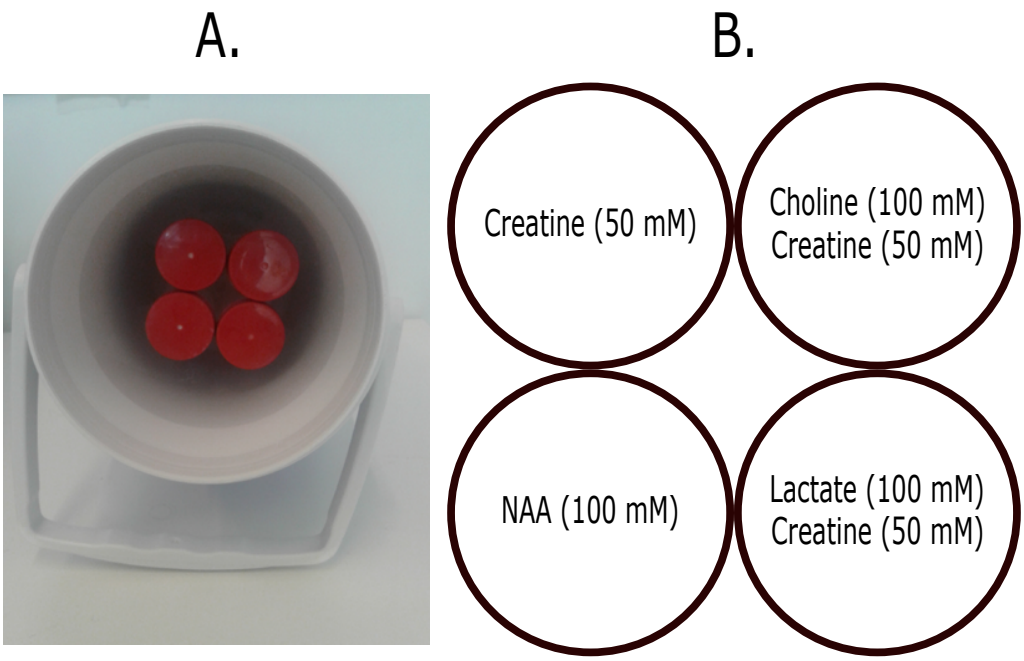

Figure 6.21: The phantom used in the retrospectively undersampled phantom analysis - Figure 6.21A is a photograph of the phantom prior to being filled with water. Figure 6.21B is a schematic depicting the contents of the four test tubes in the phantom.

Pattern Number	R_x	R_y	$N_{ACS,x}$	$N_{ACS,y}$	R_{eff}
1	2	2	10	10	2.50
2	2	2	6	6	2.89
3	3	3	12	12	3.23
4	4	4	12	12	3.75
5	5	5	12	12	4.04
6	4	4	10	10	4.33
7	5	5	10	10	4.71

Table 6.4: The retrospectively undersampled acquisition patterns used in this phantom analysis.

factor. Two metrics were used to this end. The first metric was the root mean squared (RMS) error of the LCModel-quantified metabolite concentrations normalized by the concentration of the metabolite in the tubes in which it is present. Thus, if $C_f(i, M)$ is the concentration of the metabolite M in the ith pixel as determined using the fully-sampled dataset, $C_r(i, M)$ is the concentration of the metabolite M in the ith pixel as determined using the reconstructed dataset, and $i \in \{1, 2, ..., N\}$ is the index which runs over the N pixels in the analysis, then the RMS error can be calculated for the metabolite M as follows:

$$RMSE(M) = \sqrt{\frac{1}{N}\sum_{i=1}^{N}(C_f(i, M) - C_r(i, M))^2} \tag{6.26}$$

The second metric used to assess reconstruction accuracy was simply the mean squared error between the reconstructed datasets and the fully-sampled dataset. With this metric, the unprocessed datasets are compared, so there has been no coil combination, Fourier transformation into image space, nor LCModel quantification. Here, if $S_f(j)$ is the complex-valued signal value in the jth data point

of the fully-sampled dataset, $S_r(j)$ is the complex-valued signal value in the jth data point of the reconstructed dataset, and $j \in \{1, 2, ..., J\}$ is the index, then the RMS error of the unprocessed reconstruction is given by

$$RMSE_u = \sqrt{\frac{1}{J}\sum_{j=1}^{J}(S_f(j) - S_f(j))^2} \tag{6.27}$$

Here, J is the total number of data points in each dataset which runs over two spatial dimensions, the temporal dimension, and the coil dimension. The first metric is used to quantify the influence of the ARTT GRAPPA reconstruction on the quantification of metabolites, which is the end goal of the MRSI protocol. The second metric instead quantifies the raw error on the complete dataset introduced via the ARTT GRAPPA reconstruction.

In order to quantify local concentration deviations introduced by the GRAPPA reconstruction, a region of interest (ROI) analysis was performed. The four ROI's were taken to be the four tubes. Within each ROI, the mean and standard deviation of concentrations were calculated along with the mean and standard deviation of the Cramér–Rao lower bounds.

6.8.3 Retrospectively Undersampled *In Vivo* Experimental Setup

An *in vivo* analysis with retrospective undersampling, similar to that described in Section 6.8.2, was performed. A fully-sampled dataset was acquired in the brain of a healthy volunteer that was a 23-year old male. All imaging parameters were kept the same as in Section 6.8.2. The matrix size was 64×64, and the slice thickness was 15 mm. The FOV was 240×240 mm^2, yielding an in-plane resolution of 3.75 mm. A TR of 920 ms was used. A fully-sampled MRSI dataset was acquired in 62 minutes, and retrospective undersampling was performed. The specific undersampling patterns used are summarized in Table 6.5.

Pattern Number	R_x	R_y	$N_{ACS,x}$	$N_{ACS,y}$	R_{eff}
1	2	2	10	10	2.50
2	3	3	12	12	3.23
3	3	3	10	10	3.58
4	4	4	12	12	3.75
5	5	5	12	12	4.04

Table 6.5: The retrospectively undersampled ARTT GRAPPA acquisition patterns used in this *in vivo* analysis.

To quantify reconstruction accuracy, the same metrics utilized in the phantom analysis were reused here. These were the root mean squared error of the LCModel-quantified metabolite concentrations normalized by the mean concentration of that metabolite in the brain, as described in Equation 6.26, and the mean squared error between the reconstructed datasets and the fully-sampled dataset, as described in Equation 6.27. In addition, an ROI analysis was performed in order to quantify local concentration deviations. Two ROI's were chosen for this analysis, both of which are located in the parietal lobe of the volunteer's brain. The MRSI slice was acquired at an oblique angle which explains why both ROI's were taken to be in the parietal lobe. The positioning of these two ROI's is shown in Figure 6.22, where ROI 1 is shown in dark pink, and ROI 2 is shown in cyan.

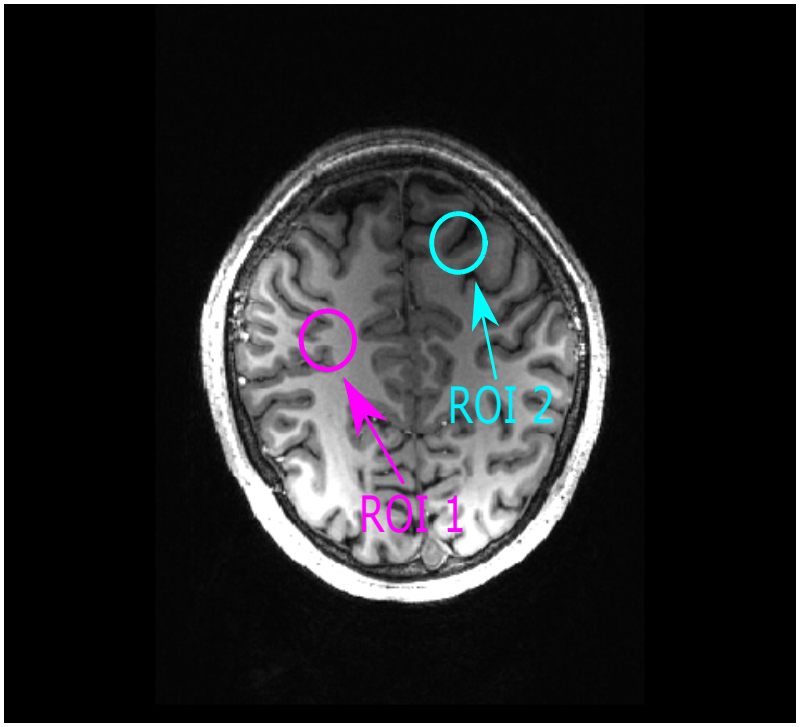

Figure 6.22: The locations of the two regions of interest in the *in vivo* local concentration analysis.

To compare ARTT GRAPPA with the conventional approach, the data were also retrospectively undersampled in a variety of conventional MRSI GRAPPA patterns. These patterns are analogous to k-space sampling patterns for GRAPPA imaging reconstructions, similar to the pattern shown in Figure 6.10A. These retrospectively undersampled datasets were then reconstructed using the conventional MRSI GRAPPA algorithm, in which a GRAPPA imaging reconstruction is applied iteratively at each time point, and relative metabolite concentrations were quantified in LCModel. The error of these reconstructions were assessed by comparison with the fully-sampled relative concentration values, and, as above, the normalized RMS error's dependence on effective acceleration factor was characterized. The reconstruction accuracy for both the novel ARTT GRAPPA approach and the conventional approach were then able to be compared. The conventional MRSI GRAPPA undersampling schemes used here are summarized in Table 6.6. Possible undersampling patterns with N_{ACS} values ranging from 8 to 12 were chosen except for the least aggressive pattern. This pattern utilized an exaggeratedly large N_{ACS} in order to try to find a conventional reconstruction pattern that produced errors comparable to the less aggressive ARTT GRAPPA reconstruction patterns.

6.8.4 Prospectively Undersampled *In Vivo* Experimental Setup

In order to demonstrate the feasibility of this accelerated ^{1}H MRSI protocol, prospectively undersampled datasets were acquired for three healthy volunteers. Volunteer 1 was a 34 year old male. Volunteer 2 was a 33 year old male. Volunteer 3 was a 25 year old male. Two accelerated acquisitions

Pattern Number	R	N_{ACS}	R_{eff}
1	2	32	1.33
2	2	10	1.78
3	3	12	2.28
4	3	8	2.46
5	4	10	2.91

Table 6.6: The retrospectively undersampled acquisition patterns used in this conventional MRSI GRAPPA *in vivo* analysis.

were performed on each volunteer: one with $R_{\text{eff}} = 2.50$ for a 25 minute acquisition and the other with $R_{\text{eff}} = 3.58$ for a 17 minute acquisition. All imaging and parameters were kept the same. The matrix size was 64×64, and the slice thickness was 15 mm. The FOV was 240×240 mm^2, yielding an in-plane resolution of 3.75 mm. A TR of 920 ms was used.

6.8.5 Homogeneous Phantom Experimental Setup

In order to assess the influence of the spatial-spectral correlations in MRSI data, an additional phantom experiment was performed. This phantom, which is shown in Figure 6.23, is spherical in shape and homogeneously filled with a solution containing lithium lactate and sodium acetate. Both compounds have a spatially homogeneous concentration of 100 mM. Since each voxel in the phantom contains the same spectral signature, there are no spatial-spectral correlations for the ARTT GRAPPA reconstruction algorithm to exploit. Here, a fully-sampled dataset of this phantom was acquired. As before, the matrix size was 64×64, and the slice thickness was 15 mm. The FOV was 240×240 mm^2. A TR of 920 ms was used corresponding to an acquisition time of 62 minutes. As before, retrospective undersampling and subsequent reconstruction was performed using both the ARTT GRAPPA and the conventional GRAPPA approaches. This had a very similar experimental setup as in Section 6.8.3, but the key difference is that the phantom is spatially and spectrally homogeneous.

Pattern Number	R	N_{ACS}	R_{eff}
1	3	8	2.46
2	5	9	3.20
3	6	10	3.56
4	6	10	3.76
5	7	10	4.00

Table 6.7: The retrospectively undersampled acquisition patterns used in this conventional MRSI GRAPPA homogeneous phantom analysis.

As before, a number of ARTT GRAPPA reconstructions and conventional MRSI GRAPPA reconstructions were performed. Unlike the *in vivo* results that will be presented below in Section 7.1.3, it was found that the conventional MRSI GRAPPA approach performs similarly to the ARTT GRAPPA approach. This is discussed in more detail in Section 7.2, however, it induced a modified conventional MRSI GRAPPA sampling pattern profile in this experiment. In particular, the conventional MRSI GRAPPA undersampling schemes utilized here were more aggressive than those used in Section 6.8.3 and are shown in Table 6.7. These sampling patterns were chosen so that their effective acceleration factors match most closely with the ARTT GRAPPA sampling patterns and a bijective comparison could most easily be made. The ARTT GRAPPA undersampling schemes used were the same as in the

Figure 6.23: The homogeneous spectroscopy phantom.

in vivo experiment and are listed above in Table 6.5. The concentrations of the two metabolites were quantified by integrating under the specified peak since these artificial metabolites are not contained in the provided LCModel basis set. The reconstructed metabolite concentrations were then compared with the fully-sampled metabolite concentrations, and the behavior of the normalized RMS error of the concentration as a function of effective acceleration factor was characterized for both compounds.

6.9 Data Processing

After the data are acquired, the ARTT GRAPPA reconstruction algorithm described in Section 6.4 was applied to reconstruct the missing data points. Following reconstruction the multi-voxel SVD-based coil combination algorithm described in Section 6.5 was applied to combine the individual receiver coil elements. Next, the L_2 regularization algorithm described in Section 6.6 was applied to remove the errant lipid signal from the data. Gaussian filtering [322] was then performed in the spectral domain. In particular, if $\vec{y}$ is the unfiltered FID, δ is a time constant, and BW is the bandwidth, then the filtered FID $\vec{y'}$ is given by

$$\vec{y'} = \vec{y}e^{-\frac{\delta^2}{BW^2}t^2} \tag{6.28}$$

Here, a time constant of 10 Hz was used.

Metabolite concentrations were then quantified using LCModel, as described in Section 6.7. After LCModel quantification, the metabolite maps were transformed back into k-space and two-fold zero filling [323] was applied along both spatial dimensions so that the imaging matrix size was increased

to 128×128. After transformation back into image space, a spatial Hamming filter was applied in both spatial dimensions. If w_n is the windowed data point, n is spatial index, N is the number of data points, and $a_0 = 0.54$ is the Hamming coefficient, a one-dimensional spatial Hamming filter [324] is described by:

$$w_n = a_0 - (1 - a_0)\cos(\frac{2\pi n}{N}) \tag{6.29}$$

The two-dimensional analog of Equation 6.29 was applied to each metabolite map.

Chapter 7

Results

7.1 Proof-of-Concept

7.1.1 Simulation Studies

When performing a GRAPPA reconstruction, a number of parameters need to be specified in advance. These include the acceleration factor R, the number of acquired autocalibration lines N_{ACS}, the kernel dimension in the fully-sampled direction K_x, and the distance S between consecutive kernel positions as it traverses the autocalibration region. In order to get a sense how varying these parameters affects the quality of reconstruction, simulations studies were first performed.

Each parameter was successively varied in order to characterize the reconstruction accuracy's dependence on that parameter. Reconstruction accuracy was quantified by taking the normalized mean squared error of the entire dataset, as described by Equation 6.25. The results are shown in Figure 7.1 for the acceleration factor (7.1A), number of ACS lines (7.1B), kernel dimension in the fully-sampled direction (7.1C), and step size (7.1D). In Figure 7.1A, it can be seen that as acceleration factor is increased, the accuracy of the reconstruction degrades which makes sense since less data have been sampled. By the same logic, in figure 7.1B, as the number of ACS lines is increased, the accuracy of the reconstruction improves, rapidly at first but then only marginally as N_{ACS} is increased further. Here, it is shown that an optimal N_{ACS} range exists between 8 and 12. As N_{ACS} is decreased past 8, the reconstruction accuracy rapidly degrades, and as N_{ACS} is increased past 12, no real benefit in reconstruction accuracy is observed to make up for the reduced image acceleration that accompanies an increase in N_{ACS}. These conclusions are specific for the 64×64 imaging matrix size chosen in these simulations which is the matrix size ultimately used in later studies. In Figure 7.1C, it is seen that smaller kernel sizes are preferred, and in Figure 7.1D, a unit step size is shown to produce the optimal reconstruction. In all further implementations, a kernel size of 3 and a step size of 1 were chosen.

7.1.2 Retrospectively Undersampled Phantom Analysis

Figure 7.2 shows reconstructed spectra via ARTT GRAPPA from a representative voxel obtained with effective accelerations of $R_{\text{eff}} = 2.50$ (7.2A), $R_{\text{eff}} = 3.23$ (7.2B), $R_{\text{eff}} = 4.04$ (7.2C), and $R_{\text{eff}} = 4.71$ (7.2D). The voxel shown here was inside tube 2 and, thus, had choline and creatine in concentrations of 100 mM and 50 mM, respectively. These reconstructed spectra are shown in red and are overlaid

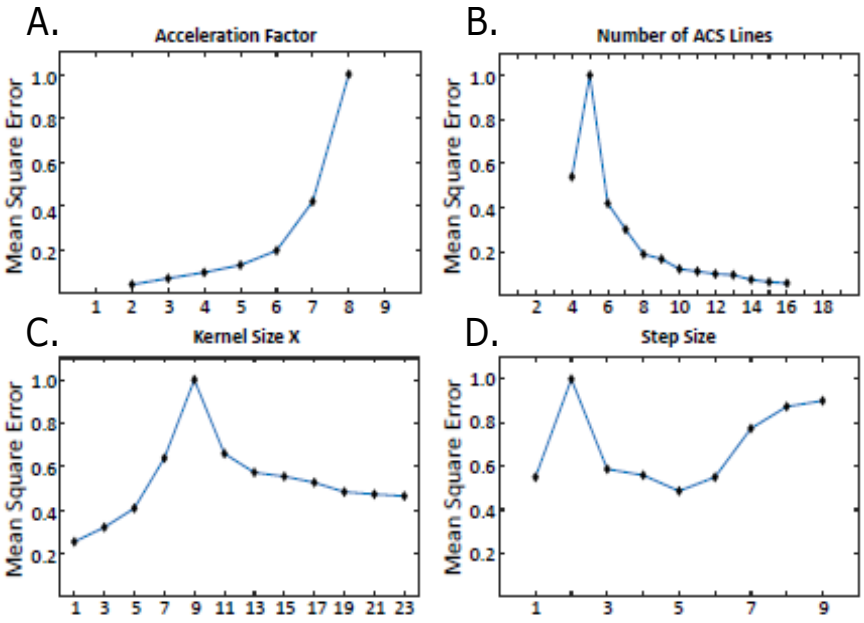

Figure 7.1: A characterization of how the accuracy of the reconstruction depends on the acceleration factor (7.1A), the number of ACS lines (7.1B), the kernel size in the fully sampled dimension (7.1C), and the step size (7.1D) - These results were obtained via simulation studies.

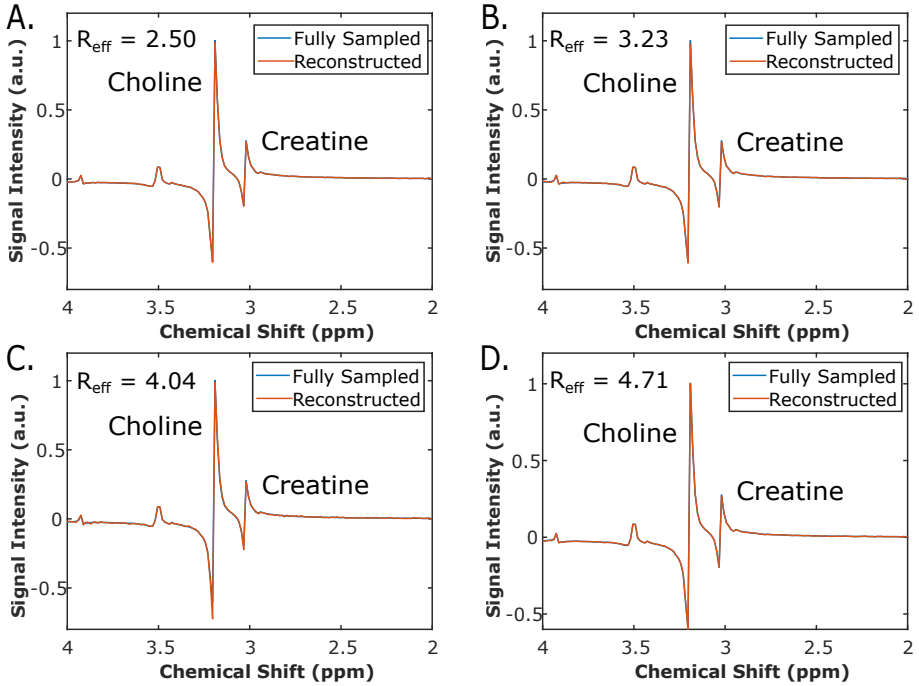

Figure 7.2: Reconstructed spectra in a representative voxel contained in tube 2 of the phantom overlaid on top of the fully-sampled spectrum in that voxel - The reconstructed spectra are shown in red, and the fully-sampled spectra are shown in blue. The reconstructed spectra utilized effective accelerations of $R_{\text{eff}} = 2.50$ (7.2A), $R_{\text{eff}} = 3.23$ (7.2B), $R_{\text{eff}} = 4.04$ (7.2C), and $R_{\text{eff}} = 4.71$ (7.2D). No significant spectral deviations are observed, even for the most aggressive undersampling schemes.

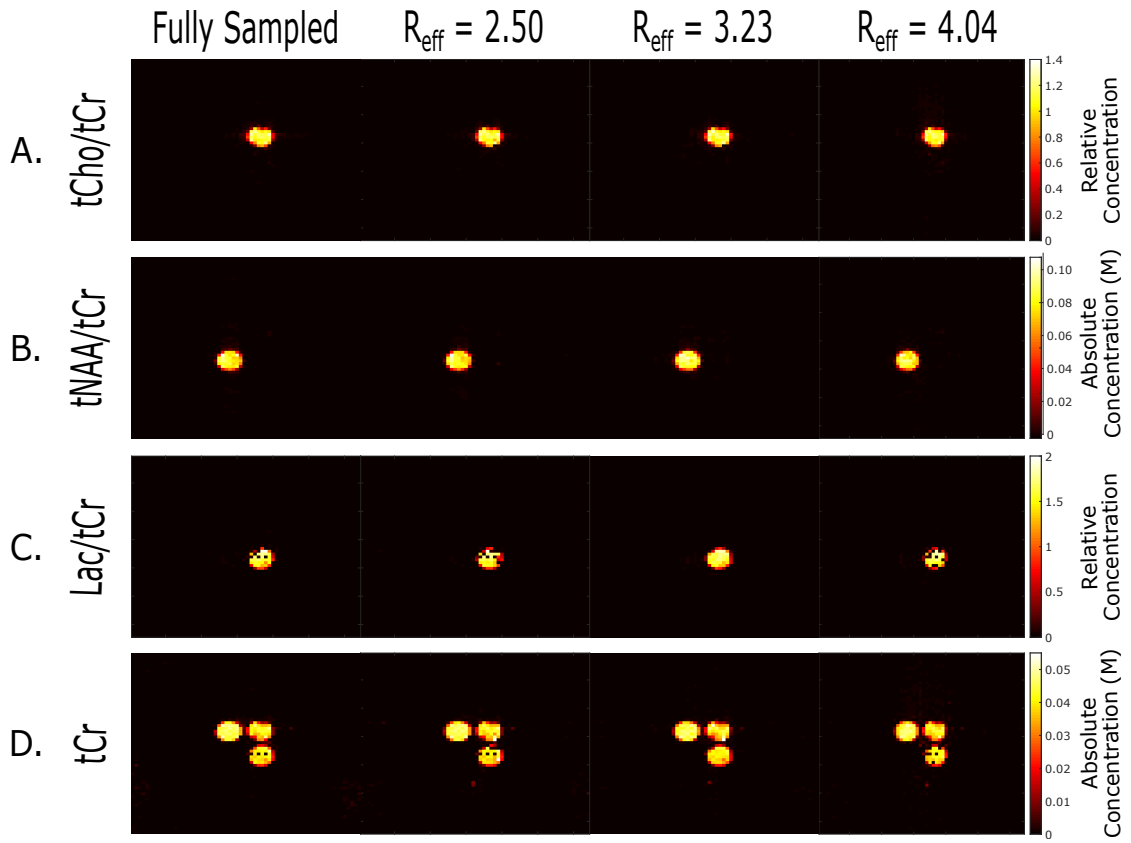

Figure 7.3: Phantom metabolite maps for total choline (7.3A), total NAA (7.3B), lactate (7.3C), and total creatine (7.3D) - These metabolite maps are those produced from the fully-sampled dataset and the reconstructed datasets for which $R_{\text{eff}} = 2.50$, $R_{\text{eff}} = 3.23$, and, $R_{\text{eff}} = 4.04$.

on top of the fully-sampled spectrum from this voxel shown in blue. As can be seen, the reconstructed spectra very accurately recapitulate the fully-sampled spectrum for modest all the way up to very aggressive acceleration.

The phantom metabolite maps are shown in Figure 7.3. Here, the fully-sampled metabolite maps along with the reconstructed metabolite maps for which $R_{\text{eff}} = 2.50$, $R_{\text{eff}} = 3.23$, and, $R_{\text{eff}} = 4.04$ are shown for total choline (7.3A), total NAA (7.3B), lactate (7.3C), and total creatine (7.3D). The metabolite maps depicting total choline and lactate are both shown normalized by total creatine concentration which is the convention in ^{1}H spectroscopy, while the total NAA (tNAA) and total creatine (tCr) maps are in an absolute scale. NAA is expressed in an absolute scale since there is no creatine in tube 3. It can be seen that the ARTT GRAPPA reconstruction is working quite well since the reconstructed metabolite maps qualitatively resemble the fully-sampled metabolite map for each metabolite in the phantom. Negligible amounts of aliasing are observed even in the metabolite maps with greater than four-fold acceleration. Any discernible differences that are observed between the different reconstructions, which are negligible, more represent fluctuations in the performance of LCModel than systematic influences introduced by the reconstruction process.

The quantification of reconstruction accuracy is shown in Figure 7.4A where metabolite-specific nor-

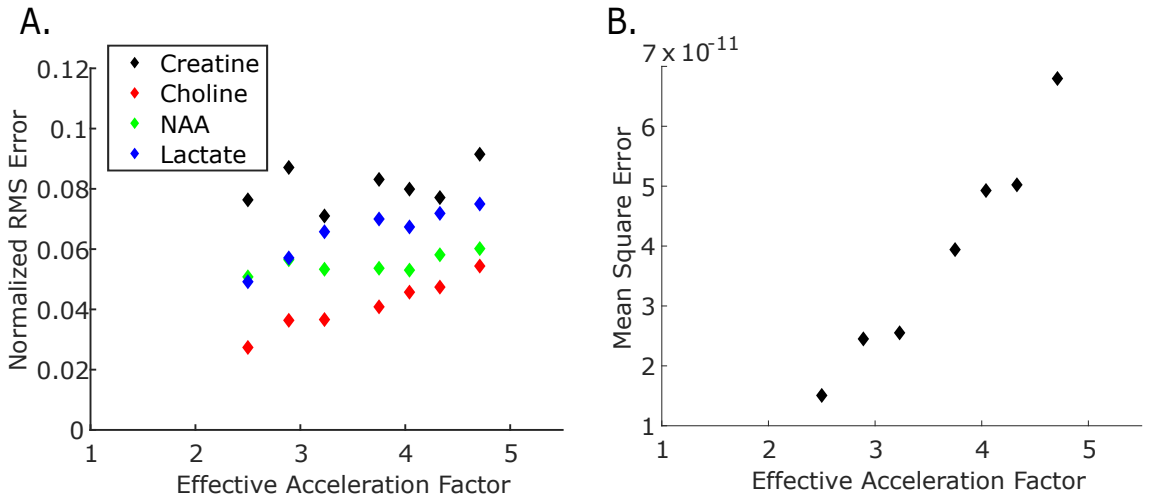

Figure 7.4: Two metrics to characterize reconstruction accuracy's dependence on effective acceleration factor in this phantom analysis - Figure 7.4A plots the normalized root mean squared error of the quantified metabolite amplitudes against R_{eff}. Figure 7.4B plots the mean squared error of the unprocessed datasets against R_{eff}.

malized RMS error, as described by Equation 6.26, is plotted against R_{eff}. The error behavior for all four metabolites, creatine (black), choline (red), NAA (green), and lactate (blue), is illustrated. As is expected, the accuracy of the reconstruction degrades as R_{eff} increases for each metabolite. However, the accuracy of the reconstruction is quite stable over a wide range of accelerations, as errors stay below 10% for each metabolite even at effective accelerations up to $R_{\text{eff}} = 4.71$. The hypothesized explanation for this stability are twofold. Firstly, these spectra have a high SNR due to the supraphysiological concentrations of each metabolite in a given test tube. GRAPPA reconstructions perform better with higher SNR which explains the stability of the reconstruction at high accelerations. The fact that the GRAPPA reconstruction performs better at higher SNR can be seen from this figure since the choline peak has the highest SNR and the lowest error values while creatine has the lowest SNR and the highest error values. The other explanation as to why the algorithm performance is so stable with respect to effective acceleration factor in this phantom analysis has to do with the relative spatial homogeneity of this phantom as compared to the situation *in vivo*. When an object is more spatially homogeneous the peripheral region of k-space contains less information content. Since the undersampling of this ARTT GRAPPA pattern is primarily on the periphery of k-space, less information is lost, and the reconstruction is more robust at higher accelerations. In addition, the RMS error of the unprocessed datasets is shown in Figure 7.4B where mean squared error of the unprocessed reconstructed datasets is plotted against effective acceleration factor.

In order to quantify local concentration deviations introduced by the GRAPPA reconstruction, an ROI analysis was performed in which the concentrations and CRLB's of each metabolite across each tube for each reconstruction were calculated. The results are shown in the tables in the appendix. In particular, Tables 10.1, 10.2, 10.3, and 10.4 present the results of this ROI analysis for choline, lactate, NAA, and creatine, respectively. Each table lists both mean and standard deviation concentrations and mean and standard deviation CRLB's within a specified ROI. There are four ROI's: tube 1, tube 2, tube 3, and tube 4. For each metabolite in each ROI, the fully sampled dataset and the seven reconstructed datasets were analyzed. Concentrations are given normalized to total creatine

concentration for both total choline (10.1) and lactate (10.2), while absolute concentrations are given for total NAA (10.3) and total creatine (10.4). It can be seen from these tables that the ARTT GRAPPA reconstruction does not appreciably alter local concentrations. This can be more easily visualized in Figure 7.5 where local concentration within a specified ROI is plotted for the fully sampled dataset and the seven reconstructed datasets for choline (7.5A), lactate (7.5B), NAA (7.5C), and creatine (7.5D). The left column shows the ROI analyses in a tube for which the specified metabolite was present. No appreciable differences are observed which demonstrates that any errors introduced by the ARTT GRAPPA reconstruction are considerably less than the statistical fluctuations in LCModel quantification. The right column shows the ROI analyses in tubes for which the specified metabolite was not present. Again, no appreciable differences are observed which demonstrates that the signals due to metabolites in adjacent tubes do not bleed into the ROI. Here, the measured concentrations do not exactly match the prescribed concentrations due to inaccuracy in the phantom construction process and errant model assumptions in LCModel. For example, LCModel corrects the basis spectra to account for the shortening of relaxation times *in vivo* but such a correction is not appropriate for the quantification of metabolites in a phantom.

7.1.3 Retrospectively Undersampled *In Vivo* Analysis

While the phantom experiments demonstrated the feasibility of the ARTT GRAPPA approach, they do not give a sense of how aggressively one can accelerate an *in vivo* acquisition. Thus, a similar analysis to that done for the phantom dataset was performed on an *in vivo* dataset. The experimental setup and error assessment methods used for this study is described in Section 6.8.3.

Figure 7.6 shows the reconstructed spectra (red) overlaid on top of the fully-sampled spectrum (blue) in a representative voxel for the five undersampling schemes. At low accelerations, the reconstructed spectrum very accurately matches the fully-sampled spectrum. This match qualitatively starts to degrade as effective acceleration factor is increased, although the performance is still quite good up to an acceleration of $R_{\text{eff}} = 3.75$. At an effective acceleration of $R_{\text{eff}} = 4.04$, the two spectra no longer match well is some regions, which surely will affect the accuracy of the metabolite quantification.

High-resolution metabolite maps of tCho, tNAA, glutamine + glutamate (Glx), and tCr were obtained for each undersampling pattern and are shown in Figure 7.7. In each subfigure, the fully-sampled metabolite map is presented along with the reconstructed metabolite maps for which $R_{\text{eff}} = 2.50$, $R_{\text{eff}} = 3.23$, $R_{\text{eff}} = 3.58$, $R_{\text{eff}} = 3.75$, and $R_{\text{eff}} = 4.04$. Figure 7.7A shows the total choline concentration normalized by the total creatine concentration. Figure 7.7B shows the total NAA concentration normalized by the total creatine concentration. Figure 7.7C shows the glutamine + glutamate concentration normalized by the total creatine concentration. Lastly, Figure 7.7D shows the total creatine concentration approximately in mM. Qualitatively, one observes good recapitulation of the fully-sampled choline, Glx, and total creatine maps for accelerations up to and including $R_{\text{eff}} = 3.58$ but sees deviations at more agressive effective accelerations. For total NAA, one observes that even the most aggressive reconstructed metabolite maps accurately recapitulate the fully-sampled map. This superior performance in reconstructing NAA maps is due to the fact that the SNR of the NAA resonance in the human brain is larger than the other resonances, and, as discussed in Section 7.1.2, this reconstruction algorithm performs better in higher SNR scenarios.

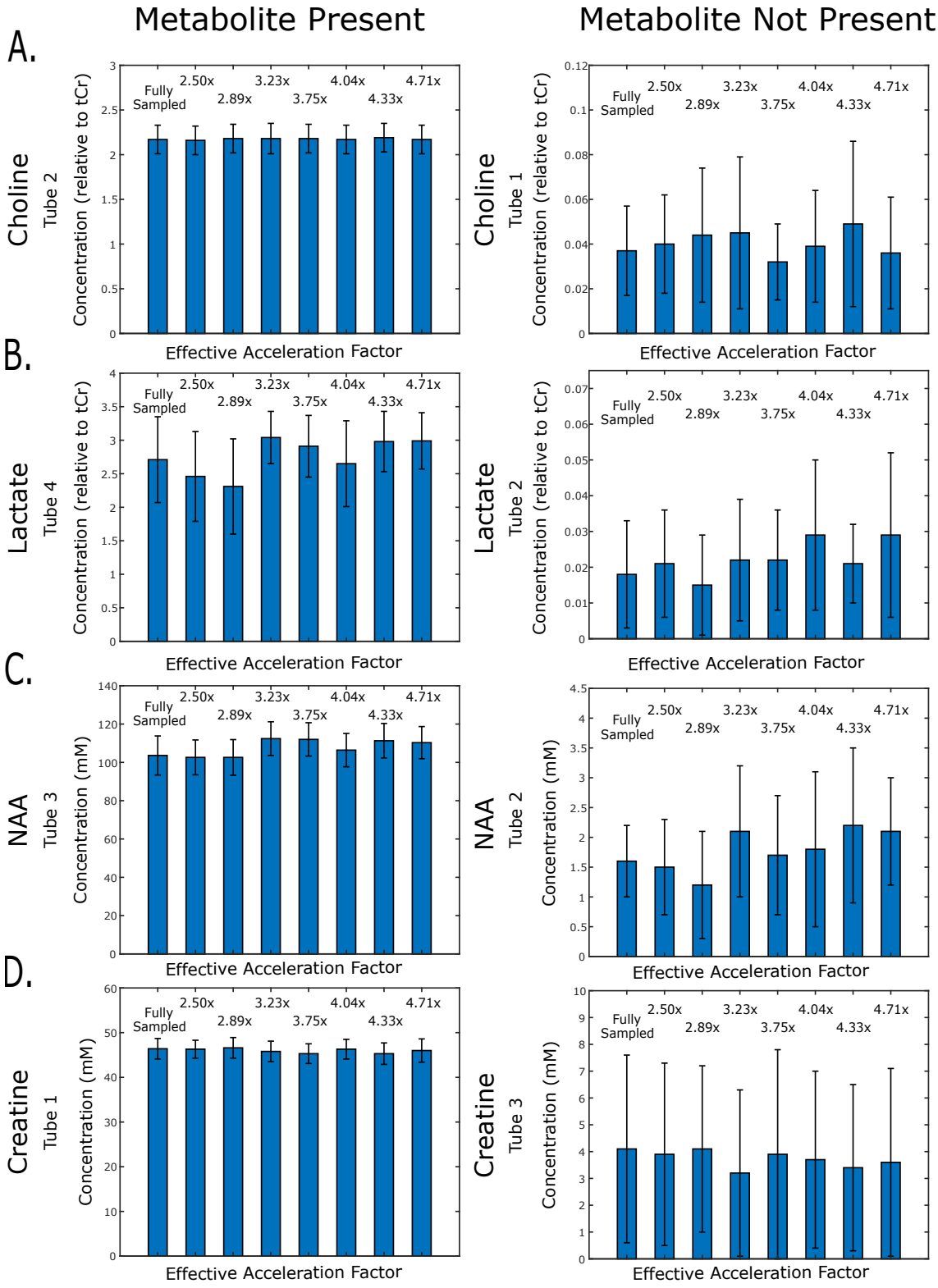

Figure 7.5: Local concentration fluctuations in representative tubes of the phantom as determined in the phantom ROI analysis.

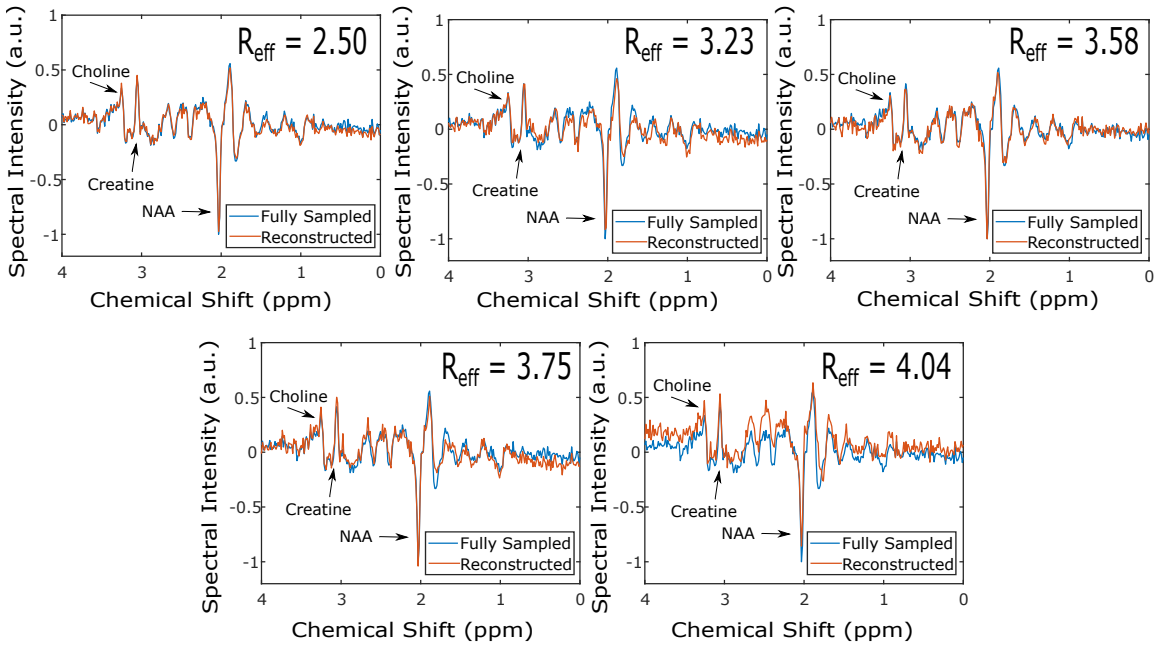

Figure 7.6: *In vivo* spectral comparisons for $R_{\text{eff}} = 2.50$, $R_{\text{eff}} = 3.23$, $R_{\text{eff}} = 3.58$, $R_{\text{eff}} = 3.75$, and $R_{\text{eff}} = 4.04$ - The reconstructed spectra are shown in red, and the fully-sampled spectra are shown in blue.

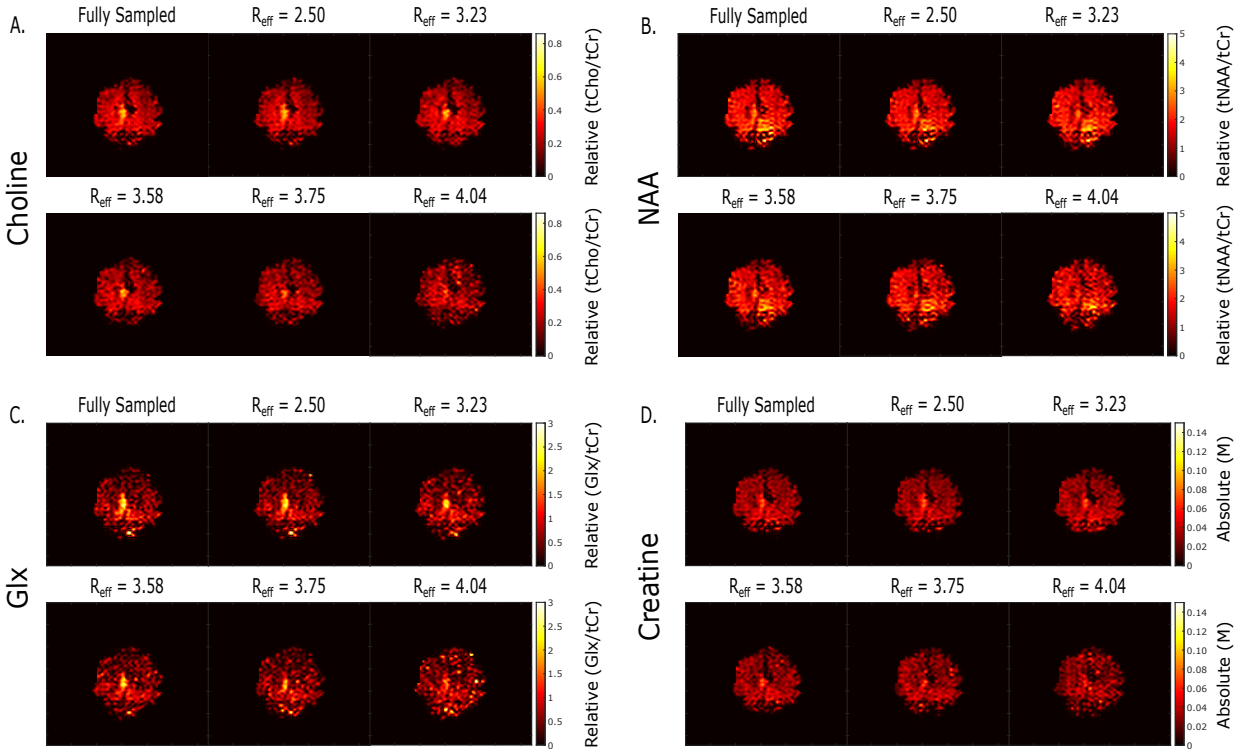

Figure 7.7: A fully-sampled metabolite map along with reconstructed metabolite maps for which $R_{\text{eff}} = 2.50$, $R_{\text{eff}} = 3.23$, $R_{\text{eff}} = 3.58$, $R_{\text{eff}} = 3.75$, and $R_{\text{eff}} = 4.04$ - These comparisons are shown for choline (7.7A), NAA (7.7B), Glx (7.7C), and creatine (7.7D). Choline, NAA, and Glx maps are shown normalized by total creatine concentration.

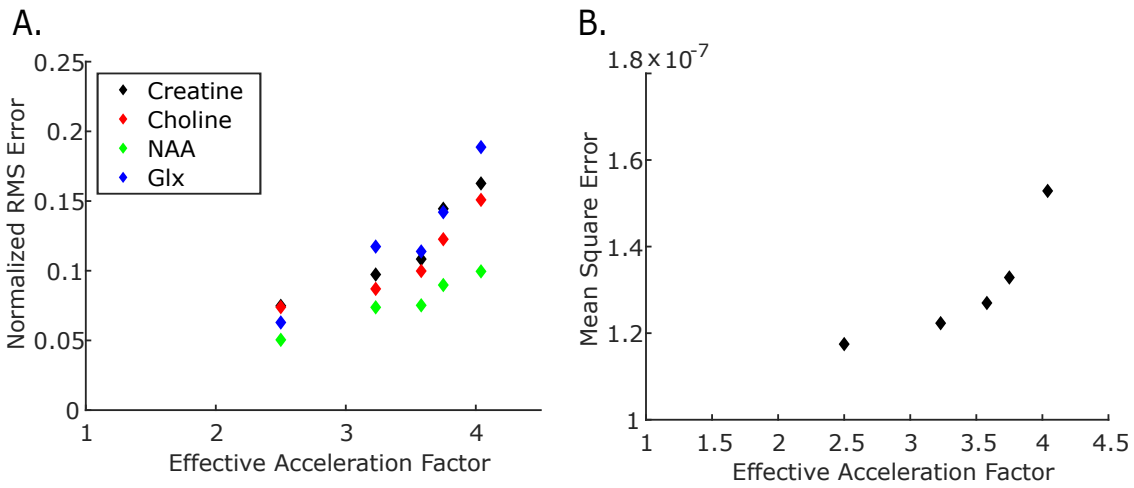

Figure 7.8: Two metrics to characterize reconstruction accuracy's dependence on effective acceleration factor in this *in vivo* analysis - Figure 7.8A plots the normalized root mean squared error of the quantified metabolite amplitudes against R_{eff}. Figure 7.8B plots the mean squared error of the unprocessed datasets against R_{eff}.

The error of each reconstruction was quantified and is displayed in Figure 7.8A, which plots the normalized RMS error against R_{eff} for tCr, tCho/tCr, tNAA/tCr, and Glx/tCr. As before, the accuracy of the reconstruction degrades as R_{eff} increases for each metabolite. If one aims for a reconstruction accuracy within approximately 10%, an effective acceleration of $R_{\text{eff}} = 3.58$ can be achieved. As the acceleration becomes increasingly more aggressive, errors in metabolite quantification become larger than is deemed acceptable. Also, as before, the second metric used was the mean squared error between the reconstructed dataset and the fully-sampled dataset. This is shown in Figure 7.8B where mean squared error of the unprocessed reconstructed datasets is plotted against effective acceleration factor. While it is difficult to make any absolute statement about this plot since the units of the MSE are not so meaningful, it can be observed that the mean squared errors obtained in this *in vivo* analysis are orders of magnitude larger than the mean squared errors obtained in the phantom analysis, as should be expected due to the lower SNR in this *in vivo* dataset.

In order to quantify local concentration deviations introduced by the GRAPPA reconstruction, an ROI analysis was performed in which the concentrations and CRLB's of each metabolite for each reconstruction were calculated within two ROI's. Both ROI's were in the parietal lobe of the brain and are depicted in Figure 6.22. The results are shown in the tables in the appendix. In particular, tables 10.5, 10.6, 10.7, and 10.8 present the results of this ROI analysis for choline, NAA, Glx, and creatine, respectively. Each table lists both mean and standard deviation concentrations and mean and standard deviation CRLB's within a specified ROI. For each metabolite in each ROI, the fully sampled dataset and the five reconstructed datasets were analyzed. Concentrations are given normalized to total creatine concentration for total choline (10.5), total NAA (10.6) and Glx (10.7), while absolute concentrations are given for and total creatine (10.8). It can be seen from these tables that the ARTT GRAPPA reconstruction does not appreciably alter local concentrations. This can be more easily visualized in Figure 7.9 where local concentration within a specified ROI is plotted for the fully sampled dataset and the seven reconstructed datasets for choline (7.9A), lactate (7.9B), NAA (7.9C), and creatine (7.9D). The left column shows the ROI analyses in ROI 1, and the right column

shows the ROI analyses in ROI 2. No appreciable differences are observed which demonstrates that any errors introduced by the ARTT GRAPPA reconstruction are considerably less than the statistical fluctuations in LCModel quantification. Thus, it is demonstrated that the use of ARTT GRAPPA does not markedly alter metabolite concentrations in an *in vivo* setting.

7.1.4 Prospectively Undersampled *In Vivo* Images

To demonstrate the feasibility of this protocol, prospectively undersampled data were acquired on three healthy volunteers. Figure 7.10 depicts all metabolite maps for one of the healthy volunteers. In this figure, the metabolite maps are overlaid on top of anatomical images. Metabolite maps are shown for total choline, total NAA, glutamine + glutamate, and total creatine for both effective acceleration factors: $R_{\text{eff}} = 2.50$ (7.10A) and $R_{\text{eff}} = 3.58$ (7.10B). Concentrations are given normalized to total creatine concentration for total choline, total NAA, and Glx, while absolute concentrations are given for and total creatine. Figure 7.11 shows accelerated choline and NAA maps produced at the lower acceleration ($R_{\text{eff}} = 2.50$) for all three volunteers. Figure 7.12 shows accelerated choline and NAA maps produced at the higher acceleration ($R_{\text{eff}} = 3.58$) for all three volunteers. As usual, both choline and NAA maps are normalized relative to total creatine concentration. Hence, the viability of the ARTT GRAPPA technique in producing accelerated metabolic images is illustrated.

7.1.5 Proof-of-Concept Summary

Throughout this section, the feasibility of an ARTT GRAPPA reconstruction for the acceleration of ^{1}H MRSI has been demonstrated in the human brain at 7 T. High-resolution metabolite maps have been produced with an acquisition time less than twenty minutes while maintaining less than a 10% error relative to the fully-sampled dataset. Simulations were initially performed to optimize some of the reconstruction parameters. The feasibility of the ARTT GRAPPA reconstruction was first demonstrated in a phantom followed by a retrospectively undersampled *in vivo* experiment. Finally, three prospectively undersampled datasets were acquired, and accelerated metabolite maps were produced.

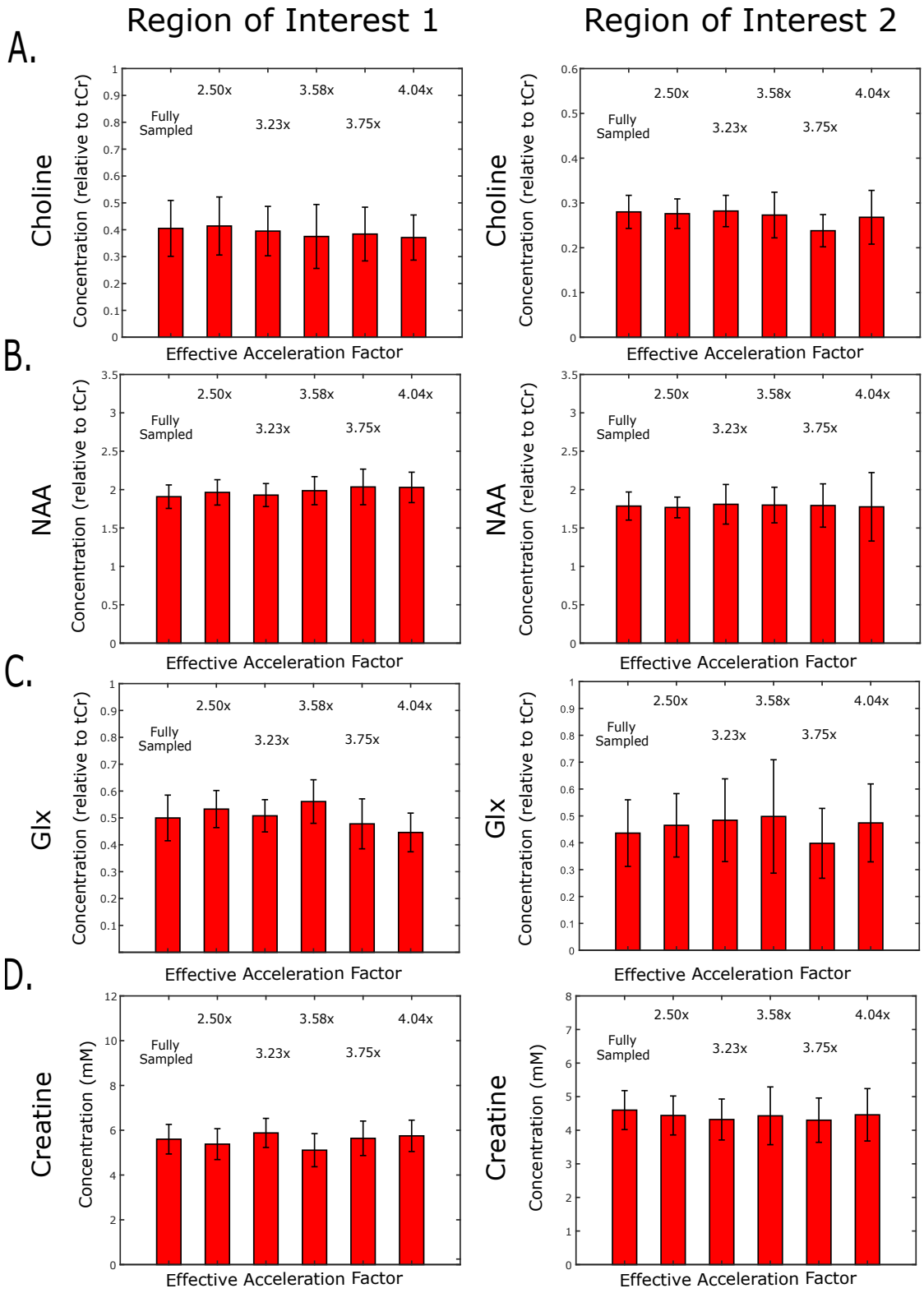

Figure 7.9: Local concentration fluctuations in two regions of interest in the brain of a healthy volunteer.

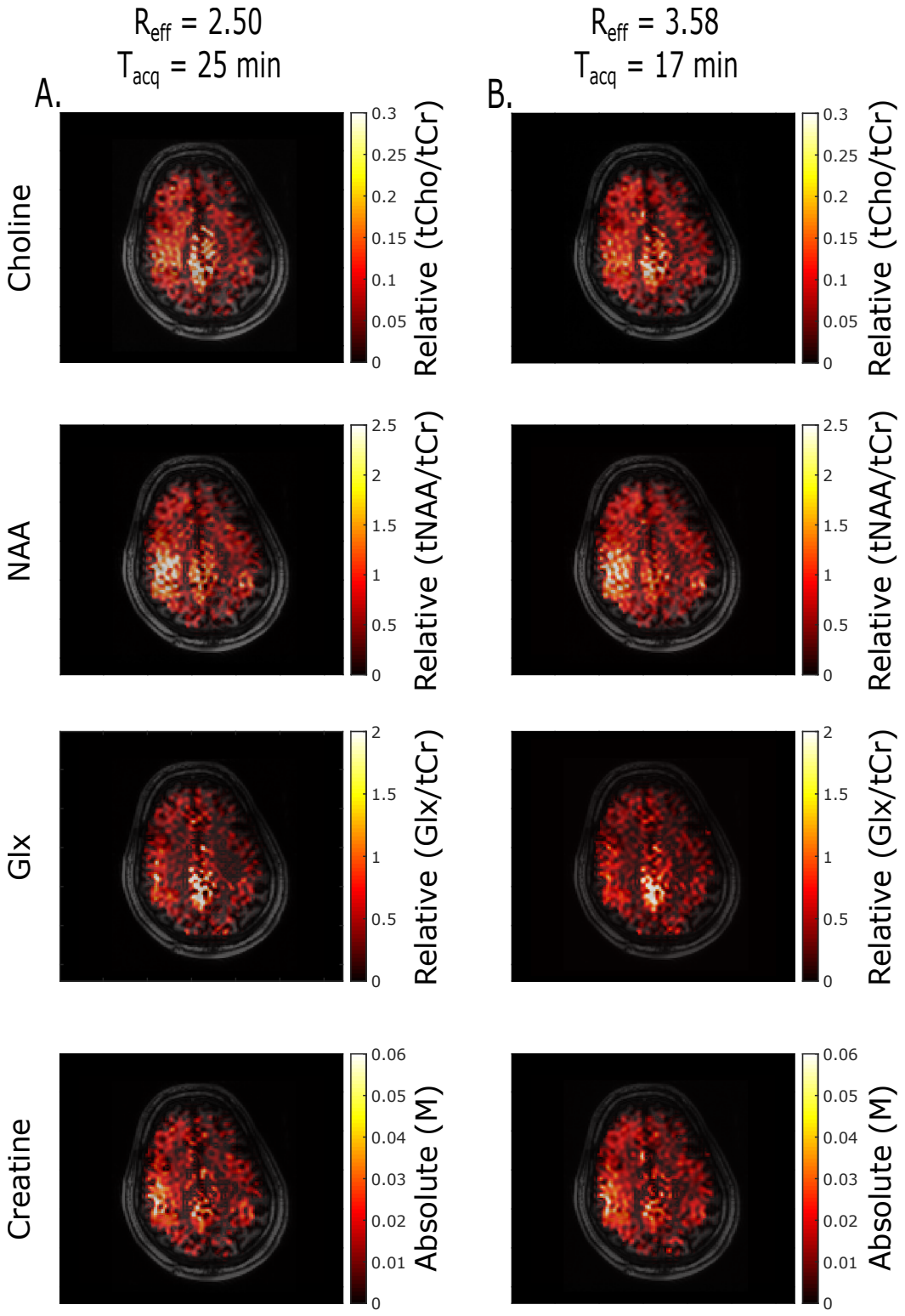

Figure 7.10: Prospectively undersampled metabolite maps from Volunteer 1 - Metabolite maps are shown for choline, NAA, Glx, and creatine for both effective acceleration factors: $R_{\text{eff}} = 2.50$ (7.10A) and $R_{\text{eff}} = 3.58$ (7.10B).

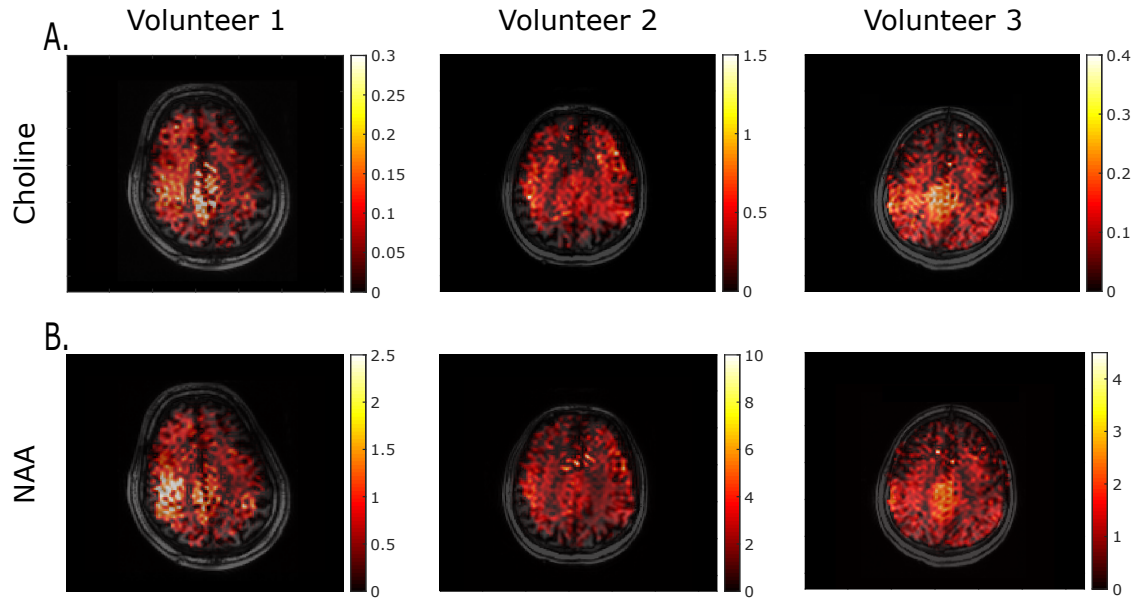

Figure 7.11: Choline (7.11A) and NAA (7.11B) maps acquired with $R_{\text{eff}} = 2.50$ for each of the three healthy volunteers - These images were acquired in 25 minutes.

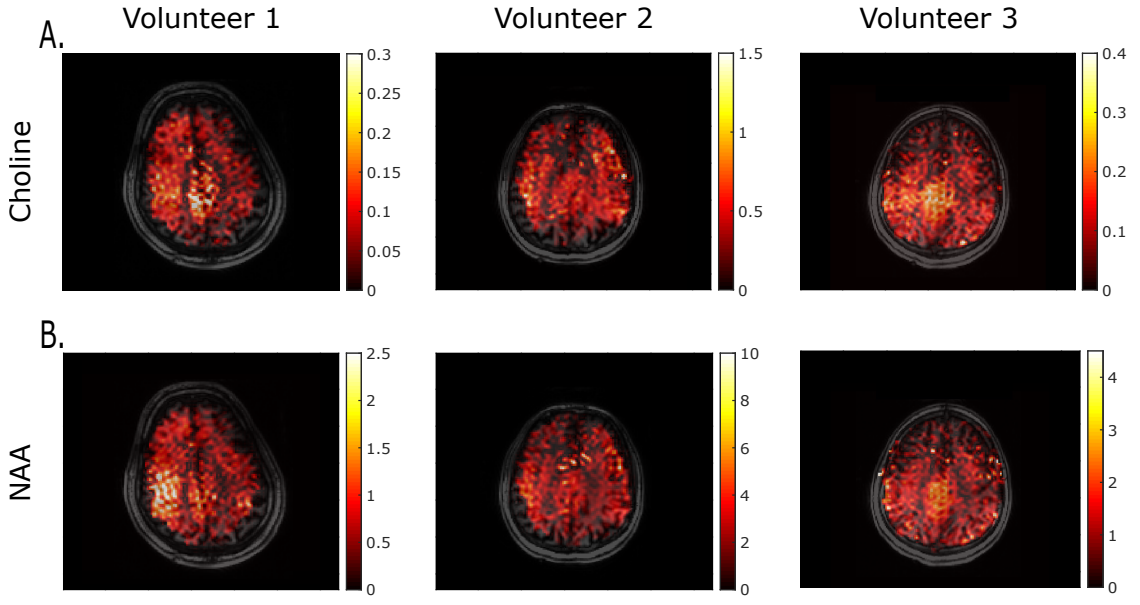

Figure 7.12: Choline (7.12A) and NAA (7.12B) maps acquired with $R_{\text{eff}} = 3.58$ for each of the three healthy volunteers - These images were acquired in 17 minutes.

7.2 Comparison to the Conventional Technique

7.2.1 Retrospectively Undersampled *In Vivo* Studies

In section 7.1, the feasibility of using ARTT GRAPPA to accelerate ^{1}H MRSI acquisitions has been demonstrated. This section will compare the ARTT GRAPPA approach with the conventional approach. In conventional MRSI GRAPPA, a standard GRAPPA imaging algorithm, as described in Section 5.5, is applied iteratively over each timepoint in the FID individually. A straightforward bijective comparison between ARTT GRAPPA and conventional MRSI GRAPPA is not possible. This is because conventional MRSI GRAPPA only accelerates along a single dimension, so the set of effective acceleration factors corresponding to possible conventional MRSI GRAPPA undersampling schemes is not the same the set of effective acceleration factors corresponding to possible ARTT GRAPPA undersampling schemes. However, conventional MRSI GRAPPA sampling schemes similar in effective acceleration factor to the ARTT GRAPPA sampling schemes were chosen.

The results of this comparison are illustrated in Figure 7.13. Figures 7.13 A, B, C, and D depict the errors in choline, NAA, creatine, and Glx concentrations, respectively. It can be seen that the ARTT GRAPPA reconstruction algorithm markedly outperforms the conventional MRSI GRAPPA reconstruction algorithm. In particular, the ARTT GRAPPA approach allows one to accelerate approximately twice as aggressively as the conventional approach if the same level of reconstruction accuracy is to be achieved. For a quantitative example of this, refer to the choline concentrations shown in Figure 7.13A. The conventional MRSI GRAPPA sampling pattern with an effective acceleration of $R_{\text{eff}} = 1.33$ matches the fully-sampled dataset to within 8.6%. With ARTT GRAPPA, the undersampling scheme that achieves similar accuracy (8.7%) has an effective acceleration factor of $R_{\text{eff}} = 3.23$. Thus, a 19-minute scan reconstructed using ARTT GRAPPA produces similarly accurate metabolite maps as a 47-minute scan reconstructed using conventional MRSI GRAPPA. As a further example with choline concentrations, the conventional MRSI GRAPPA sampling pattern with an effective acceleration of $R_{\text{eff}} = 1.78$ matches the fully-sampled dataset to within 13.0%. Compare this with the ARTT GRAPPA with an effective acceleration of $R_{\text{eff}} = 3.75$ which matches the fully-sampled dataset to within 12.2%. Thus, a 16-minute scan reconstructed using ARTT GRAPPA produces more accurate metabolite maps than a 35-minute scan reconstructed using conventional MRSI GRAPPA. Similar statements can be made for the other three metabolites depicted in Figure 7.13 as well. Thus, the novel ARTT GRAPPA reconstruction presented in this work performs markedly better and allows for more aggressive acceleration than the conventional approach.

7.2.2 Potential Mechanistic Explanation

In the previous section, it was shown that ARTT GRAPPA markedly outperforms conventional MRSI GRAPPA in an *in vivo* setting. This is likely due to the fact that the ARTT GRAPPA approach, by construction, simultaneously exploits correlations in both the spatial and spectral domains. In order to test the veracity of this hypothesis, an additional experiment was performed on the homogeneous phantom described in Section 6.8.5. The results of this analysis are shown in Figure 7.14 for sodium acetate (7.14A) and lithium lactate (7.14B). It can be seen that the two algorithms perform similarly for both metabolites. Thus, in this phantom, where there are no spatial-spectral correlations to exploit, the advantage of ARTT GRAPPA over conventional MRSI GRAPPA is negated.

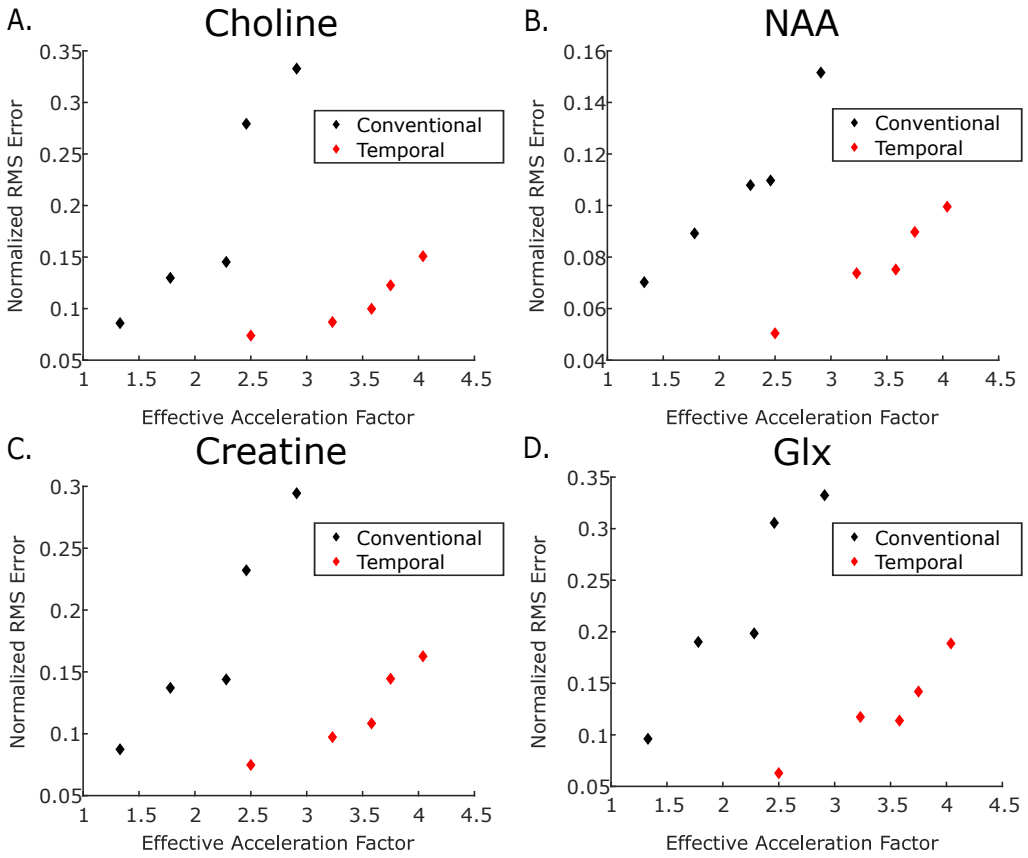

Figure 7.13: A comparison between the ARTT GRAPPA reconstruction and the conventional MRSI GRAPPA reconstruction *in vivo* for total choline (7.14A), total NAA (7.14B), total creatine (7.14C), and glutamine + glutamate (7.14D) - Normalized RMS error is plotted as a function of effective acceleration factor. The ARTT GRAPPA reconstruction performs markedly better than the conventional reconstruction.

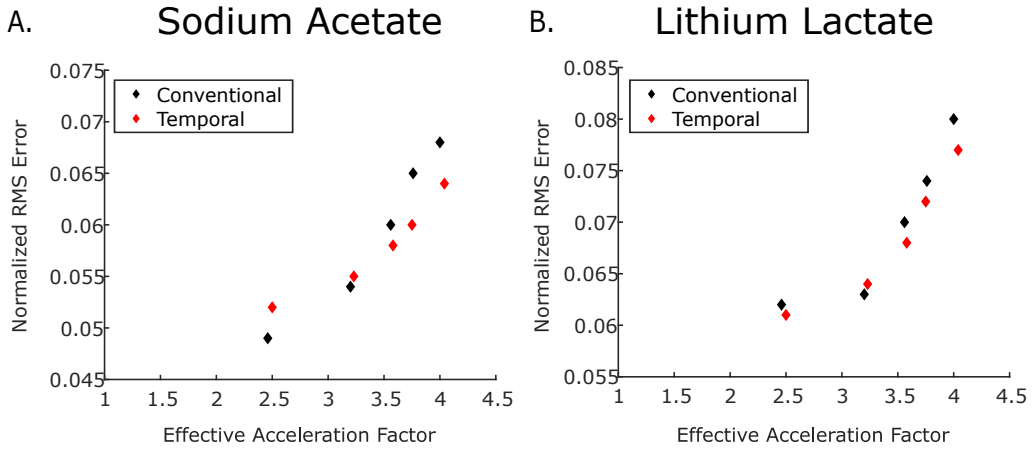

Figure 7.14: A comparison between the ARTT GRAPPA reconstruction and the conventional MRSI GRAPPA reconstruction in a homogeneous phantom containing sodium acetate (7.14A) and lithium lactate (7.14B) - Normalized RMS error is plotted as a function of effective acceleration factor. When no spatial-spectral correlations are available to exploit, the two algorithms perform similarly.

Chapter 8

Discussion

8.1 Technical Considerations

8.1.1 High Field Strength

As discussed in Section 4.6, there are numerous advantages and disadvantages to higher field MRSI. The benefits are threefold: a higher SNR, larger spectral dispersion, and a reduction of the effects of J-coupling. The higher SNR allows for higher spatial resolution in a shorter acquisition time. Major disadvantages include more pronounced field inhomogeneities, both B_0 and B_1, and shorter T_2 relaxation times. In this work, the shorter T_2 relaxation times were compensated for by using ultra short echo times which minimizes the time that the magnetization has to relax. The increased B_1 inhomogeneities were compensated, at least in regards to water suppression, by using VAPOR which is optimized to be stable in the presence of B_1 inhomogeneities. In addition, the employed pulse sequence FID MRSI also maintains robustness of low flip angle excitation pulses in the presence of B_1 inhomogeneities. The increased B_0 inhomogeneities were the most problematic, especially in pixels nearby tissue-air interphases. The system's three-dimensional shim algorithm was performed prior to each MRSI experiment to correct for static field inhomogeneities, but it was difficult to obtain linewidths less than 30 Hz. At times, these spectral peaks were then too broad for proper metabolite quantification in LCModel, as the algorithm would be unable to identify a peak that was clearly present. This occurred most often in creatine quantification. The other possibility for shimming is using the system's fast automatic shimming technique by mapping along projections (FASTMAP) algorithm [325]. The FASTMAP algorithm and its variants [326, 327] measure the inhomogeneity in the static field in a localized region along a number of linear projections and determine the spherical harmonic coefficients corresponding to the shim corrections. Using FASTMAP in these experiments yielded smaller linewidths but in a localized region much smaller than the desired FOV. Therefore, it was ultimately decided to proceed with the three-dimensional shim algorithm and accept the large linewidth in exchange for a larger shim volume. Newer 7 T systems are being designed with more sophisticated shim systems which can achieve higher levels of B_0 homogeneity, but while using this system, some level of B_0 inhomogeneity is an unavoidable consequence of working at higher fields.

8.1.2 Pulse Sequence Considerations

At clinical field strengths, single-voxel spectroscopy is typically performed using a sequence known as point resolved spectroscopy (PRESS) [328]. Spatial localization in PRESS is accomplished using a 90°

excitation pulse followed by two 180° refocusing pulses [329]. However, at higher field strengths, the chemical shift displacement artifact becomes too pronounced within reasonable RF energy deposition limits, so the use of PRESS is not recommended at high fields [330]. PRESS is also rather sensitive to B_1 inhomogeneities. Alternatives to PRESS at high field strength include localization by adiabatic selective refocusing (LASER) [331], stimulated echo acquisition mode (STEAM) [332], and spin-echo full-intensity acquired localized (SPECIAL) [333]. However, the sequence semi-LASER [334] which is a combination of conventional excitation with full localization via the adiabatic selective refocusing used in LASER [335] is now accepted within the community as the preferred technique to acquire single-voxel spectra at high fields due to its robustness [336].

The situation is quite similar for MRSI, as PRESS is not recommended for use at high fields [198], and semi-LASER is utilized as a replacement [337]. Another approach that is entirely different simplifies localization to the direct acquisition of an FID [272] and has been regaining popularity in the literature. This FID MRSI technique is now considered the method of choice for ^{1}H MRSI at higher field strengths. When utilized with short echo times and repetition times it allows for minimal chemical shift displacement, high SNR, short acquisition duration, and robustness in the presence of B_1 inhomogeneities [198]. These qualities made FID MRSI the ideal pulse sequence with which to base the protocol presented in this work, so it was ultimately decided to utilize this pulse sequence.

8.1.3 Water Suppression

In order to suppress water or any particular spectral resonance for that matter, one must exploit a difference in an NMR observable parameter. Examples of exploitable properties include chemical shift, relaxation, scalar coupling, or diffusion [61]. Relaxation-based suppression techniques such as water eliminated Fourier transform (WEFT) [338] and driven equilibrium Fourier transform (DEFT) [339] have been employed by others in the past. However, since the difference between the T_1 relaxation time of water and the metabolites of interest is quite small, the sensitivity of the detected metabolites is necessarily reduced. Moreover, since the *in vivo* T_1 relaxation time of water is not homogeneous, water suppression is often incomplete.

Suppression of water is also possible after the data have been acquired. Such an algorithm was implemented. Briefly, this was accomplished by modeling the FID as a superposition of exponentially damped sinusoids, finding those components with frequencies close to the water frequency, and removing those components [340]. After applying this algorithm to spectral data, the water signal completely disappears as desired. The main disadvantage of this technique is that it is computationally intensive. The computational time required is on the order of tens of seconds to several minutes depending on the size of the spectral dimension. In a single voxel setting, this would be acceptable, but such a computational burden is not optimal in a multi-voxel setting where the artificial water suppression algorithm need be applied thousands of times, once for each voxel in the image. In addition, this technique imposes a model on the spectral data which may effect the metabolite quantification process. Thus, a technique in which water is suppressed prior to data acquisition was necessary.

As discussed in section 6.2.2, the majority of water suppression implementation in the literature utilizes frequency selective RF pulses. VAPOR is typically considered the gold standard and most commonly employed water suppression technique, so this was the technique chosen in this work. Its insensitivity

to B_1 inhomogenieties was a strong consideration in making this choice. However, implementing WET would have had its advantages as well. In particular, WET uses only three CHESS pulses, so the sequence of water suppression pulses takes less time. While the suppression may not be as complete with WET as with VAPOR and may be slightly less robust in the presence of B_1 inhomogenieties, using WET would allow the repetition time to be reduced by a factor of approximately $\frac{2}{3}$. The only requirement is that the water suppression is sufficient enough to not interfere with the metabolite concentration quantification process. If this can be achieved with WET, this would constitute a future improvement to this protocol, as the high-resolution metabolite maps would then be able to be acquired in approximately 12 minutes.

8.1.4 Lipid Suppression

Lipid suppression is a very important component of ^{1}H MRSI of the human brain. The prominent lipid resonance located at approximately 1.5 ppm has the tendency to severely degrade data quality, due to imperfect spatial localization. In particular, the side lobes of the PSF cause the pericranial lipid signal to bleed into voxels that should only contain brain tissue. A technique that eliminates these spurious signals without altering other spectral features is necessary for the application of reliable proton spectroscopic imaging.

The first class of lipid suppression algorithms are based on differences in relaxation times. The difference in T_2 relaxation between the lipid signal and the metabolite signal is not sufficiently large and is not typically used. However, the difference in T_1 relaxation between the lipid signal and the metabolite signal is much more discernible [61], and one typically exploits T_1 relaxation differences via the method of inversion recovery (IR) [341]. Here, an initial 180° pulse inverts the magnetization. The longitudinal magnetization is then negative and as time passes, T_1 relaxation processes will cause the longitudinal magnetization to become less negative, pass through a point where it has completely vanished, and eventually start to grow in the positive longitudinal direction again. If one then waits the exact time that it takes the lipid signal to recover to zero longitudinal magnetization and applies a 90° pulse, the lipid signal is eliminated. This is because, at that time, there is no lipid-originating longitudinal magnetization to be flipped into the transverse plane. However, since the 90° pulse was applied at a time specific for the lipid signal, there is still some residual metabolite-originating magnetization flipped into the transverse plane which is able to be detected. The main drawback of this technique is that the SNR of the metabolite signals is necessarily reduced which is not desirable in a high-resolution study which is already SNR-limited.

The most commonly utilized method of lipid suppression is outer volume suppression (OVS) which consists of placing multiple spatially selective saturation bands over all regions containing lipids [342]. This technique first excites narrow slices that contain the sources of the pericranial lipid signal. A crusher gradient is then applied to dephase the transverse magnetization in a non-spectrally specific manner. Immediately after these OVS elements, brain signals not within these OVS bands can then be excited and detected.

There are, however, a number of drawbacks to using OVS that were taken into account here when deciding to go in a different direction. The first main drawback is that OVS is sensitive to B_1 inhomogeneity since its successful application requires that the OVS excitation pulse is exactly 90°.

As discussed in section 8.1.1, B_1 is never homogeneous and even less so at the high magnetic field strength of 7 T used here. When B_1 inhomogeneities exist, the achieved flip angle will differ from 90° which will cause some of the longitudinal magnetization to remain and the lipid suppression to be incomplete. Also, in the time between the OVS module and the signal excitation, there will be some nonzero T_1 relaxation causing some of the longitudinal magnetization to recover and rendering lipid suppression incomplete [61]. Another drawback is the additional time it takes to employ the pulses that achieve OVS. Since the overarching goal of this work was to minimize total acquisition time, it is advantageous to keep TR to a minimum. However, OVS is often interleaved with the water suppression protocol, so the time added to the repetition time is not a major concern. The more pertinent disadvantage of OVS is the additional RF energy deposition required by the OVS procedure. RF energy deposition can cause the patient's body temperature to rise and is quantified using a metric known as specific absorption rate (SAR) which is defined as the rate at which RF energy is absorbed by tissue during an MR procedure [343]. Regulations exist on how much SAR can safely be deposited during an examination and, if these limits are exceeded, TR must be increased until the SAR delivered is reduced to back within the allowable range. The water suppression protocol already delivers a lot of RF power, so it was advantageous to avoid additional power deposition to suppress lipids. This potential required increase in TR would also be disadvantageous since it would increase acquisition duration. Due to all of the considerations listed here, it was decided that a technique that suppresses the lipid signal without the use of OVS pulses is highly desirable.

L_2 regularization was a perfect alternative for this application. Since it achieves lipid suppression by manipulating the data after it has already been acquired, no high SAR pulses are necessary. In addition, the lipid suppression achieved via L_2 regularization, as illustrated in Section 6.6, is quite robust and certainly did not interfere in the metabolite detection and quantification process.

8.2 A Novel GRAPPA Algorithm for the Acceleration of MRSI

8.2.1 GRAPPA versus SENSE

GRAPPA and SENSE are the two major parallel imaging implementations. The superficial difference between the two techniques is that GRAPPA is performed in k-space, and SENSE is performed in image space. However, this difference is actually unsubstantial since the GRAPPA reconstruction procedure described in detail in Section 5.5 can also be recast into a convolution of the undersampled k-space dataset with a convolution kernel [314]. By applying the convolution theorem shown below, one can further recast the GRAPPA reconstruction as a pointwise multiplication in image space.

$$\mathcal{F}\{\mathbf{A} * \mathbf{B}\} = \mathcal{F}\{\mathbf{A}\}\mathcal{F}\{\mathbf{B}\} \tag{8.1}$$

Here, $\mathcal{F}$ denotes the Fourier transformation, $\mathbf{A}$ and $\mathbf{B}$ are two matrices, and $*$ denotes convolution. Thus, it is seen that the difference between image space-based reconstructions and k-space-based reconstructions is more conventional than fundamental. The coil sensitivity profile, which is explicitly measured in image space-based reconstructions but implicitly determined in k-space-based reconstructions, can be explicitly recovered in k-space-based reconstructions by taking the Fourier transformation of the convolution kernel. However, in applying the algorithm described in detail in Section 5.5, this is unnecessary, and a GRAPPA reconstruction is performed without the explicit determination of the coil sensitivity profile.

GRAPPA and SENSE are similar in that they both use the coil sensitivity profile to reconstruct undersampled data and produce an accelerated image. Fundamental differences between the two algorithms exist, and care must be taken when deciding which implementation is most appropriate for a given application. The major superficial difference between GRAPPA and SENSE, as was mentioned above, is that GRAPPA is performed in k-space and SENSE is performed in image space. However, it was also shown above that due to the convolution theorem, GRAPPA can actually be performed in image space and that this distinguishing feature between the two flavors of implementation is actually less fundamental than at first glance. The other major difference is that SENSE requires the explicit determination of the coil sensitivity profile, usually through a measurement at the beginning of the protocol, while GRAPPA determines the coil weights in a more implicit fashion using a fully-sampled central autocalibration region. Because of this ACS region, GRAPPA achieves slightly less acceleration than SENSE for a given acceleration factor. SENSE also achieves a marginally higher SNR than GRAPPA, but this difference is only noticeable at very high acceleration factors. GRAPPA is the preferred method when imaging inhomogeneous regions of the body, such as the lungs [344] or intracranial cavities [345], since it is difficult to obtain accurate coil sensitivity profiles when imaging inhomogeneous anatomy. Furthermore, SENSE is more adversely affected by patient motion since discrepancies in the patient's position at the time of data acquisition and at the time the coil sensitivity profiles are measured violates the assumptions of the SENSE algorithm. GRAPPA, in which the coil sensitivities are implicitly determined directly from the data, avoids this problem altogether and is, therefore, more robust in the presence of motion. Finally, GRAPPA is the preferred method when acquiring data using an echo planar readout, again due to the explicit calibration process employed by SENSE. Here, the magnetic susceptibility profiles, which describe a medium's propensity to become magnetized in the presence of an applied magnetic field, are different when acquiring EPI images compared to when acquiring the coil sensitivity profiles, ultimately leading to distortions in SENSE reconstructions [346]. Although this thesis does not employ an echo planar readout, it would be advantageous for this protocol to be translatable to EPSI readouts in the future. The implementation of EPSI could allow for the realization of an accelerated three-dimensional MRSI protocol. Therefore, due to the many considerations discussed above, it was ultimately decided to implement GRAPPA rather than SENSE.

8.2.2 Spatial-Spectral Correlations

In this work, a novel GRAPPA algorithm is presented to accelerate MRSI acquisitions. The GRAPPA weights are extracted from an autocalibration region in k-t space. Conventional GRAPPA, by construction, requires the full acquisition of one of the spatial dimensions, but ARTT GRAPPA no longer has this requirement and, thus, allows for undersampling along both k-space directions. In a three-dimensional acquisition, in principle, acceleration along all three dimensions would be possible. In Section 7.2, it is shown that this novel GRAPPA algorithm incontrovertibly outperforms the conventional MRSI GRAPPA technique. This is likely due to the fact that ARTT GRAPPA exploits the spatial-spectral correlations available in the data.

Parallel imaging exploits spatial correlations in the data. In particular, parallel imaging utilizes information regarding the spatial distribution and relative sensitivities of the individual receiver coil elements in a phased array. Other approaches such as partial Fourier methods [347] and reduced FOV

techniques [348] in dynamic imaging also exploit spatial correlations. Another class of techniques which have been applied to dynamic MRI examinations exploits temporal correlations in the data. These include keyhole imaging [349], unaliasing by Fourier-encoding the overlaps using the temporal dimension (UNFOLD) [350], and view sharing strategies [351]. Some techniques, however, combine both of these approaches by exploiting both spatial and temporal correlations. These methods include the Noquist method [352], UNFOLD SENSE [353], k-t SENSE [354], and k-t GRAPPA [273] and have been applied exclusively to exploit spatiotemporal correlations in dynamic MRI. The algorithm presented in this work falls into this third class of approaches but exploits these aforementioned spatiotemporal correlations in MRSI datasets, as is discussed in more detail below. As compared to dynamic MRI, MRSI has much more temporal data than dynamic acquisitions. Therefore, ARTT GRAPPA is able to reconstruct images using only the fully-sampled temporal dimension in a central region of k-space and, hence, can fully accelerate along both spatial dimensions.

Significant spatial-spectral correlations are present in MRSI datasets [355, 356]. The utility of spatial-spectral correlations can be illustrated by means of the following example. Consider an MRSI experiment investigating a human brain that contains two broad types of tissue: healthy brain tissue and tumorous brain tissue. The tumorous brain tissue can be described by a basis spectrum which, roughly speaking, has relatively high choline concentrations, intermediate creatine concentrations, relatively low NAA concentrations, and some lactate. Contrastingly, the healthy brain tissue can be described by a basis spectrum with relatively low choline concentrations, intermediate creatine concentrations, and relatively high NAA concentrations. This hypothetical dataset was acquired using a two-channel array with one channel on the left side of the brain seeing mostly tumorous brain tissue and the other channel on the right side of the brain seeing mostly healthy brain tissue but with a small metastasis present. Assume that metastasis is very small and that the SNR of the dataset is too low for the lactate concentration in the metastasis to be determined, but the choline and NAA resonances are clearly discernible. Although the lactate in the metastasis is not visible, the spatial-spectral correlations present in the data can be used to deduce the concentration of lactate in the metastasis by observing the choline and NAA levels in that pixel.

It was shown in Section 7.2, that ARTT GRAPPA allows for effectively twice as aggressive acceleration than conventional MRSI GRAPPA for an *in vivo* dataset. However, in a phantom in which every pixel has the same spectral signature, the advantage of ARTT GRAPPA disappears and the two techniques become comparable. This strongly suggests that the benefit of this approach is, in fact, the exploitation of these spatial-spectral correlations which allows for a more accurate determination of the individual receiver coil weights. In the *in vivo* dataset, where spatial-spectral correlations are present, ARTT GRAPPA markedly outperforms the conventional approach, but in a phantom dataset without spatial-spectral correlations to be exploited, the ARTT approach and the conventional approach perform similarly. This is encouraging since the desired application of this technique is clearly *in vivo* examinations.

8.2.3 Sampling with ARTT GRAPPA

The nature of how the ARTT GRAPPA algorithm works calls for unique sampling patterns. In particular, conventional GRAPPA, by construction, always requires that one of the spatial dimensions is fully-sampled. However, in ARTT GRAPPA, this is no longer a requirement, so greater flexibility in

possible sampling schemes is allowed.

Whenever attempting to accurately measure an oscillating signal, sampling must be performed at a sufficiently high rate. When the sampling rate is too low, the true frequency of oscillation may be underestimated, an effect known as aliasing. The general rule to avoid aliasing, as discussed in Section 5.2, is given by the Nyquist criterion. In parallel imaging the data are purposely undersampled to reduce examination duration, so aliasing is an impediment to the accurate reconstruction of the missing data. Aliasing was counteracted in this work by using a technique called CAIPIRINHA, discussed in detail in Section 6.4, which allows for the modification of aliasing conditions in a well-defined manner [298]. The downside of employing CAIPIRINHA is that it necessarily adds to the number of required data points for a given sampling scheme. This is due to the fact that the CAIPIRINHA sampling phase shift along a given dimension then necessitates the inclusion of autocalibration data at each line along the CAIPIRINHA-shifted dimension. To illustrate this with a concrete example, consider the two sampling schemes used in the prospectively undersampled experiments presented in Section 7.1.4. They both utilized a 10×10 autocalibration scheme, while one utilized a 2×2 acceleration scheme and the other used a 3×3 acceleration scheme, yielding effective acceleration factors of 2.50 and 3.58, respectively. However, if CAIPIRINHA were not employed, effective acceleration factors of 2.99 and 5.16 would have been achieved. Often this additionally sampled data necessitated by CAIPIRINHA is on the periphery of k-space and does not appreciably contribute to the fidelity of the reconstruction. It would be interesting to see how the badly the exclusion of CAIPIRINHA degrades reconstruction accuracy. It could be that although aliasing is more pronounced without CAIPIRINHA, the time saved via its exclusion allows for a less aggressive acceleration scheme which counteractively reduces aliasing. A more detailed analysis of the ultimate effect of CAIPIRINHA could prove fruitful.

The other consideration when discussing sampling patterns is whether Cartesian or elliptical patterns should be used. Elliptical sampling patterns excludes the periphery of k-space in, as the name suggests, an elliptical pattern. The logic is that the periphery of k-space contains less useful information than its center, so by acquiring data in an elliptical fashion, examination acquisition duration is reduced without greatly affecting image quality. This is a standard option on most scanners and is often utilized in the field, so its incorporation was considered in this work. However, initial experiments not presented here demonstrated that nothing is gained by incorporating an elliptical acquisition. In particular, consider the sampling pattern utilizing a 12×12 autocalibration scheme and 3×3 acceleration scheme, yielding an effective acceleration factor of 3.23. By changing the Cartesian acquisition into an elliptical acquisition, and effective acceleration factor of 3.52 could be achieved. However, this produced slightly less accurate results than the Cartesian sampling scheme with an effective acceleration factor of 3.58. This observation was also corroborated in other examples, so it seems that nothing is gained by going to an elliptical acquisition, as the additional acceleration can be just as accurately achieved by simply transitioning to a more aggressive Cartesian acquisition.

In summary, the ARTT GRAPPA approach allows for much greater flexibility in sampling patterns. In any parallel imaging approach, there is always a delicate balance between minimizing examination acquisition duration while still accurately recapitulating the object being imaged, and ARTT GRAPPA brings these considerations to the forefront, since many more potential sampling schemes are possible. Although thoughtful consideration was taken in choosing appropriate sampling patterns, a more detailed optimization of the sampling scheme may be beneficial and allow for a more optimal

trade off between scan time and reconstruction accuracy.

8.2.4 Other Notable Approaches in the Literature

In 2017, Gruber et al. [50] utilized an innovative parallel imaging-based technique to accelerate the acquisition of high-resolution MRSI datasets. In short, a gradient echo prescan was acquired prior to the MRSI acquisition and subsequently used in the determination of the coil weighting factors. The parallel imaging reconstruction was then performed in k-space, and high-resolution metabolite maps of the human brain with an imaging matrix size of 64×64 and a sub-five mm resolution were acquired in six minutes. While the technique describes itself as GRAPPA, according to the discussion in Section 8.2.1, it is seen to be more SENSE-like than GRAPPA-like. The distinguishing feature of GRAPPA is that the coil weighting factors are acquired via autocalibration, while in SENSE, a prescan is required. Whether the reconstruction is performed in k-space or image space is immaterial by the arguments given above.

The Gruber et al. approach [50] accelerates more aggressively than the ARTT GRAPPA approach and achieves an effective acceleration of 5.0 as compared to an effective acceleration of 3.58. However, there is an important limitation to this approach which allows the ARTT GRAPPA approach to retain its value. Namely, as mentioned above, the Gruber et al. approach [50] requires the acquisition of a SENSE-like prescan in the determination of the coil weights. This feature makes it difficult to apply this technique to nuclei other than protons. X-nuclei imaging with nuclei such as ^{31}P and ^{13}C is plagued with very much lower sensitivities compared to ^{1}H imaging, so this technique would not be appropriate in these settings. The ARTT GRAPPA approach, however, acquires the coil weights via proper autocalibration, and, thus, this approach can be easily translated to ^{31}P MRSI or ^{13}C MRSI. Also, the Gruber et al. approach [50], like all SENSE-like parallel imaging techniques using a prescan, is sensitive to patient motion in the time between the prescan and data acquisition. The ARTT GRAPPA approach, again due to its use of proper autocalibration, is less sensitive to patient motion. It is these advantages of ARTT GRAPPA which will make its application useful to the MRSI community and provide X-nuclei spectroscopic imaging a viable parallel imaging alternative that does not require the acquisition of calibration scans prior to spectroscopic imaging acquisition.

8.3 Future Applications

8.3.1 Cancer Imaging

As discussed in Section 3.1, tumorous tissue exhibits dysregulated metabolic activity. This is considered one of the fundamental hallmarks of cancer. Namely, tumor cells, even in presence of an ample supply of oxygen, preferentially undergo glycolysis. Some of the metabolites commonly observed in ^{1}H spectroscopy are known to have altered concentrations in cancerous cells, so observing how these concentrations change is very important. Most notably, NAA levels are known to decrease specifically in gliomas [131], and choline levels are known to increase in tumors [145]. The technique presented in this work has the ability to noninvasively produce high-resolution choline and NAA maps. Thus, one can interrogate changes in choline and NAA concentration levels in a spatially localized manner. This technique can aid in cancer diagnosis, but its main strength lies in its ability to monitor therapeutic response. Since MRSI does not use ionizing radiation, this technique can be applied serially to observe how metabolism changes throughout a course of treatment. Metabolism is downstream from

genomics, transcriptomics, and proteomics, so observing tumor metabolism provides crucial insight into the biological processes underlying tumor progression and therapeutic response.

In a recent study carried out by other members of Professor Bachert's laboratory, Meißner et al. [357] used single-voxel proton spectroscopy to observe longitudinal changes in choline-to-NAA ratios of a number of glioma patients as they underwent chemoradiotherapy. Scans were performed at three timepoints: before treatment, immediately following treatment, and six weeks after treatment. It was observed that choline-to-NAA ratios decreased in those patients that responded to therapy but stayed roughly constant in non-responders. The technique presented in this work would surely add value to such a study due to the heterogeneous nature of tumors. The single-voxel spectroscopy in this study observed ratiometric changes in a large voxel of $2 \times 2 \times 2$ cm^3, but it would have been advantageous to observe smaller scale changes with an in-plane resolution less than 4×4 mm^2. Since ^{1}H MRSI datasets can now be acquired in less than 20 minutes, it is now feasible to include this protocol as part of larger studies attempting to predict therapeutic response.

8.3.2 X-Nuclei Spectroscopy

A major potential application of this technique is the acceleration of X-nuclei spectroscopic imaging. SENSE-like techniques are not ideal for X-nuclei spectroscopic imaging since they explicitly require the acquisition of coil sensitivity maps. These are often difficult or not possible to acquire using nuclei other than protons. Even if they are able to be acquired, the SNR of these maps would be quite low which renders the determination of the coil weights and subsequent reconstruction process unreliable. The technique presented here, on the other hand, determines the coil weighting factors directly from the MRSI data, so no prescan is required. This will make this approach very amenable to X-nuclei applications. The improvement of this technique relative to conventional MRSI GRAPPA will allow for more aggressive X-nuclei MRSI sampling schemes, which can then be traded for more averages in order to increase SNR.

In particular, two specific X-nuclei spectroscopy applications come to mind: ^{31}P MRSI and hyperpolarized ^{13}C MRSI. Members of the laboratory recently published a study that uses ^{31}P MRSI to volumetrically map intracellular and extracellular pH in glioma patients [358]. In an oncological setting, pH is quite important since intracellular pH increases in tumors relative to healthy tissue, while extracellular pH decreases in tumors. In addition to pH, ^{31}P MRSI is able to interrogate energy metabolism and phospholipid turnover. The implementation of ARTT GRAPPA into this protocol would be highly beneficial. As with most X-nuclei, ^{31}P MRSI has low intrinsic sensitivity in the human brain, so multiple averages are typically required which add to the overall scan time and partially prohibit the acquisition of large image matrix sizes. The implementation of this ARTT GRAPPA algorithm would allow for the acquistion duration to be reduced which could then be traded for more averages and ultimately be used to improve the sensitivity of the technique.

The other major X-nuclei spectroscopy application is hyperpolarized ^{13}C MRSI. The German Cancer Research Center recently installed a device that can improve the sensitivity of ^{13}C applications by four orders of magnitude by driving spins into a specified energy state by transferring polarization from free electrons to nuclei via microwave irradiation at low temperatures [359]. The hyperpolarized nucleus which is conjugated to some biomolecule, such as pyruvate, is injected into the patient and

the metabolic evolution of that molecule can be followed dynamically. Since the T_1 relaxation time of ^{13}C-conjugated pyruvate is on the order of tens of seconds, the hyperpolarized signal only lasts for a short time. This technical limitation necessitates fast imaging sequences, so this ARTT GRAPPA algorithm is well suited to be utilized in this application as well.

Chapter 9

Summary

Proton magnetic resonance spectroscopic imaging provides the means to noninvasively interrogate metabolism *in vivo*. However, despite tremendous potential it has failed to be adopted into routine clinical practice in part due to the excessively long amount of time required for a ^{1}H MRSI examination. In this work, a novel parallel imaging algorithm was developed and an accelerated high-resolution ^{1}H MRSI protocol was established.

In order to construct this protocol six main components were realized. A pulse sequence was created that directly acquires an FID at various locations in k-space. This pulse sequence collects data in an ARTT GRAPPA-based sampling pattern, and these locations are offset in a CAIPIRINHA-like scheme in order to minimize the effects of aliasing. Prior to data acquisition seven CHESS pulses with varying amplitudes and interpulse delays were applied. This VAPOR implementation succeeds in suppressing the large water signal by many orders of magnitude so that it is comparable to the metabolite resonances. A novel ARTT GRAPPA reconstruction algorithm was developed which allows for an over three-fold acceleration of the image acquisition. The appropriate GRAPPA reconstruction parameters were determined via a number of simulation studies. A multi-voxel coil combination that is based on singular value decomposition was achieved in order to combine the data acquired in each individual coil element. An L_2 regularization algorithm was implemented which removes the lipid signal that contaminates the brain spectra. This signal arises from the pericranial lipids surrounding the skull and bleeds into adjacent voxels but is completely eliminated via L_2 regularization. The final component of this protocol was to incorporate the software LCModel which allows for the quantification of the proton spectra.

The main novelty of this work was the development of the ARTT GRAPPA reconstruction algorithm. The defining feature of GRAPPA is that the coil weights used in the reconstruction process are not explicitly measured but instead implicitly determined via the full acquisition of a central autocalibration region. Conventionally this autocalibration region extends along one of the k-space directions which prohibits undersampling along that dimension. In MRSI, an FID is acquired at each sampled position in k-space, so the autocalibration region can instead be taken to extend along the temporal dimension. This ARTT GRAPPA approach determines the coil weights using an autocalibration region in k-t-space which allows for a greater flexibility in sampling schemes since one is no longer forced to fully sample one of the k-space direction. This work exhibits the feasibility of this ARTT GRAPPA approach demonstrating that the coil weights can be determined using time domain data.

In addition to the feasibility of this approach it is also shown that ARTT GRAPPA performs markedly better than the conventional approach. In particular, ARTT GRAPPA allows for approximately twice as much acceleration than conventional MRSI GRAPPA for the same level of reconstruction accuracy. This was demonstrated *in vivo* using a fully sampled MRSI dataset of a healthy volunteer's brain via a retrospective undersampling analysis. The ARTT GRAPPA reconstruction algorithm is demonstrated to be more accurate than a conventional MRSI GRAPPA reconstruction algorithm, and this superior accuracy can be traded to more aggressively accelerate the image acquisition or to reconstruct lower SNR datasets.

The hypothesized reason why ARTT GRAPPA performs better than conventional MRSI GRAPPA is that ARTT GRAPPA exploits the spatial-spectral correlations in the data. Data suggesting this were presented since the same analysis performed on a homogeneous phantom, where there are no spatial-spectral correlations to exploit, showed no benefit to using ARTT GRAPPA. It is only when spatial-spectral correlations are available in the data to exploit, which is surely the case for *in vivo* applications, does the use of ARTT GRAPPA become beneficial.

This protocol was then applied to acquire prospectively undersampled MRSI data and produce high-resolution metabolite maps of NAA, choline, and creatine in three healthy volunteers, achieving an in-plane resolution of 3.75 mm. Two undersampling schemes were employed: an effective acceleration of 2.50 acquired in 25 minutes and an effective acceleration of 3.58 acquired in 17 minutes. This is in comparison to the 62 minutes that such an examination would have taken without the implementation of parallel imaging. Thus, it is demonstrated that accurate, high-resolution proton spectroscopic imaging is possible in less than twenty minutes which greatly increases this technique's clinical feasibility.

This accelerated ^{1}H MRSI protocol is now in place and can be utilized in the future to interrogate neurometabolism in a number of pathologies. In particular, metabolism is severely dysregulated in cancerous tissue, so this technique is well-suited to interrogate malignant systems. Often in oncology, it is not known *a priori* whether a patient will respond to a given treatment. Therefore, this protocol would be useful in serially monitoring tumor metabolism and assessing therapeutic response. In addition, because the ARTT GRAPPA approach is a fully autocalibrating parallel imaging approach, it is readily translatable into MRSI applications targeting nuclei other than protons. Future applications include the implementation of ARTT GRAPPA into ^{31}P MRSI which can image tumor pH and interrogate energy metabolism and dynamic ^{13}C MRSI which observes metabolic transitions in real time.

Chapter 10

Appendix

R_{eff}	C[tCho] / C[tCr])	CRLB (%)	Tube
Fully Sampled	0.037 ± 0.020	372 ± 479	1
2.50	0.040 ± 0.022	414 ± 488	1
2.89	0.044 ± 0.030	411 ± 490	1
3.23	0.045 ± 0.034	528 ± 500	1
3.75	0.032 ± 0.017	546 ± 484	1
4.04	0.039 ± 0.025	414 ± 487	1
4.33	0.049 ± 0.037	688 ± 462	1
4.71	0.036 ± 0.025	537 ± 491	1
Fully Sampled	2.17 ± 0.16	2.6 ± 0.5	2
2.50	2.16 ± 0.16	2.6 ± 0.6	2
2.89	2.18 ± 0.16	2.6 ± 0.5	2
3.23	2.18 ± 0.17	2.6 ± 0.5	2
3.75	2.18 ± 0.16	2.6 ± 0.5	2
4.04	2.17 ± 0.16	2.6 ± 0.5	2
4.33	2.19 ± 0.16	2.8 ± 0.4	2
4.71	2.17 ± 0.16	2.7 ± 0.5	2
Fully Sampled	0.019 ± 0.010	764 ± 387	3
2.50	0.015 ± 0.012	691 ± 395	3
2.89	0.018 ± 0.013	751 ± 385	3
3.23	0.027 ± 0.017	271 ± 316	3
3.75	0.020 ± 0.018	321 ± 298	3
4.04	0.030 ± 0.011	467 ± 447	3
4.33	0.024 ± 0.020	310 ± 327	3
4.71	0.022 ± 0.018	403 ± 375	3
Fully Sampled	0.028 ± 0.022	457 ± 491	4
2.50	0.021 ± 0.018	377 ± 444	4
2.89	0.022 ± 0.020	437 ± 473	4
3.23	0.022 ± 0.014	576 ± 488	4
3.75	0.021 ± 0.014	439 ± 473	4
4.04	0.048 ± 0.043	393 ± 471	4
4.33	0.036 ± 0.024	378 ± 476	4
4.71	0.059 ± 0.046	301 ± 445	4

Table 10.1: The variation of local choline concentration across the four test tubes - Concentrations are expressed relative to the total creatine concentration, and CRLB's are listed as percentages. Choline is only present in tube 2.

R_{eff}	C[Lac] / C[tCr])	CRLB (%)	Tube
Fully Sampled	0.007 ± 0.006	763 ± 333	1
2.50	0.008 ± 0.006	880 ± 278	1
2.89	0.006 ± 0.006	773 ± 289	1
3.23	0.006 ± 0.006	808 ± 301	1
3.75	0.009 ± 0.006	753 ± 355	1
4.04	0.006 ± 0.004	785 ± 323	1
4.33	0.003 ± 0.003	918 ± 201	1
4.71	0.002 ± 0.001	944 ± 410	1
Fully Sampled	0.018 ± 0.015	848 ± 259	2
2.50	0.021 ± 0.015	864 ± 246	2
2.89	0.015 ± 0.014	886 ± 238	2
3.23	0.022 ± 0.017	844 ± 278	2
3.75	0.022 ± 0.014	822 ± 275	2
4.04	0.029 ± 0.021	785 ± 308	2
4.33	0.021 ± 0.011	818 ± 266	2
4.71	0.029 ± 0.023	831 ± 289	2
Fully Sampled	0.069 ± 0.022	765 ± 384	3
2.50	0.057 ± 0.040	777 ± 369	3
2.89	0.075 ± 0.033	798 ± 366	3
3.23	0.063 ± 0.046	575 ± 427	3
3.75	0.061 ± 0.049	571 ± 420	3
4.04	0.079 ± 0.051	630 ± 429	3
4.33	0.064 ± 0.054	552 ± 408	3
4.71	0.077 ± 0.042	477 ± 412	3
Fully Sampled	2.71 ± 0.64	8.4 ± 2.7	4
2.50	2.46 ± 0.67	8.5 ± 2.8	4
2.89	2.31 ± 0.71	6.4 ± 2.2	4
3.23	3.04 ± 0.39	1.9 ± 1.6	4
3.75	2.91 ± 0.46	3.0 ± 2.1	4
4.04	2.65 ± 0.64	12.5 ± 4.3	4
4.33	2.98 ± 0.45	2.2 ± 1.3	4
4.71	2.99 ± 0.42	3.2 ± 1.8	4

Table 10.2: The variation of local lactate concentration across the four test tubes - Concentrations are expressed relative to the total creatine concentration, and CRLB's are listed as percentages. Lactate is only present in tube 4.

R_{eff}	C[NAA] (mM)	CRLB (%)	Tube
Fully Sampled	3.1 ± 2.0	320 ± 437	1
2.50	3.0 ± 1.9	285 ± 416	1
2.89	2.3 ± 1.9	255 ± 358	1
3.23	3.0 ± 1.8	191 ± 360	1
3.75	2.1 ± 1.4	260 ± 381	1
4.04	2.5 ± 1.6	497 ± 465	1
4.33	2.5 ± 2.1	148 ± 265	1
4.71	1.8 ± 1.5	376 ± 414	1
Fully Sampled	1.6 ± 0.6	596 ± 310	2
2.50	1.5 ± 0.8	421 ± 242	2
2.89	1.2 ± 0.9	572 ± 315	2
3.23	2.1 ± 1.1	282 ± 178	2
3.75	1.7 ± 1.0	384 ± 217	2
4.04	1.8 ± 1.3	460 ± 314	2
4.33	2.2 ± 1.3	330 ± 257	2
4.71	2.1 ± 0.9	319 ± 222	2
Fully Sampled	103.6 ± 10.2	4.8 ± 1.2	3
2.50	102.6 ± 9.1	4.8 ± 1.2	3
2.89	102.6 ± 9.3	4.9 ± 1.3	3
3.23	112.4 ± 8.8	4.3 ± 1.1	3
3.75	112.0 ± 8.7	4.3 ± 1.1	3
4.04	106.4 ± 8.7	4.6 ± 1.2	3
4.33	111.3 ± 9.0	4.3 ± 1.1	3
4.71	110.3 ± 8.4	4.3 ± 1.1	3
Fully Sampled	0.6 ± 0.5	701 ± 414	4
2.50	0.4 ± 0.4	601 ± 393	4
2.89	0.7 ± 0.7	758 ± 378	4
3.23	1.7 ± 1.2	295 ± 407	4
3.75	1.4 ± 1.5	430 ± 420	4
4.04	0.9 ± 0.5	574 ± 428	4
4.33	1.5 ± 1.8	340 ± 430	4
4.71	1.9 ± 1.7	252 ± 350	4

Table 10.3: The variation of local NAA concentration across the four test tubes - Concentrations are expressed in mM, and CRLB's are listed as percentages. NAA is only present in tube 3. Here, NAA is shown in absolute concentrations since there is no creatine present in tube 3.

R_{eff}	C[tCr] (mM)	CRLB (%)	Tube
Fully Sampled	46.4 ± 2.3	1.7 ± 0.7	1
2.50	46.3 ± 2.0	1.7 ± 0.5	1
2.89	46.6 ± 2.3	1.6 ± 0.6	1
3.23	45.8 ± 2.3	1.9 ± 0.6	1
3.75	45.3 ± 2.2	1.8 ± 0.7	1
4.04	46.3 ± 2.2	2.0 ± 0.5	1
4.33	45.3 ± 2.4	2.1 ± 0.6	1
4.71	46.0 ± 2.6	1.8 ± 0.5	1
Fully Sampled	38.7 ± 7.4	7.5 ± 0.9	2
2.50	38.5 ± 7.4	7.6 ± 0.9	2
2.89	38.9 ± 7.1	7.6 ± 1.0	2
3.23	38.1 ± 8.4	7.8 ± 1.2	2
3.75	37.8 ± 7.7	7.9 ± 1.2	2
4.04	38.2 ± 7.5	7.7 ± 1.5	2
4.33	38.6 ± 8.6	7.9 ± 1.2	2
4.71	38.1 ± 7.5	8.0 ± 1.3	2
Fully Sampled	4.1 ± 3.5	619 ± 399	3
2.50	3.9 ± 3.4	585 ± 364	3
2.89	4.1 ± 3.1	624 ± 396	3
3.23	3.2 ± 3.1	466 ± 297	3
3.75	3.9 ± 3.9	705 ± 443	3
4.04	3.7 ± 3.3	742 ± 460	3
4.33	3.4 ± 3.1	538 ± 324	3
4.71	3.6 ± 3.5	556 ± 321	3
Fully Sampled	32.7 ± 14.1	5.0 ± 3.3	4
2.50	29.0 ± 16.2	6.4 ± 3.1	4
2.89	28.3 ± 16.7	6.0 ± 3.6	4
3.23	36.7 ± 9.0	2.3 ± 1.8	4
3.75	35.1 ± 11.0	3.3 ± 2.1	4
4.04	31.6 ± 15.5	4.6 ± 2.9	4
4.33	35.8 ± 10.7	2.4 ± 1.4	4
4.71	36.7 ± 10.4	8.6 ± 4.0	4

Table 10.4: The variation of local creatine concentration across the four test tubes - Concentrations are expressed in mM, and CRLB's are listed as percentages. Creatine is present in tubes 1, 2, and 4.

R_{eff}	C[tCho] / C[tCr]) (mM)	CRLB (%)	Region
Fully Sampled	0.405 ± 0.104	9.8 ± 0.8	ROI 1
2.50	0.414 ± 0.108	11.1 ± 1.0	ROI 1
3.23	0.395 ± 0.092	11.8 ± 0.9	ROI 1
3.58	0.375 ± 0.119	15.3 ± 1.3	ROI 1
3.75	0.384 ± 0.100	13.7 ± 1.6	ROI 1
4.04	0.371 ± 0.084	13.6 ± 1.8	ROI 1
Fully Sampled	0.280 ± 0.037	7.4 ± 3.6	ROI 2
2.50	0.276 ± 0.033	10.6 ± 4.5	ROI 2
3.23	0.282 ± 0.035	12.6 ± 7.2	ROI 2
3.58	0.273 ± 0.051	13.8 ± 5.5	ROI 2
3.75	0.238 ± 0.036	13.6 ± 5.9	ROI 2
4.04	0.268 ± 0.060	8.3 ± 6.1	ROI 2

Table 10.5: The variation of local choline concentration in ROI 1 and ROI 2 of the brain of a healthy volunteer - Concentrations are expressed relative to the total creatine concentration, and CRLB's are listed as percentages.

R_{eff}	C[tNAA] / C[tCr]) (mM)	CRLB (%)	Region
Fully Sampled	1.908 ± 0.153	6.6 ± 0.5	ROI 1
2.50	1.964 ± 0.165	7.4 ± 0.5	ROI 1
3.23	1.929 ± 0.150	7.6 ± 0.5	ROI 1
3.58	1.986 ± 0.183	9.0 ± 1.2	ROI 1
3.75	2.035 ± 0.232	8.0 ± 0.4	ROI 1
4.04	2.029 ± 0.198	8.4 ± 0.6	ROI 1
Fully Sampled	1.786 ± 0.183	4.5 ± 1.5	ROI 2
2.50	1.768 ± 0.135	5.7 ± 1.8	ROI 2
3.23	1.809 ± 0.258	6.2 ± 2.3	ROI 2
3.58	1.799 ± 0.232	5.7 ± 2.7	ROI 2
3.75	1.793 ± 0.282	5.5 ± 2.9	ROI 2
4.04	1.776 ± 0.446	6.8 ± 3.3	ROI 2

Table 10.6: The variation of local NAA concentration in ROI 1 and ROI 2 of the brain of a healthy volunteer - Concentrations are expressed relative to the total creatine concentration, and CRLB's are listed as percentages.

R_{eff}	C[Glx] / C[tCr]) (mM)	CRLB (%)	Region
Fully Sampled	0.500 ± 0.085	4.0 ± 0.9	ROI 1
2.50	0.533 ± 0.069	3.9 ± 0.6	ROI 1
3.23	0.508 ± 0.060	5.6 ± 1.6	ROI 1
3.58	0.561 ± 0.081	8.1 ± 3.5	ROI 1
3.75	0.478 ± 0.093	12.8 ± 3.8	ROI 1
4.04	0.446 ± 0.072	7.8 ± 1.8	ROI 1
Fully Sampled	0.436 ± 0.124	7.3 ± 1.4	ROI 2
2.50	0.465 ± 0.118	5.6 ± 1.1	ROI 2
3.23	0.484 ± 0.154	12.8 ± 1.8	ROI 2
3.58	0.498 ± 0.211	9.2 ± 1.1	ROI 2
3.75	0.398 ± 0.130	12.8 ± 1.2	ROI 2
4.04	0.474 ± 0.145	12.6 ± 2.3	ROI 2

Table 10.7: The variation of local Glx concentration in ROI 1 and ROI 2 of the brain of a healthy volunteer - Concentrations are expressed relative to the total creatine concentration, and CRLB's are listed as percentages.

R_{eff}	C[tCr] (mM) (mM)	CRLB (%)	Region
Fully Sampled	5.60 ± 0.66	5.3 ± 1.1	ROI 1
2.50	5.38 ± 0.69	6.1 ± 1.2	ROI 1
3.23	5.88 ± 0.65	6.3 ± 1.0	ROI 1
3.58	5.11 ± 0.74	8.6 ± 1.9	ROI 1
3.75	5.64 ± 0.77	6.8 ± 1.3	ROI 1
4.04	5.75 ± 0.70	6.2 ± 1.1	ROI 1
Fully Sampled	4.60 ± 0.58	4.9 ± 0.8	ROI 2
2.50	4.44 ± 0.58	4.7 ± 0.6	ROI 2
3.23	4.32 ± 0.61	5.2 ± 0.9	ROI 2
3.58	4.43 ± 0.86	5.8 ± 1.2	ROI 2
3.75	4.30 ± 0.66	7.3 ± 1.2	ROI 2
4.04	4.46 ± 0.78	9.1 ± 1.8	ROI 2

Table 10.8: The variation of local creatine concentration in ROI 1 and ROI 2 of the brain of a healthy volunteer - Concentrations are expressed in mM, and CRLB's are listed as percentages.

Bibliography

[1] Planck M. Zur Theorie des Gesetzes der Energieverteilung im Normalspektrum. *Verhandlungen der Deutschen Physikalischen Gesellschaft*. 1900; 2: 237-245.

[2] Rayleigh L. The law of partition of kinetic energy. *The London, Edinburgh, and Dublin Philosophical Magazine and Journal of Science*. 1900; 49(296): 98-118.

[3] Jeans JH. On the partition of energy between matter and aether. *The London, Edinburgh, and Dublin Philosophical Magazine and Journal of Science*. 1900; 49(296): 98-118.

[4] Jeans JH. A comparison between two theories of radiation. *Nature*. 1905; 72: 293-294.

[5] Boltzmann L. Über die Natur der Gasmoleküle. *Wiener Berichte*. 1876; 74: 553-560.

[6] Eisberg R, Resnick R. *Quantum Physics of Atoms, Molecules, Solids, Nuclei, and Particles, 2nd Edition*. 1985; New York: John Wiley & Sons, Inc.

[7] Einstein A. Über einen die Erzeugung und Verwandlung des Lichtes betreffenden heuristischen Gesichtspunkt. *Annalen der Physik*. 1905; 322(6): 132-148.

[8] Lenard P. Über die lichtelektrische Wirkung. *Annalen der Physik*. 1902; 313(5): 149-198.

[9] Compton AH. A quantum theory of the scattering of X-rays by light elements. *Physical Review*. 1923; 21(5): 483-502.

[10] De Broglie L. Waves and quanta. *Nature*. 1923; 112(2815): 540.

[11] Pauli W. Über den Zusammenhang des Abschlusses der Elektronengruppen im Atom mit der Komplexstruktur der Spektren. *Zeitschrift für Physik*. 1925; 31(1): 765-783.

[12] Heisenberg W. Über den anschaulichen Inhalt der quantentheoretischen Kinematik und Mechanik. *Zeitschrift für Physik*. 1927; 43(3-4): 172-198.

[13] Schrödinger E. An undulatory theory of the mechanics of atoms and molecules. *Physical Review*. 1926; 28(6): 1049-1070.

[14] Thomson JJ. Cathode rays. *The London, Edinburgh, and Dublin Philosophical Magazine and Journal of Science*. 1897; 44(269): 293-316.

[15] Thomson JJ. On the structure of the atom: An investigation of the stability and periods of oscillation of a number of corpuscles arranged at equal intervals around the circumference of a circle; with application of the results to the theory of atomic structure. *The London, Edinburgh, and Dublin Philosophical Magazine and Journal of Science*. 1904; 7(39): 237-265.

[16] Rutherford E. The scattering of α and β particles by matter and the structure of the atom. *The London, Edinburgh, and Dublin Philosophical Magazine and Journal of Science*. 1911; 21(125): 669-688.

[17] Geiger H, Marsden E. On a diffuse reflection of the α-particles. *Proceedings of the Royal Society of London, Series A*. 1909; 82(557): 495-500.

[18] Bohr N. On the Constitution of Atoms and Molecules, Part I. *The London, Edinburgh, and Dublin Philosophical Magazine and Journal of Science*. 1913; 26(151): 1-24.

[19] Langmuir I. The structure of the helium atom. *Physical Review*. 1921; 17(3): 339.

[20] Sommerfeld A. Zur Quantentheorie der Spektrallinien. *Annalen der Physik*. 1916; 356(17): 1-94.

[21] Gerlach W, Stern O. Der experimentelle Nachweis der Richtungsquantelung im Magnetfeld. *Zeitschrift für Physik*. 1922; 9(1): 349-352.

[22] Dirac PAM. The quantum theory of the electron. *Proceedings of the Royal Society of London, Series A*. 1928; 117(778): 610-624.

[23] Rabi II, Zacharias JR, Millman S, Kusch P. A new method of measuring nuclear magnetic moment. *Physical Review*. 1938; 53(4): 318.

[24] Purcell EM, Torrey HC, Pound RV. Resonance absorption by nuclear magnetic moments in a solid. *Physical Review*. 1946; 69(1-2): 37-38.

[25] Bloch F. Nuclear induction. *Physical Review*. 1946; 70(7-8): 460-474.

[26] Hahn EL. Spin echoes. *Physical Review*. 1950; 80(4): 580-594.

[27] Ernst RE, Anderson WA. Application of Fourier transform spectroscopy to magnetic resonance. *Review of Scientific Instruments*. 1966; 37(1): 93-102.

[28] Odeblad E, Lindström G. Some preliminary observations on the proton magnetic resonance in biologic samples. *Acta Radiologica*. 1955; 6: 469-76.

[29] Rinck PA. *Magnetic Resonance in Medicine: A Critical Introduction*. 2019; Freiburg, Germany: Books on Demand.

[30] Lignon TR. *Coil design for low field NMR and NMR measurements on the human arm*. Ph.D. Thesis. Oklahoma State University. 1967.

[31] Jackson JA, Langham WH. Whole-body NMR spectrometer. *Review of Scientific Instruments*. 1968; 39(4): 510-513.

[32] Damadian R. Tumor detection by nuclear magnetic resonance. *Science*. 1971; 171(3976): 1151-1153.

[33] Hollis DP. *Abusing Cancer Science: The Truth about NMR and Cancer*. 1987; Chehalis, Washington: The Strawberry Fields Press.

[34] Lauterbur PC. Image formation by induced local interactions: Examples employing nuclear magnetic resonance. *Nature*. 1973; 242(5394): 190-191.

[35] Lauterbur PC, Lai CM. Zeugmatography by reconstruction from projections. *IEEE Transactions on Nuclear Science*. 1980; 27(3): 1227-1231.

[36] Lauterbur PC. Magnetic resonance zeugmatography. *Pure and Applied Chemistry*. 1974; 40(1-2): 149-157.

[37] Bernardo Jr ML, Cohen AJ, Lauterbur PC. Radiofrequency coil designs for nuclear magnetic resonance zeugmatographic imaging. *IEEE Physics and Engineering in Medical Imaging*. 1982; 372: 277-284.

[38] Rinck PA, Petersen SB, Heidelberger E, Acuff V, Reinders J, Bernardo ML, Hedges LK, Lauterbur PC. NMR ventilation imaging of the lungs using perfluorinated gases. *Magnetic Resonance in Medicine*. 1984; 1(2): 237.

[39] Frank JA, Feiler MA, House WV, Lauterbur PC, Jacobson MJ. Measurement of proton nuclear magnetic longitudinal relaxation times and water content in infarcted myocardium and induced pulmonary injury. *Clinical Research*. 1976; 24: 217A.

[40] Muller RN, Marsh MJ, Bernardo ML, Lauterbur PC. True 3-D imaging of limbs by NMR zeugmatography with off-resonance irradiation. *European Journal of Radiology*. 1983; 3: 286-290.

[41] Lauterbur PC, Kramer DM, House Jr WV, Chen CN. Zeugmatographic high resolution nuclear magnetic resonance spectroscopy: Images of chemical inhomogeneity within macroscopic objects. *Journal of the American Chemical Society*. 1975; 97(23): 6866-6868.

[42] Mansfield P. Multi-planar image formation using NMR spin echoes. *Journal of Physics C: Solid State Physics*. 1977; 10: L55-L58.

[43] Ordidge RJ, Mansfield P, Coupland RE. Rapid biomedical imaging by NMR. *The British Journal of Radiology*. 1981; 54(646): 850-855.

[44] Hounsfield GN. Computerized transverse axial scanning (tomography): Part 1. Description of system. *The British Journal of Radiology*. 1973; 46(552): 1016-1022.

[45] Wang J, Weygand J, Hwang KP, Mohamed ASR, Ding Y, Fuller CD, Lai SY, Frank SJ, Zhou J. Magnetic resonance imaging of glucose uptake and metabolism in patients with head and neck cancer. *Scientific Reports*. 2016; 6(1): 1-7.

[46] Warburg O. The metabolism of carcinoma cells. *The Journal of Cancer Research*. 1925; 9(1): 148-163.

[47] Sullivan LB, Gui DY, Vander Heiden MG. Altered metabolite levels in cancer: implications for tumour biology and cancer therapy. *Nature Reviews Cancer*. 2016; 16(11): 680-693.

[48] Kelloff GJ, Sigman CC. Cancer biomarkers: Selecting the right drug for the right patient. *Nature Reviews Drug Discovery*. 2012; 11(3): 201-214.

[49] Winfield JM, Payne GS, Weller A, deSouza NM. DCE-MRI, DW-MRI, and MRS in cancer: Challenges and advantages of implementing qualitative and quantitative multi-parametric imaging in the clinic. *Topics in Magnetic Resonance Imaging*. 2016; 25(5): 245.

[50] Gruber S, Heckova E, Strasser B, Považan M, Hangel GJ, Minarikova L, Trattnig S, Bogner W. Mapping an extended neurochemical profile at 3 and 7 T using accelerated high-resolution proton magnetic resonance spectroscopic imaging. *Investigative Radiology*. 2017; 52(10): 631-639.

[51] Heidemann RM, Özsarlak Ö, Parizel PM, Michiels J, Kiefer B, Jellus V, Müller M, Breuer F, Blaimer M, Griswold MA, Jakob PM. A brief review of parallel magnetic resonance imaging. *European Radiology*. 2003; 13(10): 2323-2337.

[52] Brau ACS, Beatty PJ, Skare S, Bammer R. Comparison of reconstruction accuracy and efficiency among autocalibrating data-driven parallel imaging methods. *Magnetic Resonance in Medicine*. 2008; 59(2): 382-395.

[53] Ryder LH. Relativistic spin operator for Dirac particles. *General Relativity and Gravitation*. 1999; 31(5): 775-780.

[54] Thomson M. *Modern Particle Physics*. 2013; Cambridge, United Kingdom: Cambridge University Press.

[55] Scott GG. Review of gyromagnetic ratio experiments. *Reviews of Modern Physics*. 1962; 34(1): 102.

[56] Scaife BKP. *The Mathematical Papers of Sir William Rowan Hamilton*. 1931; Cambridge, United Kingdom: Cambridge University Press.

[57] Zeeman P. Over den invloed eener magnetisatie op den aard van het door een stof uitgezonden licht. *Koninklijke Akademie van Wetenschappen te Amsterdam*. 1896; 5: 181-184.

[58] Stark J. Beobachtungen über den Effekt des elektrischen Feldes auf Spektrallinien. I. Quereffekt. *Annalen der Physik*. 1914; 348(7): 965-982.

[59] Larmor J. On the theory of the magnetic influence on spectra; and on the radiation from moving ions. *The London, Edinburgh, and Dublin Philosophical Magazine and Journal of Science*. 1897; 44(271): 503-512.

[60] Gibbs JW. *Elementary Principles in Statistical Mechanics*. 1902; New York: Charles Scribner's Sons.

[61] De Graaf R. *In Vivo NMR Spectroscopy: Principles and Techniques*. 2007; Chichester, UK: John Wiley & Sons, Inc.

[62] Curie P. *Propriétés Magnétiques des Corps a Diverses Temperatures*. Ph.D. Thesis. University of Paris. 1895.

[63] Brown RW, Cheng YCN, Haacke EM, Thompson MR, Venkatesan R. *Magnetic Resonance Imaging: Physical Principles and Sequence Design*. 1999; Hoboken, New Jersey: John Wiley & Sons, Inc.

[64] Feynman RP, Vernon FL, Hellwarth RW. Geometrical representation of the Schrödinger equation for solving maser problems. *Journal of Applied Physics*. 1957; 28(1): 49-52.

[65] Benders S, Blümich B. Applications of magnetic resonance imaging in chemical engineering. *Physical Science Reviews*. 2019; 4(10): 1-17.

[66] Wang CH, Fleury PA. Raman Studies of Molecular Motion in Liquid and Solid HCl. *The Journal of Chemical Physics*. 1970; 53(6): 2243-2249.

[67] Levitt MH. *Spin Dynamics: Basics of Nuclear Magnetic Resonance*. 2008; Hoboken, New Jersey: John Wiley & Sons, Inc.

[68] Hendrick RE. Tissue relaxation. *Breast MRI: Fundamentals and Technical Aspects*. 2008; 2: 19-29.

[69] Chavhan GB, Babyn PS, Thomas B, Shroff MM, Haacke EM. Principles, techniques, and applications of T2*- based MR imaging and its special applications. *RadioGraphics*. 2009; 29(5): 1433-1449.

[70] Torrey HC. Bloch equations with diffusion terms. *Physical Review*. 1956; 104(3): 563-565.

[71] McConnell HM. Reaction rates by nuclear magnetic resonance. *The Journal of Chemical Physics*. 1958; 28(3): 430-431.

[72] Wilczek F. Magnetic flux, angular momentum and statistics. *Physical Review Letters*. 1982; 48(17): 1144.

[73] Jackson JD. *Classical Electrodynamics*. 1962; New York: John Wiley & Sons, Inc.

[74] Faraday M. Experimental researches in electricity. *Philosophical Transactions of the Royal Society of London*. 1832; 122: 125-162.

[75] Henry J. On the production of currents and sparks from electricity from magnetism. *The American Journal of Science and Arts*. 1832; 22: 402-408.

[76] Maxwell JC. A dynamical theory of the electromagnetic field. *Philosophical Transactions of the Royal Society of London*. 1865; 155: 459-512.

[77] Lorentz HA. Het theorema van Poynting over de energie in het electromagnetisch veld en een paar algemeene stellingen over de voortplanting van het licht. *Koninklijke Akademie van Wetenschappen te Amsterdam*. 1895; 4: 176-187.

[78] Carson JR. A generalization of the reciprocal theorem. *The Bell System Technical Journal*. 1924; 3(3): 393-399.

[79] Proctor WG, Yu FC. The dependence of a nuclear magnetic resonance frequency upon chemical compound. *Physical Review*. 1950; 77(5): 717.

[80] Hood MN, Ho VB, Smirniotopoulos JG, Szumowski J. Chemical shift: The artifact and clinical tool revisited. *RadioGraphics*. 1999; 19(2): 357-371.

[81] James TL. *Nuclear Magnetic Resonance in Biochemistry*. 1975; New York: Academic Press.

[82] Birchall T, Gillespie RJ. Nuclear magnetic resonance studies of the protonation of weak bases in fluorosulphuric acid II: Amides, thioamides, and sulphonamides. *Canadian Journal of Chemistry*. 1963; 41(10): 2642-2650.

[83] Babcock EE, Brateman L, Weinreb JC, Horner SD, Nunnally RL. Edge artifacts in MR images: Chemical shift effect. *Journal of Computer Assisted Tomography*. 1985; 9(2): 252-257.

[84] Howe FA, Maxwell RJ, Saunders DE, Brown MM, Griffiths JR. Proton spectroscopy in vivo. *Magnetic Resonance Quarterly*. 1993; 9(1): 31-59.

[85] Hollingworth W, Medina LS, Lenkinski RE, Shibata DK, Bernal B, Zurakowski D, Comstock B, Jarvik JG. A systematic literature review of magnetic resonance spectroscopy for the characterization of brain tumors. *American Journal of Neuroradiology*. 2006; 27(7): 1404-1411.

[86] Soares DP, Law M. Magnetic resonance spectroscopy of the brain: Review of metabolites and clinical applications. *Clinical Radiology*. 2009; 64(1): 12-21.

[87] Alger JR. Quantitative proton magnetic resonance spectroscopy and spectroscopic imaging of the brain: A didactic review. *Topics in Magnetic Resonance Imaging*. 2010; 21(2): 115.

[88] Loos C, Achten E, Santens P. Proton magnetic resonance spectroscopy in Alzheimer's disease, a review. *Acta Neurologica Belgica*. 2010; 110(4): 291-298.

[89] Weygand J, Carter SE, Salzillo TC, Moussalli M, Dai B, Dutta P, Zuo X, Fleming JB, Shureiqi I, Bhattacharya P. Can an Organoid Recapitulate the Metabolome of its Parent Tissue? A Pilot NMR Spectroscopy Study. *Journal of Cancer Prevention & Current Research*. 2017; 7: 00307.

[90] Kalra S. Magnetic resonance spectroscopy in ALS. *Frontiers in Neurology*. 2019; 10: 482.

[91] Rivenzon-Segal D, Margalit R, Degani H. Glycolysis as a metabolic marker in orthotopic breast cancer, monitored by in vivo 13C MRS. *American Journal of Physiology-Endocrinology and Metabolism*. 2002; 283(4): E623-E630.

[92] Morris P, Bachelard H. Reflections on the application of 13C-MRS to research on brain metabolism. *NMR in Biomedicine*. 2003; 16(6):303-312.

[93] Ross B, Lin A, Harris K, Bhattacharya P, Schweinsburg B. Clinical experience with 13C MRS in vivo. *NMR in Biomedicine*. 2003; 16(6): 358-369.

[94] Salzillo TC, Hu J, Nguyen L, Whiting N, Lee J, Weygand J, Dutta P, Pudakalakatti S, Millward NZ, Gammon ST, Lang FF. Interrogating metabolism in brain cancer. *Magnetic Resonance Imaging Clinics*. 2016; 24(4): 687-703.

[95] Weygand J. *Identifying the immune related metabolic properties of pancreatic cancer using nuclear magnetic resonance spectroscopy and dynamic magnetic resonance spectroscopic imaging with hyperpolarized pyruvate*. SMS Thesis. UTGSBS Dissertations. 2017.

[96] Dutta P, Perez MR, Lee J, Kang Y, Pratt M, Salzillo TC, Weygand J, Zacharias NM, Gammon ST, Koay EJ, Kim M, McAllister F, Sen S, Maitra A, Piwnica-Worms D, Fleming JB, Bhattacharya PK. Combining hyperpolarized real-time metabolic imaging and NMR spectroscopy to identify metabolic biomarkers in pancreatic cancer. *Journal of Proteome Research*. 2019; 18(7): 2826-2834.

[97] Rothman DL, de Graaf RA, Hyder F, Mason GF, Behar KL, De Feyter HM. In vivo 13C and 1H-[13C] MRS studies of neuroenergetics and neurotransmitter cycling, applications to neurological and psychiatric disease and brain cancer. *NMR in Biomedicine*. 2019; 32(10): e4172.

[98] Argov Z, Bank WJ. Phosphorus magnetic resonance spectroscopy (31P MRS) in neuromuscular disorders. *Annals of Neurology*. 1991; 30(1): 90-97.

[99] De Certaines JD, Larsen VA, Podo F, Carpinelli G, Briot O, Henriksen O. In vivo 31P MRS of experimental tumours. *NMR in Biomedicine*. 1993; 6(6): 345-365.

[100] Barker AR, Armstrong N. Insights into developmental muscle metabolism through the use of 31P-magnetic resonance spectroscopy: A review. *Pediatric Exercise Science*. 2010; 22(3): 350-368.

[101] Ren J, Sherry AD, Malloy CR. 31P-MRS of healthy human brain: ATP synthesis, metabolite concentrations, pH, and T1 relaxation times. *NMR in Biomedicine*. 2015; 28(11): 1455-1462.

[102] Arndt DC, Ratner AV, Faull KF, Barchas JD, Young SW. 19F magnetic resonance imaging and spectroscopy of a fluorinated neuroleptic ligand: In vivo and in vitro studies. *Psychiatry Research*. 1988; 25(1): 73-79.

[103] Ruiz-Cabello J, Barnett BP, Bottomley PA, Bulte JW. Fluorine (19F) MRS and MRI in biomedicine. *NMR in Biomedicine*. 2011; 24(2): 114-129.

[104] Colet JM, Makos JD, Malloy CR, Sherry AD. Determination of the intracellular sodium concentration in perfused mouse liver by 31P and 23Na magnetic resonance spectroscopy. *Magnetic Resonance in Medicine*. 1998; 39(1): 155-159.

[105] Radford NB, Babcock EE, Richman A, Szczepaniak L, Malloy CR, Sherry AD. 39K NMR measurement of intracellular potassium during ischemia in the perfused guinea pig heart. *Magnetic Resonance in Medicine*. 1998; 40(4): 544-550.

[106] Lin W, de Freitas DM. 35Cl NMR Study of Cl: Distribution and Transport in Human Red Blood Cell Suspensions. *Magnetic Resonance in Chemistry*. 1996; 34(10): 768-772.

[107] Harms SE, Morgan TJ, Yamanashi WS, Harle TS, Dodd GD. Principles of nuclear magnetic resonance imaging. *RadioGraphics*. 1984; 4(1): 26-43.

[108] Fourier JBJ. Théorie analytique de la chaleur. *Académie des Sciences*. 1822; 3: 1-637.

[109] Zaiss M. *Chemical Exchange Saturation Transfer in a Biophysical Context*. Ph.D. Thesis. Heidelberg University. 2013.

[110] Roberts JD. *Nuclear Magnetic Resonance: Applications to Organic Chemistry*. 1959; New York: McGraw-Hill Book Company, Inc.

[111] Hetherington HP, Newcomer BR, Pan JW. Measurements of human cerebral GABA at 4.1 T using numerically optimized editing pulses. *Magnetic Resonance in Medicine*. 1998; 39(1): 6-10.

[112] Rule GS, Hitchens TK. *Fundamentals of Protein NMR Spectroscopy*. 2006; Dordrecht, Netherlands: Springer Publishing Company.

[113] Crews P, Rodriguez J, Jaspars M. *Organic Structure Analysis*. 1998; New York: Oxford University Press.

[114] Brown JH, Gillooly JF, Allen AP, Savage VM, West GB. Toward a metabolic theory of ecology. *Ecology*. 2004; 85(7): 1771-1789.

[115] Nelson DL, Lehninger AL, Cox MM, *Lehninger Principles of Biochemistry, 5th Edition*. 2008; New York: W.H. Freeman and Company.

[116] Frayn KN. *Metabolic Regulation: A Human Perspective, 2nd Edition*. 2009; Oxford: John Wiley & Sons, Inc.

[117] Weinberg RA. *The Biology of Cancer, 2nd Edition*. 2006; New York: Garland Science.

[118] Hanahan D, Weinberg RA. Hallmarks of cancer: The next generation. *Cell*. 2011; 144(5): 646-74.

[119] Vander Heiden MG, Cantley LC, Thompson CB. Understanding the Warburg effect: The metabolic requirements of cell proliferation. *Science*. 2009; 324(5930): 1029-1033.

[120] Zheng J. Energy metabolism of cancer: Glycolysis versus oxidative phosphorylation. *Oncology Letters*. 2012; 4(6): 1151-1157.

[121] Gillies RJ, Robey I, Gatenby RA. Causes and consequences of increased glucose metabolism of cancers. *Journal of Nuclear Medicine*. 2008; 49(2): 24S-42S.

[122] Gatenby RA, Gillies RJ. Glycolysis in cancer: A potential target for therapy. *The International Journal of Biochemistry & Cell Biology*. 2007; ;39(7-8): 1358-1366.

[123] Dutta P, Martinez GV, Gillies RJ. A new horizon of DNP technology: Application to in-vivo 13 C magnetic resonance spectroscopy and imaging. *Biophysical Reviews*. 2013; 5(3): 271-281.

[124] Warburg O. On the origin of cancer cells. *Science*. 1956; 123(3191): 309-314.

[125] Schmidt CW. Metabolomics: What's happening downstream of DNA. *Environmental Health Perspectives*. 2004; 112(7): A410-A415.

[126] Birken DL, Oldendorf WH. N-acetyl-L-aspartic acid: a literature review of a compound prominent in 1H-NMR spectroscopic studies of brain. *Neuroscience & Biobehavioral Reviews*. 1989; 13(1): 23-31.

[127] Mehta V, Namboodiri MA. N-acetylaspartate as an acetyl source in the nervous system. *Molecular Brain Research*. 1995; 31(1-2): 151-157.

[128] Yoshino E, Ohmori Y, Imahori Y, Higuchi T, Furuya S, Naruse S, Mori T, Suzuki K, Yamaki T, Ueda S, Tsuzuki T. Irradiation effects on the metabolism of metastatic brain tumors: analysis by positron emission tomography and 1H-magnetic resonance spectroscopy. *Stereotactic and Functional Neurosurgery*. 1996; 66(1): 240-259.

[129] Pouwels PJ, Frahm J. Regional metabolite concentrations in human brain as determined by quantitative localized proton MRS. *Magnetic Resonance in Medicine*. 1998; 39(1): 53-60.

[130] Bruhn H, Frahm J, Gyngell ML, Merboldt KD, Hänicke W, Sauter R. Cerebral metabolism in man after acute stroke: new observations using localized proton NMR spectroscopy. *Magnetic Resonance in Medicine*. 1989; 9(1): 126-131.

[131] Arnold DL, Matthews PM, Francis G, Antel J. Proton magnetic resonance spectroscopy of human brain in vivo in the evaluation of multiple sclerosis: Assessment of the load of disease. *Magnetic Resonance in Medicine*. 1990; 14(1): 154-159.

[132] Preul MC, Caramanos Z, Collins DL, Villemure JG, Leblanc R, Olivier A, Pokrupa R, Arnold DL. Accurate, noninvasive diagnosis of human brain tumors by using proton magnetic resonance spectroscopy. *Nature Medicine*. 1996; 2(3): 323-325.

[133] Blakely RD, Coyle JT. The neurobiology of N-acetylaspartylglutamate. *International Review of Neurobiology*. 1988; 30: 39-100.

[134] Edden RA, Pomper MG, Barker PB. In vivo differentiation of N-acetyl aspartyl glutamate from N-acetyl aspartate at 3 Tesla. *Magnetic Resonance in Medicine*. 2007; 57(6): 977-982.

[135] Rerich E, Zaiss M, Korzowski A, Ladd ME, Bachert P. Relaxation-compensated CEST-MRI at 7 T for mapping of creatine content and pH–preliminary application in human muscle tissue in vivo. *NMR in Biomedicine*. 2015; 28(11): 1402-1412.

[136] Lopaschuck GD, Dhalla NS. *Cardiac Energy Metabolism in Health and Disease*. 2014; New York: Springer Publishing Company.

[137] Fogg VC, Lanning NJ, MacKeigan JP. Mitochondria in cancer: At the crossroads of life and death. *Chinese Journal of Cancer*. 2011; 30(8): 526.

[138] Saunders DE, Howe FA, Van Den Boogaart A, Griffiths JR, Brown MM. Aging of the adult human brain: In vivo quantitation of metabolite content with proton magnetic resonance spectroscopy. *Journal of Magnetic Resonance Imaging*. 1999; 9(5): 711-716.

[139] Goto N, Yoshimura R, Moriya J, Kakeda S, Hayashi K, Ueda N, Ikenouchi-Sugita A, Umene-Nakano W, Oonari N, Korogi Y, Nakamura J. Critical examination of a correlation between brain gamma-aminobutyric acid (GABA) concentrations and a personality trait of extroversion in healthy volunteers as measured by a 3 Tesla proton magnetic resonance spectroscopy study. *Psychiatry Research: Neuroimaging*. 2010; 182(1): 53-57.

[140] Miller BL. A review of chemical issues in 1H NMR spectroscopy: N-acetyl-L-aspartate, creatine and choline. *NMR in Biomedicine*. 1991; 4(2): 47-52.

[141] Zeisel SH. Dietary choline: Biochemistry, physiology, and pharmacology. *Annual Review of Nutrition*. 1981; 1(1): 95-121.

[142] Tan J, Bluml S, Hoang T, Dubowitz D, Mevenkamp G, Ross B. Lack of effect of oral choline supplement on the concentrations of choline metabolites in human brain. *Magnetic Resonance in Medicine*. 1998; 39(6): 1005-1010.

[143] Nachas N, Pinson A. Anoxic injury accelerates phosphatidylcholine degradation in cultured cardiac myocytes by phospholipase C. *FEBS Letters*. 1992; 298(2-3): 301-305.

[144] Narayana PA. Magnetic resonance spectroscopy in the monitoring of multiple sclerosis. *Journal of Neuroimaging*. 2005; 15: 46S-57S.

[145] Firbank MJ, Harrison RM, O'Brien JT. A comprehensive review of proton magnetic resonance spectroscopy studies in dementia and Parkinson's disease. *Dementia and Geriatric Cognitive Disorders*. 2002; 14(2): 64-76.

[146] Gillies RJ, Morse DL. In vivo magnetic resonance spectroscopy in cancer. *Annual Review of Biomedical Engineering*. 2005; 7: 287-326.

[147] Bruhn H, Frahm J, Gyngell ML, Merboldt KD, Hänicke W, Sauter R, Hamburger C. Noninvasive differentiation of tumors with use of localized H-1 MR spectroscopy in vivo: Initial experience in patients with cerebral tumors. *Radiology*. 1989; 172(2): 541-548.

[148] Berkelbach Van Der Sprenkel JW, Luyten PR, Van Rijen PC, Tulleken CA, Den Hollander JA. Cerebral lactate detected by regional proton magnetic resonance spectroscopy in a patient with cerebral infarction. *Stroke*. 1988; 19(12): 1556-1560.

[149] Prichard J, Rothman D, Novotny E, Petroff O, Kuwabara T, Avison M, Howseman A, Hanstock C, Shulman R. Lactate rise detected by 1H NMR in human visual cortex during physiologic stimulation. *Proceedings of the National Academy of Sciences*. 1991; 88(13): 5829-5831.

[150] Posse S, Dager SR, Richards TL, Yuan C, Ogg R, Artru AA, Müller-Gärtner HW, Hayes C. In vivo measurement of regional brain metabolic response to hyperventilation using magnetic resonance: Proton echo planar spectroscopic imaging (PEPSI). *Magnetic Resonance in Medicine*. 1997; 37(6): 858-865.

[151] Behar KL, Rothman DL, Shulman RG, Petroff OA, Prichard JW. Detection of cerebral lactate in vivo during hypoxemia by 1H NMR at relatively low field strengths (1.9 T). *Proceedings of the National Academy of Sciences*. 1984; 81(8): 2517-2519.

[152] De Graaf RA, Dijkhuizen RM, Biessels GJ, Braun KP, Nicolay K. In vivo glucose detection by homonuclear spectral editing. *Magnetic Resonance in Medicine*. 2000; 43(5): 621-626.

[153] Engskog MK, Ersson L, Haglöf J, Arvidsson T, Pettersson C, Brittebo E. β-N-Methylamino-l-alanine (BMAA) perturbs alanine, aspartate and glutamate metabolism pathways in human neuroblastoma cells as determined by metabolic profiling. *Amino Acids*. 2017; 49(5): 905-919.

[154] Fahn S, Ccote LJ. Regional distribution of γ-aminobutyric acid (GABA) in brain of the rhesus monkey. *Journal of Neurochemistry*. 1968; 15(3): 209-213.

[155] Erecińska M, Silver IA. Metabolism and role of glutamate in mammalian brain. *Progress in Neurobiology*. 1990; 35(4): 245-296.

[156] McKenna MC. Glutamate pays its own way in astrocytes. *Frontiers in Endocrinology*. 2013; 4: 191.

[157] Dang CV, Hamaker M, Sun P, Le A, Gao P. Therapeutic targeting of cancer cell metabolism. *Journal of Molecular Medicine*. 2011; 89(3): 205-212.

[158] Bak LK, Schousboe A, Waagepetersen HS. The glutamate/GABA-glutamine cycle: aspects of transport, neurotransmitter homeostasis and ammonia transfer. *Journal of Neurochemistry*. 2006; 98(3): 641-653.

[159] Pan JW, Mason GF, Pohost GM, Hetherington HP. Spectroscopic imaging of human brain glutamate by water-suppressed J-refocused coherence transfer at 4.1 T. *Magnetic Resonance in Medicine*. 1996; 36(1): 7-12.

[160] Pfeuffer J, Tkáč I, Provencher SW, Gruetter R. Toward an in vivo neurochemical profile: Quantification of 18 metabolites in short-echo-time 1H NMR spectra of the rat brain. *Journal of Magnetic Resonance*. 1999; 141: 104-120.

[161] Ye ZC, Sontheimer H. Glioma cells release excitotoxic concentrations of glutamate. *Cancer Research*. 1999; 59(17): 4383-4391.

[162] De Groot J, Sontheimer H. Glutamate and the biology of gliomas. *Glia*. 2011; 59(8): 1181-1189.

[163] Souba WW. Glutamine and cancer. *Annals of Surgery*. 1993; 218(6): 715.

[164] Cluntun AA, Lukey MJ, Cerione RA, Locasale JW. Glutamine metabolism in cancer: Understanding the heterogeneity. *Trends in Cancer*. 2017; 3(3): 169-180.

[165] Gallagher FA, Kettunen MI, Day SE, Lerche M, Brindle KM. 13C MR spectroscopy measurements of glutaminase activity in human hepatocellular carcinoma cells using hyperpolarized 13C-labeled glutamine. *Magnetic Resonance in Medicine*. 2008; 60(2): 253-257.

[166] Rajagopalan KN, DeBerardinis RJ. Role of glutamine in cancer: Therapeutic and imaging implications. *Journal of Nuclear Medicine*. 2011; 52(7): 1005-1008.

[167] Long J, Zhang CJ, Zhu N, Du K, Yin YF, Tan X, Liao DF, Qin L. Lipid metabolism and carcinogenesis, cancer development. *American Journal of Cancer Research*. 2018; 8(5): 778-791.

[168] Stanley JA, Pettegrew JW, Keshavan MS. Magnetic resonance spectroscopy in schizophrenia: Methodological issues and findings - Part I. *Biological Psychiatry*. 2000; 48(5): 357-368.

[169] Fransson A, Andreo P, Pötter R. Aspects of MR image distortions in radiotherapy treatment planning. *Strahlentherapie und Onkologie*. 2001; 177(2): 59-73.

[170] Qin Q. Point spread functions of the T_2 decay in k-space trajectories with long echo train. *Magnetic Resonance Imaging*. 2012; 30(8): 1134-42.

[171] Ljunggren S. A simple graphical representation of Fourier-based imaging methods. *Journal of Magnetic Resonance*. 1983; 54: 338-343.

[172] Rasche V, Boer RW, Holz D, Proksa R. Continuous radial data acquisition for dynamic MRI. *Magnetic Resonance in Medicine*. 1995; 34(5): 754-761.

[173] Yan H, Braun M. Image reconstruction from Fourier domain data sampled along a zig-zag trajectory. *Magnetic Resonance in Medicine*. 1991; 18(2): 405-410.

[174] Caravan P. Strategies for increasing the sensitivity of gadolinium based MRI contrast agents. *Chemical Society Reviews*. 2006; 35(6): 512-523.

[175] Wendt III RE, Nitz W, Murphy PH, Bryan RN. Characterization of fluid flow using low-spatial-resolution velocity spectra from NMR images. *Magnetic Resonance in Medicine*. 1989; 10(1): 71-88.

[176] Neubauer AM, Caruthers SD, Hockett FD, Cyrus T, Robertson JD, Allen JS, Williams TD, Fuhrhop RW, Lanza GM, Wickline SA. Fluorine cardiovascular magnetic resonance angiography in vivo at 1.5 T with perfluorocarbon nanoparticle contrast agents. *Journal of Cardiovascular Magnetic Resonance*. 2007; 9(3): 565-573.

[177] Prudhomme M, Mattéi-Gazagnes M, Fabbro-Peray P, Puche P, Chabalier JP, Delacrétaz G, François-Michel LFM, Godlewski G. MRI thermodosimetry in laser-induced interstitial thermotherapy. *Lasers in Surgery and Medicine*. 2003; 32(1): 54-60.

[178] Hoult DI, Richards RE. The signal-to-noise ratio of the nuclear magnetic resonance experiment. *Journal of Magnetic Resonance*. 1976; 24(1): 71-85.

[179] Ladd ME. High-field-strength magnetic resonance: Potential and limits. *Topics in Magnetic Resonance Imaging*. 2007; 18(2): 139-152.

[180] Celik A, Lin W. Signal and noise. *Current Protocols in Magnetic Resonance Imaging*. 2001; 1: B6.1-10.

[181] Rice SO. Mathematical analysis of random noise. *Bell System Technical Journal*. 1945; 24(1): 46-156.

[182] Gudbjartsson H, Patz S. The Rician distribution of noisy MRI data. *Magnetic Resonance in Medicine*. 1995; 34(6): 910-914.

[183] Siddiqui MM. Some problems connected with Rayleigh distributions. *Journal of Research of the National Bureau of Standards D*. 1962; 66: 167-174.

[184] Goodman NR. Statistical analysis based on a certain multivariate complex Gaussian distribution (an introduction). *The Annals of Mathematical Statistics*. 1963; 34(1): 152-177.

[185] Kale SC, Chen XJ, Henkelman RM. Trading off SNR and resolution in MR images. *NMR in Biomedicine*. 2009; 22(5): 488-494.

[186] Lin SP, Brown JJ. MR contrast agents: Physical and pharmacologic basics. *Journal of Magnetic Resonance Imaging*. 2007; 25(5): 884-899.

[187] Ramalho J, Semelka RC, Ramalho M, Nunes RH, AlObaidy M, Castillo M. Gadolinium-based contrast agent accumulation and toxicity: an update. *American Journal of Neuroradiology*. 2016; 37(7): 1192-1198.

[188] Gaha M, Chazot A, Barrat JA, Roge P, Salem DB. Excessive use of gadolinium-based contrast agents: Myth or reality?. *Journal of Neuroradiology*. 2019; 46(2): 80-81.

[189] Lee MJ, Kim MJ, Yoon CS, Song SY, Park K, Kim WS. The T2-shortening effect of gadolinium and the optimal conditions for maximizing the CNR for evaluating the biliary system: a phantom study. Korean *Journal of Radiology*. 2011; 12(3): 358-364.

[190] Rutt BK, Lee DH. The impact of field strength on image quality in MRI. *Journal of Magnetic Resonance Imaging*. 1996; 6(1): 57-62.

[191] Brown TR, Kincaid BM, Ugurbil K. NMR chemical shift imaging in three dimensions. *Proceedings of the National Academy of Sciences*. 1982; 79(11): 3523-3526.

[192] Maudsley AA, Hilal SK, Perman WH, Simon HE. Spatially resolved high resolution spectroscopy by "four-dimensional" NMR. *Journal of Magnetic Resonance*. 1983; 51(1): 147-152.

[193] Haselgrove JC, Subramanian VH, Leigh JJ, Gyulai L, Chance B. In vivo one-dimensional imaging of phosphorus metabolites by phosphorus-31 nuclear magnetic resonance. *Science*. 1983; 220(4602): 1170-1173.

[194] Pykett IL, Rosen BR. Nuclear magnetic resonance: In vivo proton chemical shift imaging. Work in progress. *Radiology*. 1983; 149(1): 197-201.

[195] Otazo R, Mueller B, Ugurbil K, Wald L, Posse S. Signal-to-noise ratio and spectral linewidth improvements between 1.5 and 7 Tesla in proton echo-planar spectroscopic imaging. *Magnetic Resonance in Medicine*. 2006; 56(6): 1200-1210.

[196] Xu D, Cunningham CH, Chen AP, Li Y, Kelley DA, Mukherjee P, Pauly JM, Nelson SJ, Vigneron DB. Phased array 3D MR spectroscopic imaging of the brain at 7 T. *Magnetic Resonance Imaging*. 2008; 26(9): 1201-1206.

[197] Zhu H, Soher BJ, Ouwerkerk R, Schär M, Barker PB. Spin-echo magnetic resonance spectroscopic imaging at 7 T with frequency-modulated refocusing pulses. *Magnetic Resonance in Medicine*. 2013; 69(5): 1217-1225.

[198] Henning A. Proton and multinuclear magnetic resonance spectroscopy in the human brain at ultra-high field strength: A review. *NeuroImage*. 2018; 168: 181-198.

[199] Schenck JF. The role of magnetic susceptibility in magnetic resonance imaging: MRI magnetic compatibility of the first and second kinds. *Medical Physics*. 1996; 23(6): 815-850.

[200] Zhang Z, Yip CY, Grissom W, Noll DC, Boada FE, Stenger VA. Reduction of transmitter B1 inhomogeneity with transmit SENSE slice-select pulses. *Magnetic Resonance in Medicine*. 2007; 57(5): 842-847.

[201] Mekle R, Mlynarik V, Gambarota G, Hergt M, Krueger G, Gruetter R. MR spectroscopy of the human brain with enhanced signal intensity at ultrashort echo times on a clinical platform at 3T and 7T. *Magnetic Resonance in Medicine*. 2009; 61(6): 1279-1285.

[202] Choi H, Underwood M, Boonsirikamchai P, Matin S, Troncoso P, Ma J. Technical challenges in 3 T magnetic resonance spectroscopic imaging of the prostate: A single-institution experience. *Quantitative Imaging in Medicine and Surgery*. 2014; 4(4): 251.

[203] Golay X, Gillen J, van Zijl PC, Barker PB. Scan time reduction in proton magnetic resonance spectroscopic imaging of the human brain. *Magnetic Resonance in Medicine*. 2002; 47(2): 384-387.

[204] Majumdar A, Ward RK. *MRI Physics, Image Reconstruction, and Analysis*. 2016; Boca Raton, Florida: CRC Press.

[205] Tweig DB. Acquistion and accuracy in rapid NMR imaging methods. *Magnetic Resonance in Medicine*. 1985; 2(5): 437-452.

[206] Haase A, Frahm J, Matthaei D, Hänicke W, Merboldt KD. FLASH imaging. Rapid NMR imaging using low flip-angle pulses. *Journal of Magnetic Resonance*. 1986; 67(2): 258-266.

[207] Hennig J, Nauerth A, Friedburg H. RARE imaging: A fast imaging method for clinical MR. *Magnetic Resonance in Medicine*. 1986; 3(6): 823-833.

[208] Posse S, Dager SR, Richards TL, Yuan C, Ogg R, Artru AA, Müller-Gärtner HW, Hayes C. In vivo measurement of regional brain metabolic response to hyperventilation using magnetic resonance: Proton echo planar spectroscopic imaging (PEPSI). *Magnetic Resonance in Medicine*. 1997; 37(6): 858-865.

[209] Otazo R, Mueller B, Ugurbil K, Wald L, Posse S. Signal-to-noise ratio and spectral linewidth improvements between 1.5 and 7 Tesla in proton echo-planar spectroscopic imaging. *Magnetic Resonance in Medicine*. 2006; 56(6): 1200-1210.

[210] Donadieu M, Le Fur Y, Lecocq A, Maudsley AA, Gherib S, Soulier E, Confort-Gouny S, Pariollaud F, Ranjeva MP, Pelletier J, Guye M, Zaaraoui W, Audoin B, Ranjeva JP. Metabolic voxel-based analysis of the complete human brain using fast 3D-MRSI: Proof of concept in multiple sclerosis. *Journal of Magnetic Resonance Imaging*. 2016; 44(2): 411-419.

[211] Korzowski A, Bachert P. High-resolution 31P echo-planar spectroscopic imaging in vivo at 7T. *Magnetic Resonance in Medicine*. 2018; 79(3): 1251-1259.

[212] Larson PEZ, Bok R, Kerr AB, Lustig M, Hu S, Chen AP, Nelson SJ, Pauly JM, Kurhanewicz J, Vigneron DB. Investigation of tumor hyperpolarized [1-13C]-pyruvate dynamics using time-resolved multiband RF excitation echo-planar MRSI. *Magnetic Resonance in Medicine*. 2010; 63(3): 582-591.

[213] Reeder SB, Atalar E, Faranesh AZ, McVeigh ER. Multi-echo segmented k-space imaging: an optimized hybrid sequence for ultrafast cardiac imaging. *Magnetic Resonance in Medicine*. 1999; 41(2): 375-385.

[214] Roemer PB, Edelstein WA, Hayes CE, Souza SP, Mueller OM. The NMR phased array. *Magnetic Resonance in Medicine*. 1990; 16(2): 192-225.

[215] Ackerman JJH, Grove TH, Wong GC, Gadian DG, Radda GK. Mapping of metabolites in whole animals by 31P NMR using surface coils. *Nature*. 1980; 283(5743): 167-170.

[216] Ohlinger MA, Sodickson DK. An introduction to coil array design for parallel MRI. *NMR in Biomedicine*. 2006; 19(3): 300-315.

[217] Katscher U, Börnert P. Parallel RF transmission in MRI. *NMR in Biomedicine*. 2006; 19(3): 393-400.

[218] Stadler A, Schima W, Ssalamah AB, Kettenbach J, Eisenhuber E. Artifacts in body MR imaging: their appearance and how to eliminate them. *European Radiology*. 2007; 17(5): 1242-1255.

[219] Griswold MA, Kannengiesser S, Heidemann RM, Wang J, Jakob PM. Field-of-view limitations in parallel imaging. *Magnetic Resonance in Medicine*. 2004; 52(5): 1118-1126.

[220] Nyquist H. Certain factors affecting telegraph speed. *Transactions of the American Institute of Electrical Engineers*. 1924; 43: 412-422.

[221] Seeger M, Nickisch H, Pohmann R, Schölkopf B. Optimization of k-space trajectories for compressed sensing by Bayesian experimental design. *Magnetic Resonance in Medicine*. 2010; 63(1): 116-126.

[222] Kyriakos WE, Panych LP, Kacher DF, Westin CF, Bao SM, Mulkern RV, Jolesz FA. Sensitivity profiles from an array of coils for encoding and reconstruction in parallel (SPACE RIP). *Magnetic Resonance in Medicine*. 2000; 44(2): 301-308.

[223] Pruessmann KP, Weiger M, Scheidegger MB, Boesiger P. SENSE: Sensitivity encoding for fast MRI. *Magnetic Resonance in Medicine*. 1999; 42(5): 952-962.

[224] Pruessmann KP, Weiger M, Boesiger P. Sensitivity encoded cardiac MRI. *Journal of Cardiovascular Magnetic Resonance*. 2001; 3(1): 1-9.

[225] Van Den Brink JS, Watanabe Y, Kuhl CK, Chung T, Muthupillai R, Van Cauteren M, Yamada K, Dymarkowski S, Bogaert J, Maki JH, Matos C, Casselman JW, Hoogeveen RM. Implications of SENSE MR in routine clinical practice. *European Journal of Radiology*. 2003; 46(1): 3-27.

[226] Heo HY, Zhang Y, Lee DH, Jiang S, Zhao X, Zhou J. Accelerating chemical exchange saturation transfer (CEST) MRI by combining compressed sensing and sensitivity encoding techniques. *Magnetic Resonance in Medicine*. 2017; 77(2): 779-786.

[227] Dydak U, Weiger M, Pruessmann KP, Meier D, Boesiger P. Sensitivity-encoded spectroscopic imaging. *Magnetic Resonance in Medicine*. 2001; 46(4): 713-722.

[228] Zhao X, Prost RW, Li Z, Li SJ. Reduction of artifacts by optimization of the sensitivity map in sensitivity-encoded spectroscopic imaging. *Magnetic Resonance in Medicine*. 2005; 53(1): 30-34.

[229] Sánchez-González J, Tsao J, Dydak U, Desco M, Boesiger P, Pruessmann KP. Minimum-norm reconstruction for sensitivity-encoded magnetic resonance spectroscopic imaging. *Magnetic Resonance in Medicine*. 2006; 55(2): 287-295.

[230] Lin FH, Tsai SY, Otazo R, Caprihan A, Wald LL, Belliveau JW, Posse S. Sensitivity-encoded (SENSE) proton echo-planar spectroscopic imaging (PEPSI) in the human brain. *Magnetic Resonance in Medicine*. 2007; 57(2): 249-257.

[231] Ozturk-Isik E, Chen AP, Crane JC, Bian W, Xu D, Han ET, Chang SM, Vigneron DB, Nelson SJ. 3D sensitivity encoded ellipsoidal MR spectroscopic imaging of gliomas at 3T. *Magnetic Resonance Imaging*. 2009; 27(9): 1249-1257.

[232] Griswold MA, Jakob PM, Nittka M, Goldfarb JW, Haase A. Partially parallel imaging with localized sensitivities (PILS). *Magnetic Resonance in Medicine*. 2000; 44(4): 602-609.

[233] Griswold MA, Jakob PM, Heidemann RM, Nittka M, Jellus V, Wang J, Kiefer B, Haase A. Generalized autocalibrating partially parallel acquisitions (GRAPPA). *Magnetic Resonance in Medicine*. 2002; 47(6): 1202-1210.

[234] Huo D, Wilson DL. Robust GRAPPA reconstruction and its evaluation with the perceptual difference model. *Journal of Magnetic Resonance Imaging*. 2008; 27(6): 1412-1420.

[235] Zhao T, Hu X. Iterative GRAPPA (iGRAPPA) for improved parallel imaging reconstruction. *Magnetic Resonance in Medicine*. 2008; 59(4): 903-907.

[236] Bauer S, Markl M, Honal M, Jung BA. The effect of reconstruction and acquisition parameters for GRAPPA-based parallel imaging on the image quality. *Magnetic Resonance in Medicine*. 2011; 66(2): 402-409.

[237] Liu W, Zhao X, Ma Y, Tang X, Gao JH. DWI using navigated interleaved multishot EPI with realigned GRAPPA reconstruction. *Magnetic Resonance in Medicine*. 2016; 75(1): 280-286.

[238] Zhu X, Ebel A, Ji JX, Schuff N. Spectral phase-corrected GRAPPA reconstruction of three-dimensional echo-planar spectroscopic imaging (3D-EPSI). *Magnetic Resonance in Medicine*. 2007; 57(5): 815-820.

[239] Tsai SY, Otazo R, Posse S, Lin YR, Chung HW, Wald LL, Wiggins GC, Lin FH. Accelerated proton echo planar spectroscopic imaging (PEPSI) using GRAPPA with a 32-channel phased-array coil. *Magnetic Resonance in Medicine*. 2008; 59(5): 989-998.

[240] Banerjee S, Ozturk-Isik E, Nelson SJ, Majumdar S. Elliptical magnetic resonance spectroscopic imaging with GRAPPA for imaging brain tumors at 3 T. *Journal of Magnetic Resonance Imaging*. 2009; 27(10): 1319-1325.

[241] Hangel G, Strasser B, Povžan M, Gruber S, Chmelík M, Gajdošík M, Trattnig S, Bogner W. Lipid suppression via double inversion recovery with symmetric frequency sweep for robust 2D-GRAPPA-accelerated MRSI of the brain at 7 T. *NMR in Biomedicine*. 2015; 28(11): 1413-1425.

[242] Nassirpour S, Chang P, Henning A. MultiNet PyGRAPPA: Multiple neural networks for reconstructing variable density GRAPPA (a 1H FID MRSI study). *NeuroImage*. 2018; 183: 336-345.

[243] Moser P, Bogner W, Hingerl L, Heckova E, Hangel G, Motyka S, Trattnig S, Strasser B. Non-Cartesian GRAPPA and coil combination using interleaved calibration data - Application to concentric-ring MRSI of the human brain at 7T. *Magnetic Resonance in Medicine*. 2019; 82(5): 1587-1603.

[244] Sodickson DK, Manning WJ. Simultaneous acquisition of spatial harmonics (SMASH): Fast imaging with radiofrequency coil arrays. *Magnetic Resonance in Medicine*. 1997; 38(4): 591-603.

[245] Jakob PM, Griswold MA, Edelman RR, Sodickson DK. AUTO-SMASH: A self-calibrating technique for SMASH imaging. *Magnetic Resonance Materials in Physics, Biology, and Medicine*. 1998; 7(1): 42-54.

[246] Heidemann RM, Griswold MA, Haase A, Jakob PM. VD-AUTO-SMASH imaging. *Magnetic Resonance in Medicine*. 2001; 45(6): 1066-1074.

[247] Wang Z, Wang J, Detre JA. Improved data reconstruction method for GRAPPA. *Magnetic Resonance in Medicine*. 2005; 53(4): 981-985.

[248] Breuer FA, Kannengiesser SAR, Blaimer M, Seiberlich N, Jakob PM, Griswold MA. General formulation for quantitative G-factor calculation in GRAPPA reconstructions. *Magnetic Resonance in Medicine*. 2009; 62(3): 739-746.

[249] Penrose R. A generalized inverse for matrices. *Mathematical Proceedings of the Cambridge Philosophical Society*. 1955; 51(3): 406-413.

[250] Windschuh J. *Isolation of Unbiased Chemical Exchange Saturation Transfer Effects at 7 T and Application to Brain Tumors*. Ph.D. Thesis. Heidelberg University. 2016.

[251] Korzowski A. *Echo-planare 31P-NMR-spektroskopische Bildgebung in vivo bei 7 T*. Ph.D. Thesis. Heidelberg University. 2015.

[252] Hayes CE, Edelstein WA, Schenck JF, Mueller OM, Eash M. An efficient, highly homogeneous radiofrequency coil for whole-body NMR imaging at 1.5 T. *Journal of Magnetic Resonance*. 1985; 63(3): 622-628.

[253] Van Der Veen JW, Weinberger DR, Tedeschi G, Frank JA, Duyn JH. Proton MR spectroscopic imaging without water suppression. *Radiology*. 2000; 217(1): 296-300.

[254] Haase A, Frahm J, Hänicke W, Matthaei D. 1H NMR chemical shift selective (CHESS) imaging. *Physics in Medicine & Biology*. 1985; 30(4): 341-344.

[255] Weygand J, Fuller CD, Ibbott GS, Mohamed ASR, Ding Y, Yang J, Hwang KP, Wang J. Spatial precision in magnetic resonance imaging–guided radiation therapy: The role of geometric distortion. *International Journal of Radiation Oncology*Biology*Physics*. 2016; 95(4): 1304-1316.

[256] Mohamed ASR, Hansen C, Weygand J, Ding Y, Frank SJ, Rosenthal DI, Hwang KP, Hazle JD, Fuller CD, Wang J. Prospective analysis of in vivo landmark point-based MRI geometric distortion in head and neck cancer patients scanned in immobilized radiation treatment position: Results of a prospective quality assurance protocol. *Clinical and Translational Radiation Oncology*. 2017; 7: 13-19.

[257] Clare S, Alecci M, Jezzard P. Compensating for B1 inhomogeneity using active transmit power modulation. *Magnetic Resonance Imaging*. 2001; 19(10): 1349-1352.

[258] Ogg RJ, Kingsley PB, Taylor JS. WET, a T1- and B1-insensitive water-suppression method for in vivo localized 1H NMR spectroscopy. *Journal of Magnetic Resonance, Series B*. 1994; 104(1): 1-10;

[259] Murdoch JB, Lampman DA. Beyond WET and DRY: optimized pulses for water suppression. In: *Proceedings of the 12th Annual Meeting of the ISMRM*. 1993; New York, New York, USA: 1191.

[260] De Graaf R, Nicolay K. Adiabatic water suppression using frequency selective excitation. *Magnetic Resonance in Medicine*. 1998; 40(5): 690-696.

[261] Starcuk Jr Z, Starcuk Z, Mlynárik V, Roden M, Horký J, Moser E. Low-power water suppression by hyperbolic secant pulses with controlled offsets and delays (WASHCODE). *Journal of Magnetic Resonance*. 2001; 152(1): 168-178.

[262] Piotto M, Saudek V, Sklenář V. Gradient-tailored excitation for single-quantum NMR spectroscopy of aqueous solutions. *Journal of Biomolecular NMR*. 1992; 2(6): 661-665.

[263] Hwang TL, Shaka AJ. Water suppression that works. Excitation sculpting using arbitrary waveforms and pulsed field gradients. *Journal of Magnetic Resonance, Series A*. 1995; 112(2): 275-279;

[264] Mescher M, Tannus A, O'Neil Johnson M, Garwood M. Solvent Suppression Using Selective Echo Dephasing. *Journal of Magnetic Resonance, Series A*. 1996; 123(2): 226-229.

[265] Tkáč I, Starcuk Z, Choi IY, Gruetter R. In vivo 1H NMR spectroscopy of rat brain at 1 ms echo time. *Magnetic Resonance in Medicine*. 1999; 41(4): 649-656.

[266] Barker GJ, Mareci TH. Suppression of artifacts in multiple-echo magnetic resonance. *Journal of Magnetic Resonance*. 1989; 83(1): 11-28.

[267] Bodenhausen G, Kogler H, Ernst RR. Selection of coherence-transfer pathways in NMR pulse experiments. *Journal of Magnetic Resonance*. 1984; 58(3): 370-388.

[268] Ernst RR, Bodenhausen G, Wokaun A. *Principles of Nuclear Magnetic Resonance in One and Two Dimensions*. 1987; New York: Oxford University Press.

[269] Moonen CTW, Van Zijl PCM. Highly effective water suppression for in vivo proton NMR spectroscopy (DRYSTEAM). *Journal of Magnetic Resonance*. 1990; 88(1): 28-41.

[270] Göksu C, Scheffler K, Ehses P, Hanson LG, Thielscher A. Sensitivity analysis of magnetic field measurements for magnetic resonance electrical impedance tomography (MREIT). *Magnetic Resonance in Medicine*. 2018; 79(2): 748-760.

[271] Hargreaves B. *Bloch Equation Simulator*. Online. Available: http://mrsrl.stanford.edu/ brian/blochsim/.

[272] Henning A, Fuchs A, Murdoch JB, Boesiger P. Slice-selective FID acquisition, localized by outer volume suppression (FIDLOVS) for 1H-MRSI of the human brain at 7 T with minimal signal loss. *NMR in Biomedicine*. 2009; 22(7): 683-696.

[273] Huang F, Akao J, Vijayakumar S, Duensing GR, Limkeman M. *k-t* GRAPPA: A *k*-space implementation for dynamic MRI with high reduction factor. *Magnetic Resonance in Medicine*. 2005; 54(5): 1172-1184.

[274] Huang F, Vijayakumar S, Li Y, Hertel S, Reza S, Duensing GR. Self-calibration method for radial GRAPPA/*k-t* GRAPPA. *Magnetic Resonance in Medicine*. 2007; 57(6): 1075-1085.

[275] Lai P, Huang F, Larson AC, Li D. Fast four-dimensional coronary MR angiography with *k-t* GRAPPA. *Journal of Magnetic Resonance Imaging*. 2008; 27(3): 659-665.

[276] Jung B, Stalder AF, Bauer S, Markl M. On the undersampling strategies to accelerate time-resolved 3D imaging using *k-t*-GRAPPA. *Magnetic Resonance in Medicine*. 2011; 66(4): 966-975.

[277] Seiberlich N, Ehses P, Duerk J, Gilkeson R, Griswold M. Improved radial GRAPPA calibration for real-time free-breathing cardiac imaging. *Magnetic Resonance in Medicine*. 2011; 65(2): 492-505.

[278] Seiberlich N, Lee G, Ehses P, Gilkeson R, Griswold M. Improved temporal resolution in cardiac imaging using through-time spiral GRAPPA. *Magnetic Resonance in Medicine*. 2011; 66(6): 1682-1688.

[279] Bauer S, Markl M, Föll D, Russe M, Stankovic Z, Jung B. *k-t* GRAPPA accelerated phase contrast MRI: Improved assessment of blood flow and 3-directional myocardial motion during breath-hold. *Journal of Magnetic Resonance Imaging*. 2013; 38(5): 1054-1062.

[280] Aandal G, Nadig V, Yeh V, Rajiah P, Jenkins T, Sattar A, Griswold M, Gulani V, Gilkeson RC, Seiberlich N. Evaluation of left ventricular ejection fraction using through-time radial GRAPPA. *Journal of Cardiovascular Magnetic Resonance*. 2014; 16(1): 79.

[281] Barkauskas KJ, Rajiah P, Ashwath R, Hamilton JI, Chen Y, Ma D, Wright KL, Gulani V, Griswold MA, Seiberlich N. Quantification of left ventricular functional parameter values using 3D spiral bSSFP and through-time Non-Cartesian GRAPPA. *Journal of Cardiovascular Magnetic Resonance*. 2014; 16(1): 65.

[282] Schnell S, Markl M Entezari P, Mahadewia RJ, Semaan E, Stankovic Z, Collins J, Carr J, Jung B. *k-t* GRAPPA accelerated four-dimensional flow MRI in the aorta: Effect on scan time, image quality, and quantification of flow and wall shear stress. *Magnetic Resonance in Medicine*. 2014; 72(2): 522-533.

[283] Wright KL, Chen Y, Saybasili H, Griswold MA, Seiberlich N, Gulani V. Quantitative high resolution renal perfusion imaging using 3D through-time radial GRAPPA. *Investigative Radiology*. 2014; 49(10): 666.

[284] Wright KL, Lee GR, Ehses P, Griswold MA, Gulani V, Seiberlich N. Three-dimensional through-time radial GRAPPA for renal MR angiography. *Journal of Magnetic Resonance Imaging*. 2014; 40(4): 864-874.

[285] Chen Y, Lee GR, Wright KL, Badve C, Nakamoto D, Yu A, Schluchter MD, Griswold MA, Seiberlich N, Gulani V. Free-breathing liver perfusion imaging using 3D through-time spiral GRAPPA acceleration. *Investigative Radiology*. 2015; 50(6): 367-375.

[286] Chen Y, Lee GR, Aandal G, Badve C, Wright KL, Griswold MA, Seiberlich N, Gulani V. Rapid volumetric T1 mapping of the abdomen using three-dimensional through-time spiral GRAPPA. *Magnetic Resonance in Medicine*. 2016; 75(4): 1457-1465.

[287] Sayin O, Saybasili H, Zviman MM, Griswold M, Halperin H, Seiberlich N, Herzka DA. Real-time free-breathing cardiac imaging with self-calibrated through-time radial GRAPPA. *Magnetic Resonance in Medicine*. 2017; 77(1): 250-264.

[288] Chen Y, Lo WC, Hamilton JI, Barkauskas K, Saybasili H, Wright KL, Batesole J, Griswold MA, Gulani V, Seiberlich N. Single breath-hold 3D cardiac T1 mapping using through-time spiral GRAPPA. *NMR in Biomedicine*. 2018; 31(6): e3923.

[289] Mickevicius NJ, Paulson ES. Simultaneous orthogonal plane cine imaging with balanced steady-state free-precession contrast using *k-t* GRAPPA. *Physics in Medicine & Biology*. 2018; 63(15): 15NT02.

[290] Einstein A. Zur Elektrodynamik bewegter Körper. *Annalen der Physik*. 1905; 322(10): 891-921.

[291] Einstein A. Die Grundlage der allgemeinen Relativitätstheorie. *Annalen der Physik*. 1916; 49(4): 284-339.

[292] Lorentz HA. La théorie electromagnétique de Maxwell et son application aux corps mouvants. *Archives Néerlandaises des Sciences Exactes et Naturelles*. 1892; 25: 363-552.

[293] Poincaré H. Sur la dynamique de l'électron. *Comptes Rendus*. 1905; 140: 1504-1508.

[294] Minkowski H. Das Relativitätsprinzip. *Annalen der Physik*. 1907; 352(15): 927-938.

[295] Griswold MA, Blaimer M, Breuer F, Heidemann RM, Mueller M, Jakob PM. Parallel magnetic resonance imaging using the GRAPPA operator formalism. *Magnetic Resonance in Medicine*. 2005; 54(6): 1553-1556.

[296] Blaimer M, Breuer FA, Mueller M, Seiberlich N, Ebel D, Heidemann RM, Griswold MA, Jakob PM. 2D-GRAPPA-operator for faster 3D parallel MRI. *Magnetic Resonance in Medicine*. 2006; 56(6): 1359-1364.

[297] Breuer FA, Blaimer M, Mueller MF, Seiberlich N, Heidemann RM, Griswold MA, Jakob PM. Controlled aliasing in volumetric parallel imaging (2D CAIPIRINHA). *Magnetic Resonance in Medicine*. 2006; 55(3): 549-556.

[298] Breuer FA, Blaimer M, Heidemann RM, Mueller MF, Griswold MA, Jakob PM. Controlled aliasing in parallel imaging results in higher acceleration (CAIPIRINHA) for multi-slice imaging. *Magnetic Resonance in Medicine*. 2005; 53(3): 684-691.

[299] Stäb D, Ritter CO, Breuer FA, Weng AM, Hahn D, Köstler H. CAIPIRINHA accelerated SSFP imaging. *Magnetic Resonance in Medicine*. 2011; 65(1): 157-164.

[300] Kim B, Lee CK, Seo N, Lee SS, Kim JK, Choi Y, Woo DC, Kim IS, Nickel D, Kim KW. Comparison of CAIPIRINHA-VIBE, Radial-VIBE, and conventional VIBE sequences for dynamic contrast-enhanced (DCE) MRI: A validation study using a DCE-MRI phantom. *Magnetic Resonance Imaging*. 2016; 34(5): 638-644.

[301] Van Der Zwaag W, Reynaud O, Narsude M, Gallichan D, Marques JP. High spatio-temporal resolution in functional MRI with 3D echo planar imaging using cylindrical excitation and a CAIPIRINHA undersampling pattern. *Magnetic Resonance in Medicine*. 2018; 79(5): 2589-2596.

[302] McKenzie CA, Ohliger MA, Yeh EN, Price MD, Sodickson DK. Coil-by-coil image reconstruction with SMASH. *Magnetic Resonance in Medicine*. 2001; 46(3): 619-623.

[303] Barkhuijsen H, De Beer R, Bovee WMMJ, Creyghton JHN, Van Ormondt D. Application of linear prediction and singular value decomposition (LPSVD) to determine NMR frequencies and intensities from the FID. *Magnetic Resonance in Medicine*. 1985; 2: 86-89.

[304] Sandgren N, Stoica P, Frigo FJ, Selén Y. Spectral analysis of multichannel MRS data. *Journal of Magnetic Resonance*. 2005; 175(1): 79-91.

[305] Pijnappel WWF, Van Den Boogaart A, De Beer R, Van Ormondt D. SVD-based quantification of magnetic resonance signals. *Journal of Magnetic Resonance*. 1992; 97(1): 122-134.

[306] Vermathen P, Kreis R, Boesch C. Distribution of intramyocellular lipids in human calf muscles as determined by MR spectroscopic imaging. *Magnetic Resonance in Medicine*. 2004; 51(2): 253-262.

[307] Hetherington HP, Pan JW, Mason GF, Ponder SL, Twieg DB, Deutsch G, Mountz J, Pohost GM. 2D 1H spectroscopic imaging of the human brain at 4.1 T. *Magnetic Resonance in Medicine*. 1994; 32(4): 530-534.

[308] Singh S, Rutt BK, Henkelman RM. Projection presaturation: a fast and accurate technique for multidimensional spatial localization. *Journal of Magnetic Resonance*. 1990; 87(3): 567-583.

[309] Bilgic B, Chatnuntawech I, Fan AP, Setsompop K, Cauley SF, Wald LL, Adalsteinsson E. Fast image reconstruction with L2-regularization. *Journal of Magnetic Resonance Imaging*. 2014; 40(1): 181-191.

[310] Fan RE, Chang KW, Hsieh CJ, Wang XR, Lin CJ. LIBLINEAR: A library for large linear classification. *Journal of Machine Learning Research*. 2008; 9: 1871-4.

[311] Bishop CM. Training with noise is equivalent to Tikhonov regularization. *Neural Computation*. 1995; 7(1): 108-116.

[312] Hoerl AE, Kennard RW. Ridge regression: Biased estimation for nonorthogonal problems. *Technometrics*. 1970; 12(1): 55-67.

[313] Metzger G, Sarkar S, Zhang X, Patel KH, Hu X. A hybrid technique for spectroscopic imaging with reduced truncation artifact. *Magnetic Resonance Imaging*. 1999; 17(3): 435-443.

[314] Bilgic B, Gagoski B, Kok T, Adalsteinsson E. Lipid suppression in CSI with spatial priors and highly undersampled peripheral k-space. *Magnetic Resonance in Medicine*. 2013; 69(6): 1501-1511.

[315] Provencher SW. Estimation of metabolite concentrations from localized in vivo proton NMR spectra. *Magnetic Resonance in Medicine*. 1993; 30(6): 672-679.

[316] Wilson M, Davies NP, Sun Y, Natarajan K, Arvanitis TN, Kauppinen RA, Peet AC. A comparison between simulated and experimental basis sets for assessing short-TE in vivo 1H MRS data at 1.5 T. *NMR in Biomedicine*. 2010; 23(10): 1117-1126.

[317] Provencher SW. Automatic quantitation of localized in vivo 1H spectra with LCModel. *NMR in Biomedicine*. 2001; 14(4): 260-264.

[318] Kroeker RM, Mcveigh ER, Hardy P, Bronskill MJ, Mark Henkelman R. In vivo measurements of NMR relaxation times. *Magnetic Resonance in Medicine*. 1985; 2(1): 1-3.

[319] Marquardt DW. An algorithm for least-squares estimation of nonlinear parameters. *Journal of the Society for Industrial and Applied Mathematics*. 1963; 11(2): 431-441.

[320] Cramér H. *Mathematical Methods of Statistics*. 1946; Princeton, New Jerson: Princeton University Press.

[321] Rao CR. Information and the accuracy attainable in the estimation of statistical parameters. *Bulletin of the Calcutta Mathematical Society*. 1945; 37: 81-89.

[322] Blinchikoff HJ, Zverev AI. *Filtering in the Time and Frequency Domains*. 1976; Rayleigh, NC: SciTech Publishing.

[323] Bernstein MA, Fain SB, Riederer SJ. Effect of windowing and zero-filled reconstruction of MRI data on spatial resolution and acquisition strategy. *Journal of Magnetic Resonance Imaging*. 2001; 14(3): 270-280.

[324] Hamming RW. *Digital Filters*. 1989; Minneola, NY: Dover Publications Inc.

[325] Gruetter R, Boesch C. Fast, noniterative shimming of spatially localized signals. In vivo analysis of the magnetic field along axes. *Journal of Magnetic Resonance*. 1992; 96: 323-334.

[326] Shen J, Rycyna RE, Rothman DL. Improvements on an in vivo automatic shimming method (FASTERMAP). *Magnetic Resonance in Medicine*. 1997; 38(5): 834-839.

[327] Gruetter R, Tkáč I. Field mapping without reference scan using asymmetric echo-planar techniques. *Magnetic Resonance in Medicine*. 2000; 43(2): 319-323.

[328] Bottomley PA. Spatial localization in NMR spectroscopy in vivo. *Annals of the New York Academy of Sciences*. 1987; 508(1): 333-348.

[329] Jung WI. Localized double spin echo proton spectroscopy part I: Basic concepts. *Concepts in Magnetic Resonance*. 1996; 8(1): 1-5.

[330] Henning A, Schär M, Schulte RF, Wilm B, Pruessmann KP, Boesiger P. SELOVS: brain MRSI localization based on highly selective T1-and B1-insensitive outer-volume suppression at 3T. *Magnetic Resonance in Medicine*. 2008; 59(1): 40-51.

[331] Garwood M, DelaBarre L. The return of the frequency sweep: Designing adiabatic pulses for contemporary NMR. *Journal of Magnetic Resonance*. 2001; 153(2): 155-177.

[332] Frahm JA, Bruhn H, Gyngell ML, Merboldt KD, Hänicke W, Sauter R. Localized high-resolution proton NMR spectroscopy using stimulated echoes: Initial applications to human brain in vivo. *Magnetic Resonance in Medicine*. 1989; 9(1): 79-93.

[333] Mlynárik V, Gambarota G, Frenkel H, Gruetter R. Localized short-echo-time proton MR spectroscopy with full signal-intensity acquisition. *Magnetic Resonance in Medicine*. 2006; 56(5): 965-970.

[334] Scheenen TW, Heerschap A, Klomp DW. Towards 1 H-MRSI of the human brain at 7T with slice-selective adiabatic refocusing pulses. *Magnetic Resonance Materials in Physics, Biology and Medicine*. 2008; 21(1-2): 95.

[335] Scheenen TW, Klomp DW, Wijnen JP, Heerschap A. Short echo time 1H-MRSI of the human brain at 3T with minimal chemical shift displacement errors using adiabatic refocusing pulses. *Magnetic Resonance in Medicine*. 2008; 59(1): 1-6.

[336] Boer VO, Siero JC, Hoogduin H, van Gorp JS, Luijten PR, Klomp DW. High-field MRS of the human brain at short TE and TR. *NMR in Biomedicine*. 2011; 24(9): 1081-1088.

[337] Donadieu M, Le Fur Y, Confort-Gouny S, Le Troter A, Guye M, Ranjeva JP. Evidencing different neurochemical profiles between thalamic nuclei using high resolution 2D-PRESS semi-LASER 1 H-MRSI at 7 T. *Magnetic Resonance Materials in Physics, Biology and Medicine*. 2016; 29(3): 491-501.

[338] Patt SL, Sykes BD. Water eliminated Fourier transform NMR spectroscopy. *The Journal of Chemical Physics*. 1972; 56(6): 3182-3184.

[339] Becker ED, Ferretti JA, Farrar TC. Driven equilibrium Fourier transform spectroscopy. A new method for nuclear magnetic resonance signal enhancement. *Journal of the American Chemical Society*. 1969; 91(27): 7784-7785.

[340] Vanhamme L, Fierro RD, Van Huffel S, De Beer R. Fast removal of residual water in proton spectra. *Journal of Magnetic Resonance*. 1998; 132(2): 197-203.

[341] Bydder GM, Young IR. MR imaging: Clinical use of the inversion recovery sequence. *Journal of Computer Assisted Tomography*. 1985; 9: 659-675.

[342] Connelly A, Counsell C, Lohman JA, Ordidge RJ. Outer volume suppressed image related in vivo spectroscopy (OSIRIS), a high-sensitivity localization technique. *Journal of Magnetic Resonance*. 1988; 78(3): 519-525.

[343] Schmale I, Gleich B, Rahmer J, Bontus C, Schmidt J, Borgert J. MPI safety in the view of MRI safety standards. *IEEE Transactions on Magnetics*. 2015; 51(2): 1-4.

[344] Kauczor HU, Ebert M, Kreitner KF, Nilgens H, Surkau R, Heil W, Hofmann D, Otten EW, Thelen M. Imaging of the lungs using 3he MRI: Preliminary clinical experience in 18 patients with and without lung disease. *Journal of Magnetic Resonance Imaging*. 1997; 7(3): 538-543.

[345] Truong TK, Clymer BD, Chakeres DW, Schmalbrock P. Three-dimensional numerical simulations of susceptibility-induced magnetic field inhomogeneities in the human head. *Magnetic Resonance Imaging*. 2002; 20(10): 759-770.

[346] Blaimer M, Breuer F, Mueller M, Heidemann RM, Griswold MA, Jakob PM. SMASH, SENSE, PILS, GRAPPA: How to choose the optimal method. *Topics in Magnetic Resonance Imaging*. 2004; 15(4): 223-236.

[347] McGibney G, Smith MR, Nichols ST, Crawley A. Quantitative evaluation of several partial Fourier reconstruction algorithms used in MRI. *Magnetic Resonance in Medicine*. 1993; 30(1): 51-59.

[348] Hu X, Parrish T. Reduction of field of view for dynamic imaging. *Magnetic Resonance in Medicine*. 1994; 31(6): 691-694.

[349] Van Vaals JJ, Brummer ME, Thomas Dixon W, Tuithof HH, Engels H, Nelson RC, Gerety BM, Chezmar JL, Den Boer JA. "Keyhole" method for accelerating imaging of contrast agent uptake. *Journal of Magnetic Resonance Imaging*. 1993; 3(4): 671-675.

[350] Madore B, Glover GH, Pelc NJ. Unaliasing by Fourier-encoding the overlaps using the temporal dimension (UNFOLD), applied to cardiac imaging and fMRI. *Magnetic Resonance in Medicine*. 1999; 42(5): 813-828.

[351] Riederer SJ, Tasciyan T, Farzaneh F, Lee JN, Wright RC, Herfkens RJ. MR fluoroscopy: Technical feasibility. *Magnetic Resonance in Medicine*. 1988; 8(1): 1-5.

[352] Brummer ME, Moratal-Pérez D, Hong CY, Pettigrew RI, Millet-Roig J, Dixon WT. Noquist: Reduced field-of-view imaging by direct Fourier inversion. *Magnetic Resonance in Medicine*. 2004; 51(2): 331-342.

[353] Madore B. UNFOLD-SENSE: A parallel MRI method with self-calibration and artifact suppression. *Magnetic Resonance in Medicine*. 2004; 52(2):

[354] Tsao J, Boesiger P, Pruessmann KP. *k-t* BLAST and *k-t* SENSE: Dynamic MRI with high frame rate exploiting spatiotemporal correlations. *Magnetic Resonance in Medicine*. 2003; 50(5): 1031-1042.

[355] Nguyen HM, Peng X, Do MN, Liang ZP. Denoising MR spectroscopic imaging data with low-rank approximations. *IEEE Transactions on Biomedical Engineering*. 2012; 60(1): 78-89.

[356] Lam F, Liang ZP. A subspace approach to high-resolution spectroscopic imaging. *Magnetic Resonance in Medicine*. 2014; 71(4): 1349-1357.

[357] Meißner JE, Korzowski A, Regnery S, Goerke S, Breitling J, Floca RO, Debus J, Schlemmer HP, Ladd ME, Bachert P, Adeberg S. Early response assessment of glioma patients to definitive chemoradiotherapy using chemical exchange saturation transfer imaging at 7 T. *Journal of Magnetic Resonance Imaging*. 2019; 50(4): 1268-1277.

[358] Korzowski A, Weinfurtner N, Mueller S, Breitling J, Goerke S, Schlemmer HP, Ladd ME, Paech D, Bachert P. Volumetric mapping of intra- and extracellular pH in the human brain using 31P MRSI at 7T. *Magnetic Resonance in Medicine*. 2020; 84: 1707-1723.

[359] Maly T, Debelouchina GT, Bajaj VS, Hu KN, Joo CG, Mak–Jurkauskas ML, Sirigiri JR, Van Der Wel PC, Herzfeld J, Temkin RJ, Griffin RG. Dynamic nuclear polarization at high magnetic fields. *The Journal of Chemical Physics*. 2008; 128(5): 02B611.

List of Figures

List of Tables

List of Scientific Contributions

Journal Contributions

1. **Weygand J**, Fuller CD, Ibbott GS, Mohamed ASR, Ding Y, Yang J, Hwang KP, Wang J. Spatial precision in magnetic resonance imaging-guided radiotherapy: The role of geometric distortion. *International Journal of Radiation Oncology* Biology* Physics.* 2016; 95: 1304-16.

2. Wang J, **Weygand J**, Hwang KP, Mohamed ASR, Ding Y, Fuller CD, Lai SY, Frank SJ, Zhou J. Magnetic resonance imaging of glucose uptake and metabolism in patients with head and neck cancer. *Scientific Reports.* 2016; 6: 1-7.

3. Salzillo TC, Hu J, Nguyen L, Whiting N, Lee J, **Weygand J**, Dutta P, Pudakalakatti S, Zacharias Millward N, Gammon ST, Lang FF, Heimberger AB, Bhattacharya PK. Interrogating metabolism in brain cancer. *Magnetic Resonance Imaging Clinics of North America.* 2016; 24: 687-703.

4. Mohamed ASR, Hansen C, **Weygand J**, Ding Y, Frank SJ, Rosenthal DI, Hwang KP, Hazle JD, Fuller CD, Wang J. Prospective analysis of in vivo landmark point-based MRI geometric distortion in head and neck cancer patients scanned in immobilized radiation treatment position: Results of a prospective quality assurance protocol. *Translational Radiation Oncology.* 2017; 7: 13-19.

5. **Weygand J**, Carter SE, Salzillo TC, Moussalli M, Dai B, Dutta P, Zuo X, Fleming JB, Shureiqi I, Bhattacharya PK. Can an organoid recapitulate the metabolome of its parent tissue? A pilot NMR spectroscopy study. *Journal of Cancer Prevention & Current Research.* 2017; 8: 00307.

6. Dutta P, Perez MR, Lee J, Kang Y, Pratt M, Salzillo TC, **Weygand J**, Zacharias NM, Gammon ST, Koay EJ, Kim M, McAllister F, Sen S, Maitra A, Piwnica-Worms D, Flemming JB, Bhattacharya PK. Combining hyperpolarized real-time metabolic imaging and NMR spectroscopy to identify metabolic biomarkers in pancreatic cancer. *Journal of Proteome Research.* 2019; 18, 2826-2834.

Scientific Conference Contributions

1. **Weygand J**, Fuller CD, Mohamed ASR, Ding Y, Wang J. *Characterizing the influence of geometric distortion in MRI-guided radiotherapy.* At: American Association of Physicists in Medicine - Southwest Regional Chapter. 2015; Galveston, TX, USA.

2. **Weygand J**, Wang J. *CEST imaging in head and neck cancer patients: Preliminary experiences.* At: 5th International Workshop on Chemical Exchange Saturation Transfer Imaging. 2015; Philadelphia, PA, USA.

3. **Weygand J**, Salzillo TC, Lee J, Zacharias NM, Dutta P, Bhattacharya PK. *Identifying immune-related metabolic signatures of pancreatic cancer.* At: World Molecular Imaging Congress. 2016; New York, NY, USA.

4. **Weygand J**, Dutta P, Molkentine J, Lee Y, Salzillo TC, Yu M, Lee J, Koay EJ, Taniguchi C, Bhattacharya PK. *Identifying Immune-Related Metabolic Properties of Pancreatic Cancer via Hyperpolarized Pyruvate Spectroscopic Imaging and NMR Metabolomics.* At: Annual Meeting of the International Society for Magnetic Resonance in Medicine. 2017; Honolulu, HI, USA.

5. **Weygand J**, Ladd ME, Bachert P, Korzowski A. *Identifying Immune-Related Metabolic Properties of Pancreatic Cancer via Hyperpolarized Pyruvate Spectroscopic Imaging and NMR Metabolomics.* At: American Association of Physicists in Medicine. 2019; San Antonio, TX, USA.

Acknowledgements

I want to take a brief moment to thank everyone who has helped me reach this point. I extend my apologies in advance to all those that I have failed to mention.

I would like to thank Professor Dr. Peter Bachert for allowing me to complete my doctoral work in his laboratory. I appreciate the freedom that he give his students in developing their scientific ideas and all the support over the past three years.

I would like to thank the members of my thesis advisory committee, Professor Dr. Joao Seco and Professor Dr. Lothar Schad, for their insightful comments at my committee meetings.

I would like to thank the Helmholtz International Graduate School at the German Cancer Research Center for their generous financial support over the past three years.

I would like to thank each and every member of Professor Bachert's laboratory throughout the past three years: Dr. Steffen Görke, Dr. Andreas Korzowski, Dr. Johannes Breitling, Vanessa Franke, Philip Boyd, Cornelius Bauer, Sarah Neumann, Florian Kroh, Nam Dang, Marcel Awenius, Dr. Ferdinand Zimmerman, Dr. Jan Meißner, Dr. Patrick Schünke, Neele Kempe, Justyna Platek, Leoni Rath, Yannick Söhngen, Sebastian Müller, and Johannes Fürle. I have had some ridiculous questions in the last few years while adjusting to life in a foreign country, such as how to properly shop in a German supermarket or how to adjust my German social security insurance number. I thank them for their ceaseless patience in helping me out in these areas and making the past few years very enjoyable.

Thank you to everyone who volunteered to be a subject of my *in vivo* experiments, specifically Dr. Andreas Korzowski, Marcel Awenius, Florian Kroh, Sebastian Müller, Cornelius Bauer, and Vanessa Franke.

A most special thanks goes to Dr. Andreas Korzowski. His supervision throughout my doctoral work has been priceless. I truly appreciate all the time that he dedicated to my project and the perspicacious insight he possesses on all aspects related to magnetic resonance spectroscopy. The last three years would have been markedly more difficult without his thoughtful guidance. Thank you, most sincerely.

Lastly, I would like to thank my parents, Donna M. Weygand and Joseph L. Weygand, for all their support over the years. It is truly appreciated.

Declaration

I, hereby, declare that this work was composed solely by the author, and all works used are listed in the bibliography.

Heidelberg, August 3rd, 2020 .....